UNIVERSITA' DEGLI STUDI DI MESSINA

DIPARTIMENTO DI SCIENZE CHIMICHE, BIOLOGICHE, FARMACEUTICHE ED AMBIENTALI

Corso di Dottorato in Scienze Chimiche – XXXIII Ciclo
Curriculum Progettazione, Sintesi, Analisi e Proprietà di Sistemi Molecolari Funzionali

Photocatalytic CO_2 Reduction by Multinuclear Metal Complexes - A Journey Towards High-Nuclearity Supramolecular Photocatalysts

Ambra Maria Cancelliere

Coordinator

Prof.ssa Paola Dugo

Supervisor

Prof. Sebastiano Campagna

2017 - 2020

Index

Introduction 1

Outline of the thesis 2

References 4

Chapter 1

Artificial Photosynthesis 5

References 8

Chapter 2

Photoinduced Electron Transfer 9

2.1 The Marcus Theory 9

2.2 Electron Transfer via Hopping or Tunnelling (or Superexchange) Mechanism 13

References 21

Chapter 3

Properties of Ruthenium Polypyridine Complexes 23

References 28

Chapter 4

Basic Concepts about CO_2 Reduction 31

4.1. Introduction 31

4.2. Redox photosensitizer 35

4.3 Catalysts 37

4.4 Electron Donors 38

4.4.1 NAD(P)H Model Compound 39

4.4.2 Dihydrobenzoimidazole Derivatives 40

References 41

Chapter 5

Photocatalytic CO_2 Reduction by Multinuclear Metal Complexes 45

5.1 Ligand bpy_2Ph and its metal complexes 46

5.1.1 Synthesis of ligand bpy_2Ph 46

5*.1.2 Synthesis of RuRe complex* 47

5.1.2.1 Absorption Spectra and Photophysical Properties 49

5.1.2.2 Redox Properties 52

5.1.2.3 Photocatalytic Analysis 55

5.2 Ligand bpy_3Ph and its metal complexes 58

5.2.1 Synthesis of ligand bpy_3Ph 58

5.2.2 Synthesis of RuRe2 and Ru2Re Supramolecular Complexes 59

5.2.2.1 Absorption Spectra and Photophysical Properties 61

5.2.2.2 Redox Properties 65

5.2.2.3 Photocatalysis Studies 69

5.2.3 Synthesis of Ru2Ru Supramolecular Complex 75

5.2.3.1 Absorption Spectra and Photophysical Properties 76

5.2.3.2 Redox Properties 78

5.2.3.3 Photocatalytic Analysis 79

5.3 Ligand bpy_4Ph and its metal complexes 80

5.3.1 Synthesis of ligand bpy_3Ph 80

5.3.2 Synthesis of Ru3Re Supramolecular Complex 81

5.3.2.1 Absorption Spectra and Photophysical Properties 83

5.3.2.2 Redox Properties 86

5.3.2.3 Photocatalysis Analysis 87

5.3.3 Synthesis of Ru3Ru Supramolecular Complex 88

5.3.3.1 Absorption Spectra and Photophysical properties 89

5.3.3.2 Redox Properties 91
5.3.3.3 Photocatalytic Analysis 92
5.4 Second generation: dendritic mixed metal photocatalysts 93
5.4.1 Synthesis of RuRe3 and RuRe6 Supramolecular Complexes 93
5.4.1.1 Absorption Spectra and Photophysical Properties 102
5.4.1.2 Redox Properties 106
References 112

Chapter 6
Conclusions 115

Chapter 7
PhotoElectrocatalysis for CO_2 Reduction – An Appendix 117
6.1 Preparation of modified photoelectrodes FTO/NiO-Dye/Catalyst 120
6.2 Spectroscopic characterization of molecular components and of the FTO/NiO-P1/Re electrode 121
6.3 Electrochemical characterization of FTO/NiO/Re and FTO/NiO-P1/Re electrodes 124
6.4. Conclusions and Perspectives 131
References 133

Chapter 8
Experimental Section 135
8.1 Materials and Methods 135
8.2 CO_2 Photoreduction 136
8.3 CO_2 PhotoElectroreduction 137
8.3.1 Modified (photo)electrode fabrication 137
8.4. Syntheses 139
8.4.1 Syntheses of the Bridging Ligands 139

8.4.2 Syntheses of the Photosensitizer Moieties 141

8.4.3 Syntheses of the Final Integrated Photosensitizer(s)-Catalyst(s) Complexes 143

8.4.4 Syntheses of the Final Integrated dendrimer Photosensitizer(s)-Catalyst(s) Complexes 145

8.4.5 Syntheses Catalysts Complexes 147

8.4.6 Syntheses of the Sacrificial Agents 148

8.5 NMR Characterization 151

References 155

Acknowledgements 157

Introduction

We have always held to the hope, the belief, the conviction that there is a better life, a better world, beyond the horizon.

Franklin D. Roosevelt

The fossil fuels have been, until now, the most exploited energy source. The growth of world population, together with the increasing demand of energy, needs, economic and industrial developments have caused the increasing in the global energy consumption. The extensive fossil fuels consumption causes an increase in the atmospheric CO_2, that induces several problems such as the global warming and the greenhouse effect. There are *a better life* and *a better world beyond the horizon*. We can reach them having the research focused on the green and sustainable energy sources. There are various kinds of energy sources suitable to this aim, but the solar energy is the most promising. Solar light is renewable and environmentally clean, inexpensive, available everywhere and abundant.[1,2] Moreover, the use of CO_2 to obtain energy-rich compounds, like CO and HCOOH, using solar light,[3] has been scientifically demonstrated. Increasing the field of research on this alternative energy source can gives us the possibility that reaching this *horizon* could not be just *a hope*.

So, the aim of my research topic during the three-year PhD course in Chemical Science was the synthesis and study of new multinuclear metal-based supramolecular systems that can integrate all the principal components needed for the photocatalytic reduction of CO_2. Most of my research work has been performed in the Photochemistry group of the Department of Chemical, Biological, Pharmaceutical and Environmental Science of University of Messina under the supervision of Prof. Sebastiano Campagna. During this period, I have

performed the syntheses and the photophysical and redox studies of all the metal complexes (including the various building blocks) reported in this thesis. Moreover, I performed the photocatalysis experiments on these complexes in the Tokyo Institute of Technology (Japan) under the supervision of prof. Osamu Ishitani, also taking advantage of a Italy-Japan collaborative research project. To complement the work on integrated systems for CO_2 photocatalysis, an investigation on the PhotoElectroreduction of CO_2 was performed in Universitè de Paris under the supervision of Dr. Marie-Pierre Santoni, where I performed the syntheses of suitable catalysts for the CO_2 reduction, the assembly of multilayer electrodes and the electrochemical analysis on these electrodes.

Outline of the thesis

In *Chapter 1* it is exposed a brief overview on the artificial photosynthesis and the principal elements that should compose an artificial photosynthetic system.

Chapter 2 summarizes the basic information about the electron transfer process, fundamental in the CO_2 reduction process.

Chapter 3 describes the principal photochemical and photophysical properties of the ruthenium polypyridine complexes, crucial element of the supramolecular systems described in this thesis.

In *Chapter 4* the bases of the CO_2 reduction are described, together with the key elements that compose an efficient system for CO_2 reduction and their principal characteristics and properties.

Chapter 5 presents all the synthesized supramolecular complexes and their photophysical and redox properties. In this chapter also the results of the photocatalysis experiments are exposed. The complexes synthesized present three different bridging ligands, which allow the possibility to build integrate photosensitizer-catalyst (PS-CAT) systems with different ratio of Ru(II)-based PS and Ru(II)- or Re(I)-based CAT subunits. The bridging ligands used are different from those usually used in this field in literature, since they guarantee a

larger separation between the photosensitizer and catalyst metal subunits. This can also have an impact on future developments of this field.

In *Chapter 6* the principal results obtained with the supramolecular systems described in detail in Chapter 5, that is the main output of the thesis, are summarized.

Chapter 7 is a brief appendix on PhotoElectrocatalytic systems, a parallel approach we used towards the preparation of metal-based integrated systems for CO_2 photoreduction. In this chapter, the construction of NiO electrodes functionalized with suitable photosensitizers and catalysts and their principal redox characteristics are reported.

Chapter 8 is the experimental section of this thesis, where the methods and materials employed and the synthetic details and procedures are reported.

References

1. (a) N. Armaroli, V. Balzani, *Angew. Chem., Int. Ed.*, 2007, **46**, 52-66; (b) M. H. V. Huynh, T. J. Meyer, *Chem. Rev.*, 2007, **107**, 5004-5064; (c) J. P. McEvoy, G. W. Brudvig, *Chem. Rev.*, 2006, **106**, 4455-4483; (d) M. Wasielewski, *Acc. Chem. Res.*, 2009, **42**, 1910-1921; (e) D. Gust, T. A. Moore, A. L. Moore, *Acc. Chem. Res.*, 2009, **42**, 1890-1898; (f) C. Herrero, A. Quaranta, W. Leibl, A. W. Rutherford, A. Aukauloo, *Energy Environ. Sci.*, 2001, **4**, 2353-2365.
2. (a) N. Armaroli, V. Balzani, *Energy for a Sustainable World: From the Oil Age to a Sun-Powered Future*, *Wiley-VCH*, Weinheim, 2011; (b) N. Armaroli, V. Balzani, N. Serpone, *Powering Planet Earth*, *Wiley-VCH*, Weinheim, 2013.
3. Y. Tamaki, O. Ishitani, *ACS Catal.*, 2017, **7**, 3394–3409.

Chapter 1

Artificial Photosynthesis

The sun represents an inexhaustive energetic source: it sends on the Earth surface every hour more energy than that consumed all over the word in one year. Nature has taken advantage of this kind of energy in natural photosynthetic processes through the conversion of water and CO_2 in O_2 and simple sugars (as $C_6H_{12}O_6$), since ancient times.[1] In natural photosynthetic organisms, such as plants and bacteria, the light conversion in useful energy-rich chemicals occurs via a series of energy and electron transfer processes. In a photosynthetic system, photosystem I (PSI)[2] and photosystem II (PSII)[3] play the role of collecting sunlight and transferring it (in the form of electronic energy) towards the reaction center, where charge separation takes place. A manganese calcium cluster acts as catalyst for the water oxidation (see eqn. 1).[4] On the other side, the reduction of NAD^+ to NADPH (useful to produce carbohydrates in the dark cycle) occurs.

$$6\,CO_2 + 6\,H_2O \xrightarrow{h\nu} C_6H_{12}O_6 + 6\,O_2 \qquad \text{eqn. 1}$$

In the past decades, by mimicking natural systems, artificial photosynthetic systems have been investigated.[5] It should be noted that natural systems are incredibly complex and it is almost impossible to mimic exactly their components. On the other side, natural photosynthesis is rather inefficient for an industrial use, so the aim of artificial photosynthesis is to borrow mechanistic information from the natural photosynthesis and use the basic functions to design more efficient ones. In order to replicate the function of the natural photosynthetic systems, the artificial photosynthetic ones must include an antenna system, a reaction center and multielectron catalysts for the oxidation and reduction processes, as shown in **Figure 1.1**.

An efficient *antenna system* should be based on a large number of chromophores that should absorb a wide portion of the solar light and, by a series of energy transfer, funnelling the light to a specific site: the energy trap.

The *reaction center* is based on redox-active species (the energy trap and the electron acceptor and donor subunits). The goal of the reaction center is obtaining a charge-separated state via a series of electron transfer processes that allow the transformation of electronic energy in redox energy.

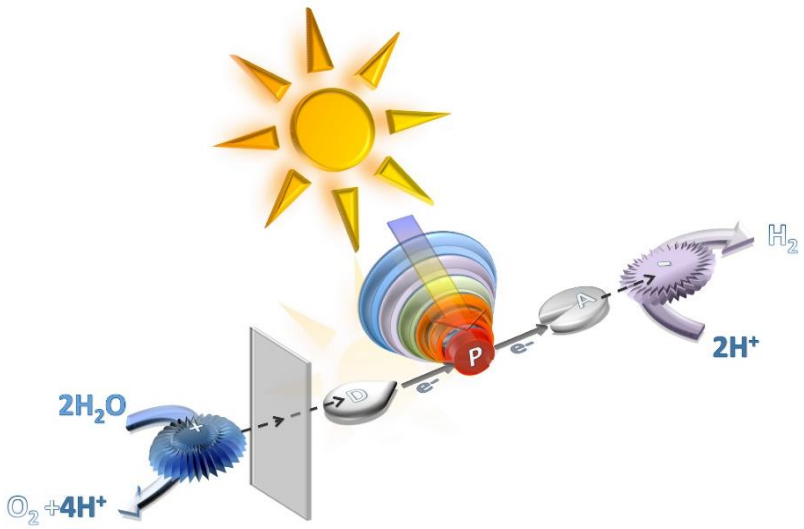

Figure 1.1. *Schematic representation of an artificial photosynthetic system.*

On the two sides of the reaction center there are two different *catalysts* able to accumulate holes and electrons needed respectively for the oxidation and the reduction processes.

In artificial photosynthesis, the mainly reactions investigated are the water splitting[6] and the CO_2 reduction,[7] but also other kinds of reactions have been studied.[8,9]

All the previously described components of the artificial photosynthetic systems are multicomponent systems themselves, so a hierarchical organization is required.[10]

The best approach to design a rational system that can act as an efficient photosynthetic system is studying all the components separately and then connect them in single supramolecular entities in a functionally-integrated manner.

References

1. V. Krewald, M. Retegan, D. A. Panzalis, *Solar Energy for Fuels*, Springer, 2015, 23-48.
2. A. Amunts, O. Drory, N. Nelson, *Nature*, 2007, **447**, 58–63.
3. Y. Umena, K. Kawakami, J. R. Shen, N. Kamiya, *Nature*, 2011, **473**, 55–60.
4. J. P. McEvoy, G. W. Brudvig, *Chem. Rev.*, 2006, **106**, 4455–4493.
5. (a) H. Dau, E. Fujita, L. Sun, *ChemSusChem*, 2017, **10**, 4228–4235; (b) B. Zhang, L. Sun, *Chem. Soc. Rev.*, 2019, **48**, 2216-2264.
6. Y. Tachibana, L. Vayssieres, J. R. Durrant, *Nature Photonics*, 2012, **6**, 511-518.
7. A. Corma, H. Garcia, *Journal of Catalysis*, 2013, **308**, 168-175.
8. K. E. Dalle, J. Warnan, J. J. Leung, B. Reuillard, I. S. Karmel, E. Reisner, *Chem. Rev.*, 2019, **119**, 2752–2875.
9. Y. Amao, *ChemCatChem*, 2011, **3**, 458 – 474.
10. S. Serroni, S. Campagna, F. Puntoriero, F. Loiseau, V. Ricevuto, R. Passalacqua, M. Galletta, *C. R. Chimie*, 2003, **6**, 883–893.

Chapter 2

Photoinduced Electron Transfer

The electron transfer process (ET) plays a key role in chemical and biological systems, such as in synthetic assemblies for solar energy conversion and information technology and in natural photosynthetic systems.[1,2,3]

In a generic electron transfer reaction, there are two species acting one as electron acceptor (A) and the other one as electron donor (D). The diffusion is the limiting factor that influences the process rate when A and D are dispersed in solution (intermolecular electron transfer). Such a process leads to the formation of A^- and D^+ ions. On the other hand, if a covalent link connects the electron donor and acceptor, the electron transfer process is no more influenced by the diffusion and can be more rapid (intramolecular electron transfer). The charge separated D^+-A^- supermolecular species is so formed.

Photoinduced Electron Transfer (PET) is a case where A or D are excited species, formed by light absorption or energy transfer. In this case, the process is easier than the process involving the species in the ground state because the excited state species are better oxidants and reductants.

2.1 The Marcus Theory

The parameters that influence the rate constant of the electron transfer are explained in the classical Marcus theory.[4] In this theory the potential energy surfaces (the Gibbs energy profiles) are represented as parabolas. In **Figure 2.1** it is shown the parabolic potential energy curves for a generic electron transfer process. In this figure, ΔG^* represents the activation energy for the electron transfer reaction; ΔG^0 is the reaction driving force (the difference in energy between the minima of the equilibrium curves); λ is the reorganization energy.

The last parameter is graphically defined in **Figure 2.1** and mathematically by the eqn. 1:

$$\lambda = \lambda_i + \lambda_o \qquad \text{eqn. 1}$$

Where λ_i deals with the bond length and the vibrational mode of the reactants and λ_o is related to the reorganization and to the parameters of the solvent and it is given by the eqn. 2:

$$\lambda_o = e^2 \left(\frac{1}{\varepsilon_{op}} - \frac{1}{\varepsilon_s}\right)\left(\frac{1}{2r_A} + \frac{1}{2r_D} - \frac{1}{r_{DA}}\right) \qquad \text{eqn. 2}$$

In this equation, reactants are approximated to be spheres in a dielectric continuum; ε_s and ε_{op} are respectively the static and optical solvent dielectrics; r_D and r_A are the donor and acceptor radii and r_{DA} represents the distance center-to-center between the reactants.

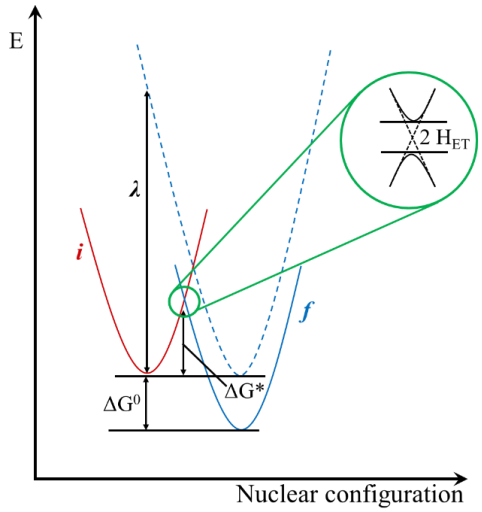

Figure 2.1. *Parabolic potential energy curves for the electron transfer:* ***i*** *represents the initial state (D-A) and* ***f*** *is the final state (D^+-A^-).*

From eqn. 1 and 2 it is possible to assume that:

1. The radii of D and A are inversely related with the reorganization energy (due to a less interaction between solvent and ions);

2. When distance between donor and acceptor decrease, the value of λ decreases too;
3. The reorganization energy value decreases when there are solvents with a high dielectric constant (ε_2).

The eqn. 3, according to the Fermi Golden Rule, represents the rate constant for the electron transfer (here a semi-quantomechanical approach, inherently non-adiabatic, is considered):[5]

$$K_{el} = \frac{4\pi}{h} |H_{ET}|^2 \, FCWD \qquad \text{eqn. 3}$$

H_{ET} is a matrix element representing the electronic coupling for the electron transfer reaction between the reactant and product states. This coupling depends on the overlapping region magnitude between acceptor and donor orbitals. A small value of H_{ET} implies that the product and reactant energy surfaces (see **Figure 2.1**) do not present strong interactions and the ET process is called non-adiabatic. On the contrary, if the H_{ET} value is quite large, the energy surfaces interact significantly and the electron transfer is named adiabatic.

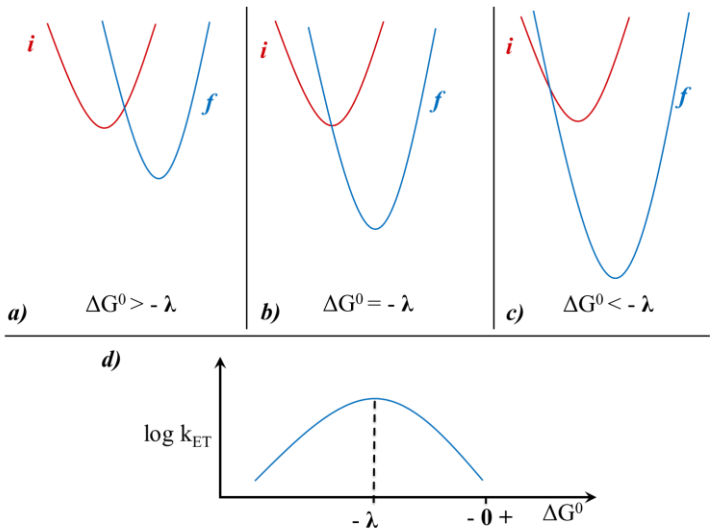

Figure 2.2. *In the panel a), b) and c) the different region in the Marcus theory are shown. Panel d) shows the dependence of the electron transfer rate on the driving force.*

The FCWD term (Franck-Condon weighted density of states) in eqn. 3 is a thermally averaged overlap which connects the initial and final vibrational wavefunctions. This term can be expressed, using a single-mode approximation with quantum mode of frequency ν_i, by the equation 4:[6,7]

$$FCWD = \left(\frac{1}{4\pi\lambda_0 K_B T}\right)^{\frac{1}{2}} \sum_m S^m \frac{e^{-S}}{m!} \exp\left[-\frac{(\Delta G^0 + \lambda_0 + m h\nu_i)^2}{4\lambda_0 K_B T}\right] \qquad \text{eqn. 4}$$

Where m is the number of vibrational states in the final state, ΔG^0 is the variation of the free energy, λ_o is related to the reorganization energy of the solvent (outer-sphere) and S (the Huang-Rhys factor) is expressed by the eqn. 5:

$$S = \frac{\lambda_i}{h\nu_i} \qquad \text{eqn. 5}$$

The S parameter is dimensionless and is proportional to the inner-sphere reorganization energy λ_i.[6,7]

The FCWD term takes note of the nuclear reorganization and the driving force effects simultaneously. This parameter can be expressed by the eqn. 6 considering the high-temperature limits, yielding to the classical expression of the Marcus theory:[7,8]

$$FCWD = \left(\frac{1}{4\pi\lambda K_B T}\right)^{\frac{1}{2}} \exp\left[-\frac{(\Delta G^0 + \lambda)^2}{4\lambda K_B T}\right] \qquad \text{eqn. 6}$$

Specifically, eqn. 6 connects $-\Delta G^0$ term with the reorganization energy λ, predicting three different kinetic regimes (as exposed in **Figure 2.2**, assuming that the final potential energy surface is only vertically shifted in respect to the initial surface):[7,8,9]

- A "normal" regime when $-\Delta G^0$ is smaller than λ (**Figure 2.2a**), the rate constant for the electron transfer increases as ΔG^* diminishes;
- An activationless regime when $-\Delta G^0$ is equal to λ, $\Delta G^* = 0$ and the rate constant for the electron transfer reaches its maximum value (**Figure**

2.2b);

- An "inverted" regime when $-\Delta G^0$ is larger than λ, the activation energy should increase again even though the driving force becomes even more negative (**Figure 2.2c**); k_{ET} decreases when the process becomes more exergonic (Marcus inverted region).[7-9]

2.2 Electron Transfer via Hopping or Tunneling (or Superexchange) Mechanism

What discussed till now refers to a generic case of electron transfer. Now it will be examined the case where one or more subunits called bridge (B) link the electron donor (D) and the electron acceptor (A). The characteristics of the bridge (i.e. its nature and molecular orbitals) strongly influence the processes of charge separation and recombination.

The electron transfer in D-B-A systems may involve two kinds of mechanisms: hopping or tunneling.[3-10]

The hopping mechanism is presumed to occur when the bridge's LUMO is energetically close to the donor's one and its state is thermodynamically accessible. In this mechanism the bridge is reduced or oxidized via a multistep charge transport in order to obtain a charge separation.

Instead, in the tunneling mechanism it must be introduced the superexchange model, in which bridge-involving states are not thermodynamically available because too high in energy with respect to the donor- and acceptor-centred states. However, despite the bridge makes the electronic coupling between the donor and acceptor possible, it is never directly oxidized or reduced (in other words, the bridge-involving states behave as *virtual states*).[11] As mentioned above, it should be expected that the electron transfer via tunneling mechanism is slower than via hopping, but in some D-B-A systems a mixture of both mechanisms can take place.

The next part of this paragraph will be focused on the tunnelling (or superexchange) mechanism. In this case the orbitals of D, B and A are involved in the formation of virtual states (for the superexchange mechanism model) via two main pathways (see **Figure 2.3**):

- The electron transfer (ET) pathway, where a virtual D^+-B^--A participates state, involves the lowest virtual molecular orbital centred on the bridge;
- The hole transfer (HT) route, where there is the participation of a D-B^+-A^- virtual state (the highest molecular orbital occupied centred on the bridging ligand).

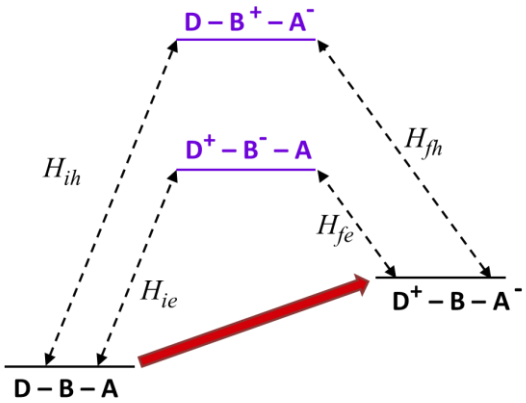

Figure 2.3. *Schematic representation of the electron transfer via superexchange model in D-B-A systems. The excited blue states are the possible virtual state involved in the electron and hole transfer.*

In the case where there is no direct coupling between donor and acceptor (or it is negligible) the superexchange coupling H_{ET} is mediated by the bridge as shown in eqn. 7:[12,13,14]

$$H_{ET} = H^e + H^h = \frac{H_{ie}H_{fe}}{\Delta E_{e(if)}} + \frac{H_{ih}H_{fh}}{\Delta E_{h(if)}} \qquad \text{eqn. 7}$$

Where H_{ie} and H_{fe} are matrix elements referring to the couplings between the initial and final states with the electron transfer virtual state D^+-B^--A, while H_{ih} and H_{fh} are the corresponding coupling with the hole transfer virtual state D-B^+-A^- and $\Delta E_{e(if)}$ and $\Delta E_{h(if)}$ represents the difference in energy between the virtual

ET and HT and the initial or final state. In the eq. 7 is clearly evidenced that both HT and ET superexchange routes could be involved in the thermal electron transfer reactions.

In general, in the photoinduced electron transfer processes the charge separated species can be obtained via a reductive or an oxidative mechanism.[3,15]

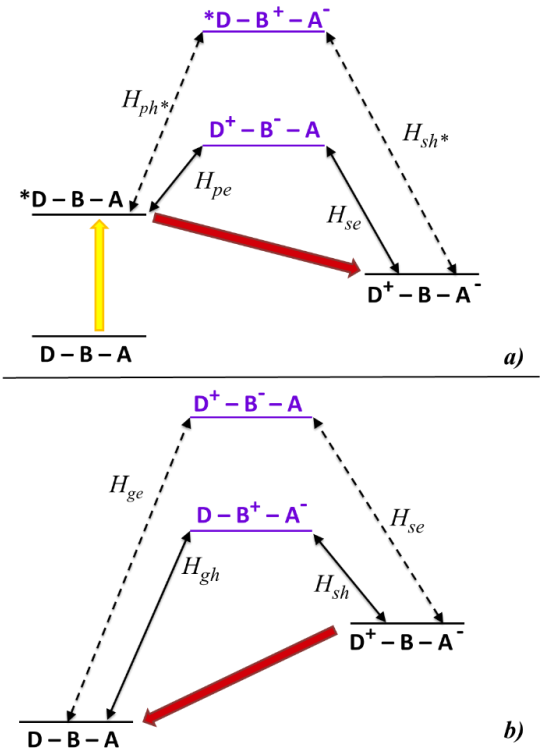

Figure 2.4. *Schematization of the states which take part in an oxidative electron transfer mechanism mediated by superexchange in a typical D-B-A molecular dyad. The double arrows represent the couplings among the states. In the panel a) shows a yellow arrow representing the light effect and it illustrates the states involved in the forward electron transfer process (the photoinduced charge separation); in the panel b) the back electron transfer process is shown (the charge recombination process). The state D-B*$^{+}$*-A*$^{-}$ *in the panel b) does not appear in the panel a) because it cannot assist the forward process.*

In the oxidative electron transfer process, it is possible considering the electron moving from the D excited state to the A ground state (as shown in **Figure 2.4a**). The only virtual states possibly involved in the charge separation are the ones that grant a connection through the bridge between the initial *D-B-A

photo-excited state with the charge separated D^+-B-A^- state, via two sequential one-electron transfer steps. The virtual state D-B^+-A^- is not a superexchange mediator because it involves a two-electrons transfer. Moreover, the *D-B^+-A^- excited hole transfer state is too high in energy, so its contribution to the charge separated state formation can be neglectable.[16] For these reasons, the virtual state D^+-B^--A is the most efficiently involved in the charge separated state formation.

Generally, the matrix element for the superexchange electronic coupling involved in an oxidative charge separation process (H^{CS}_{OPET}) can be expressed by the eqn. 8:[17]

$$H_{OPET}^{CS} = \frac{H_{pe}H_{se}}{\Delta E_{e(ps)}} + \frac{H_{ph^*}H_{sh^*}}{\Delta E_{h^*(ps)}} \qquad \text{eqn. 8}$$

Where H_{pe}, H_{se}, H_{ph^*} and H_{sh^*} are defined in **Figure 2.4a** and represent the virtual states intermediate coupling matrix elements and $\Delta E_{e(ps)}$ and $\Delta E_{h^*(ps)}$ represent the energy gap between the virtual states and the initial or final states of the process. The first term of the eqn. 8 is expected to be the dominating one and, for this reason, it is reasonably predictable that the charge separation, in photoinduced oxidative electron transfer, takes place by an electron transfer superexchange path.[3,15,17]

On the other hand, in the reductive mechanism for the photoinduced electron transfer, the excited species is the electron acceptor, which is reduced by the electron donor in the ground state. Also in this case, the only virtual states possibly involved in the charge separation are the ones that grant a connection through the bridge between the initial D-B-*A photo-excited state with the charge separated D^+-B-A^- state, via two sequential one-electron transfer steps. Among all the possible virtual state represented in **Figure 2.5a**, the D-B^+-A^- state is not a superexchange mediator because it involves a two-electrons transfer; the D^+-B^--*A excited state is too high in energy, so its contribution to the charge separated state formation can be neglectable;[3] so, the virtual state

$D\text{-}B^{+}\text{-}A^{-}$ is the most efficiently involved in the charge separated state formation. The superexchange electronic coupling matrix element for the reductive charge separation process (H^{CS}_{RPET}) can be expressed by the eqn. 9:

$$H^{CS}_{RPET} = \frac{H_{ph}H_{sh}}{\Delta E_{h(ps)}} + \frac{H_{pe^*}H_{se^*}}{\Delta E_{e^*(ps)}} \qquad \text{eqn. 9}$$

Where H_{ph}, H_{sh}, H_{pe^*} and H_{se^*} are defined in **Figure 2.5a** and represent the virtual states intermediate coupling matrix elements and $\Delta E_{h(ps)}$ and $\Delta E_{e^*(ps)}$ represent the energy gap between the virtual states and the initial or final states of the process.

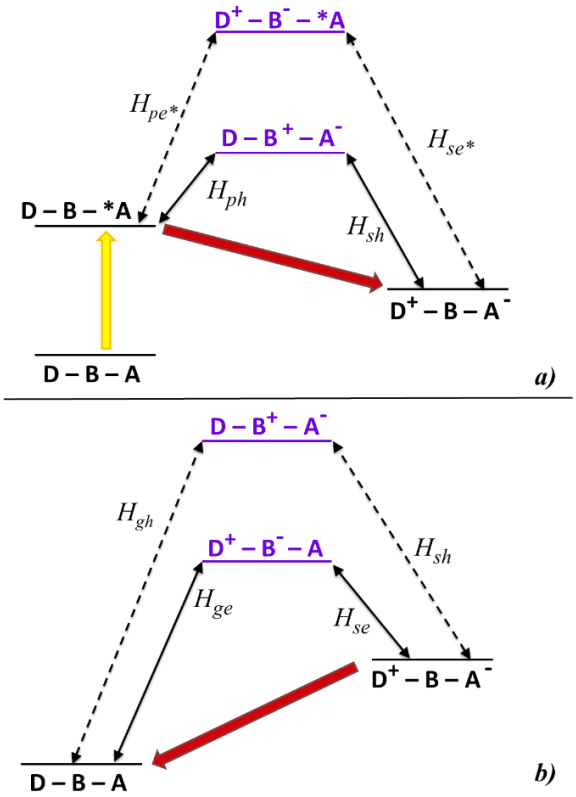

Figure 2.5. *Schematization of the states which take part in a reductive photoinduced electron transfer process mediated by superexchange in a typical D-B-A system. The double arrows represent the couplings among the states. In the panel a) shows a yellow arrow representing the light effect and it illustrates the states involved in the forward electron transfer process; in the panel b) the back electron transfer process is shown.*

The first term of the eqn. 9 is expected to be the dominating one, because of the major contribution of the D-B^+-A^- state; for this reason it is reasonably predictable that the charge separation, in photoinduced reductive electron transfer, takes place via an hole transfer superexchange path.[3,15,17]

Also in the charge recombination processes, both the hole and electron transfer pathways should be considered (see **Figure 2.4b** and **2.5b**).

The bridge is usually based on aromatic units or π-conjugated systems (e.g. double bonds). The MOs energy level and the HOMO-LUMO energy difference in the bridge should decrease by increasing the extension of the conjugated system size.[3,10] So, the model of the superexchange might be modified when the bridge is composed by several repeating units (the so called "modular" bridge).

It is now described an example of oxidative electron transfer in a dyad with a modular bridge based on three repeating units schematized in **Figure 2.6**. It can be noted that, even if the following example is referred to an oxidative mechanism, the same consideration can be done also for the reductive electron transfer or charge recombination (applying the appropriate scheme).

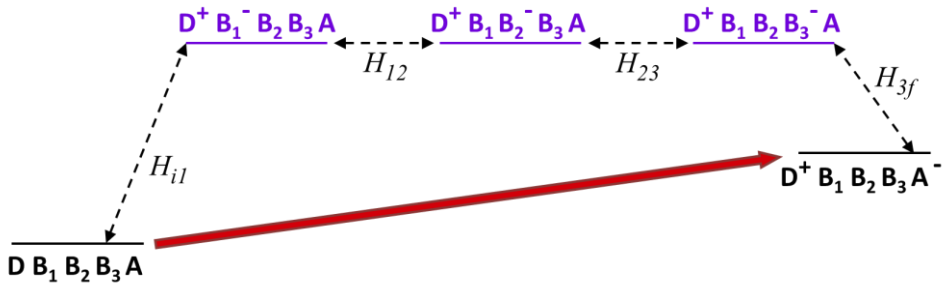

Figure 2.6. *Schematization of the superexchange interactions mediating an oxidative photoinduced electron transfer in a system with a modular bridge composed by three repetitive units. The excited blue states are the possible virtual state involved in the electron and hole transfer and the double arrows represent the couplings among the states.*

The charge separation rate matrix element is calculated by the eqn. 10:[3]

$$H^e = \frac{H_{i1}H_{12}H_{23}H_{3f}}{\Delta E^3} \qquad \text{eqn. 10}$$

Where H_{i1} and H_{3f} represent the coupling between the states localized on the bridge and, respectively, the initial and final sates, $H_{12} = H_{23}$ are the coupling between the close units of the bridge and ΔE represents the energy gap between the bridge-localized virtual states and the initial or final states of the process. For *n* repeating units the eqn.10 becomes:

$$H^e = \frac{H_{i1}H_{nf}}{\Delta E}\left(\frac{H_{mn}}{\Delta E}\right)^{n-1} \qquad \text{eqn. 11}$$

The first term of eq. 11 represents the coupling between the bridge units and the initial or final states and the second term gives the interaction propagation along the bridge (given that H12 = H23=…=Hmn). Ideally, ΔE is not dependent from the bridge length when there are weak interactions between the bridge units.[3] So, the electronic matrix element should exponentially decrease with the number of modules *n* of the bridge:

$$H^e = H^e(0)\exp\left[-\frac{\beta_n}{2}(n-1)\right] \qquad \text{eqn. 12}$$

In eqn. 12, $H^e(0)$ is the coupling term for a single-module dyad and is expressed by the eqn. 13 and β_n represents the decay coefficient (eqn. 14):

$$H^e(0) = \frac{H_{i1}H_{1f}}{\Delta E} \qquad \text{eqn. 13}$$

$$\beta_n = 2\ln\frac{\Delta E}{H_{mn}} \qquad \text{eqn. 14}$$

In the case of electron transfer in presence of modular bridges the process rate constant (K^{ET}) decreases exponentially with the distance between the donor and acceptor (*r*) as expressed by the eqn. 15:

$$K^{ET} = K_0^{ET}\exp[-\beta(r-r_0)] \qquad \text{eqn. 15}$$

$$\beta = \frac{2}{r_m}\ln\frac{\Delta E}{H_{mn}} \qquad \text{eqn. 16}$$

In eqn. 16, r_m represents the length of one bridge unit. It is evident from eq. 16 that β, in modular-bridge systems, depends on ΔE; consequently, it changes by using different donor or acceptor units and it can explain how the modular bridge mediates the donor-acceptor interaction. The equations 10 – 16 evidence also that the bridges should, preferably, have high-energy HOMOs or low-energy LUMOs, in order to obtain a long-range hole or electron transfer.[3]

References

1. (a) M. R. Wasielewski, *Chem. Rev.*, 1992, **92**, 435-461; (b) D. Gust, T. A. Moore, A. L. Moore, *Acc. Chem. Res.*, 1993, ***26***, 198-205.
2. (a) V. Balzani, *Pure Appl. Chem.*, 1990, **62**, 1099-1102; (b) T. J. Meyer, *Acc. Chem. Res.*, 1989, **22**, 163-170; (c) J. J. Onuchic, D. N. Beratan, J. R. Winkler, H. B. Gray, *Annu. Rev. Biophys. Biomol. Struct.*, 1992, **21**, 349-377; (d) B. Albinsson, J. Martersson, *J. Photochem. Photobiol. C: Photochem. Rev.*, 2008, **9**, 138-155.
3. M. Natali, S. Campagna, F. Scandola, *Chem. Soc. Rev.*, 2014, **43**, 4005-4018.
4. R. A. Marcus, N. Sutin, *Biochim. Biophys. Acta*, 1985, **811**, 265-322.
5. M. N. Paddon-Row, in: V. Balzani, *Electron Transfer in Chemistry*, Wiley-VCH, Weinheim, 2001, vol. 3, p. 179.
6. (a) T. J. Meyer, *Pure Appl. Chem.* 1986, **58**, 1193-1206; (b) P. F. Barbara, T. J. Meyer, M. A. Ratner, *J. Phys. Chem.*, 1996, **100**, 13148-13168; (c) J. R. Miller, J. V. Beitz and R. K. Huddleston, *J. Am. Chem. Soc.*, 1984, **106**, 5057-5068.
7. (a) N. Sutin, *Prog. Inorg. Chem.*, 1983, **30**, 441; (b) R. D. Cannon, *Electron Transfer Reactions*, Butterworths, London, 1980; (c) L. Eberson, *Electron Transfer Reactions in Organic Chemistry* Springer, New York, 1987.
8. (a) R. A. Marcus, *J. Chem. Phys.*, 1965, **43**, 679-701; (b) R. A. Marcus, *Disc. Faraday Soc.*, 1960, **29**, 21-31.
9. (a) J. Jortner, *J. Chem. Phys.*, 1976, **64**, 4860-4867; (b) V. Balzani, F. Scandola, *Supramolecular Photochemistry*, ed. Ellis Horwood, 1991, Ch. 5; (c) H. M. McConnell, *J. Chem Phys.*, 1961, 35, 508-515.
10. M. Gilbert, B. Albinsson, *Chem. Soc. Rev.*, 2005, **44**, 845-862.
11. V. Balzani, P. Ceroni, A. Juris, *Photochemistry and Photophysics. Concepts, Research, Perspectives*, Wiley-VCH, Weinheim, 2014.
12. (a) J. N. Onuchic, D. N. Beratan, *J. Am. Chem. Soc.*, 1987, **109**, 6771-67780; (b) K. V. Mikkelsen, M. A. Ratner, *J. Phys. Chem.*, 1989, **93**, 1759-

1770; (c) M. D. Newton, *Chem. Rev.*, 1991, **91**, 767-792; (d) K. D. Jordan, M. N. Paddon-Row, *Chem. Rev.*, 1992, **92**, 395-410; (e) P. F. Barbara, T. J. Meyer, M. A. Ratner, *J. Phys. Chem.*, 1996, **100**, 13148-13168; (f) D. Gust, T. A. Moore, A. L. Moore, *Acc. Chem. Res.*, 2001, **34**, 40-48; (g) S. Fukuzumi, *Bull. Chem. Soc. Jpn.*, 2006, **79**, 177-195; (h) S. Wenger, *Acc. Chem. Res.*, 2011, **44**, 25-35.

13. J. R. Winkler, H. B. Gray, *J. Am. Chem. Soc.*, 2014, **136**, 2930-2939.
14. (a) F. Scandola, C. Chiorboli, M. T. Indelli and M. A. Rampi, in *Electron Transfer in Chemistry*, ed. V. Balzani, Wiley-VCH, Weinheim, Germany, 2001, ch. 2.3, vol. III; (b) J. Halpern, L. E. Orgel, *Discuss. Faraday Soc.*, 1960, **29**, 32-41.
15. A. Arrigo, A. Santoro, F. Puntoriero, P. P. Lainé, S. Campagna, *Coord. Chem. Rev.*, 2015, **304-305**, 109-116
16. J. R. Miller, J. V. Beitz, R. K. Huddleston, *J. Am. Chem. Soc.*, 1984, **106**, 5057-5068.
17. A. Arrigo, A. Santoro, M. T. Indelli, M. Natali, F. Scandola, S. Campagna, *Phys. Chem.Chem. Phys.*, 2014, **16**, 818-826.

Chapter 3

Properties of Ruthenium Polypyridine Complexes

Ru(II) polypyridine complexes have been widely studied in the last decades. Ruthenium, in its 2+ oxidation state, is a d^6 system. Polypyridine are colourless molecules and strong field ligands. These ligands can act as σ-donor, using the orbital localized on the nitrogen atoms, and π-donor and π*-acceptor, using the orbital delocalized on the aromatic rings. A schematization of the molecular orbital (MO) diagram and the possible electronic transition of the $Ru(LL)_3^{2+}$ complexes (where LL indicates the bidentate polypyridine ligand) is shown in **Figure 3.1**.

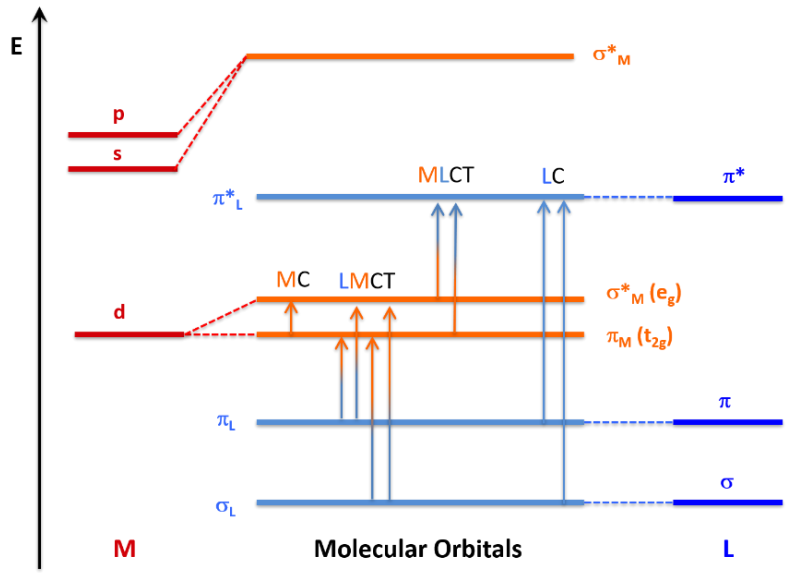

Figure 3.1. *Scheme of MO with possible electronic transition.*

In these complexes, which present octahedral symmetry, it is possible to observe several electron transitions with the formation of the following excited states:

- A Metal Centred (MC) excited state involving the promotion of an electron from the π_M to σ^*_M orbitals;
- A Metal To Ligand Charge Transfer (MLCT) excited state involving the electron promotion from a π_M metal orbital to a π_L^* ligand orbitals;
- A Ligand Centred (LC) excited state involving the electron promotion from π_L to a π_L^* orbitals.

The LMCT excited state could not be observed at low energy because in low spin octahedral complexes the $\pi_M(t_{2g})$ orbital are fulfilled.

All the excited states previously described may have singlet or triplet multiplicity, the same in the MC and MLCT excited states where a large singlet-triplet mixing occurs due to a spin-orbit coupling.[1,2,3,4]

$Ru(LL)_3^{2+}$ complexes (among which $Ru(bpy)_3^{2+}$ is the most studied and could be used as model) present a D_3 symmetry.[5] The π^* orbitals may be symmetrical or antisymmetrical referring to C_2 rotational axis retained by each Ru(LL) unit (respectively χ and φ, following the Orgel notation)[6].

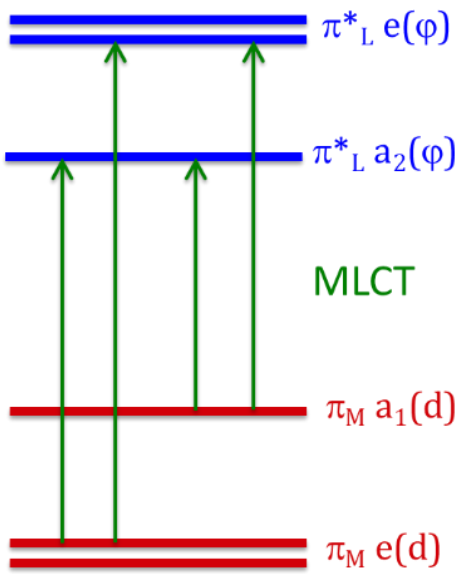

Figure 3.2. *Detailed representation of MLCT transition in metal complexes with D_3 symmetry.*

Figure 3.2 shows a more detailed representation of the HOMOs (Highest Occupied Molecular Orbitals, π_M $a_1(d)$ and π_M $e(d)$), mainly localized on the metal, and LUMOs (Lowest Unoccupied Molecular Orbitals, $\pi^*_L a_2(\varphi)$ and $\pi^*_L e(\varphi)$) mainly localized on the ligands.[7,8] In such complexes the ground state is a singlet where the electron takes up the HOMO with π_M $e(d)^4$ π_M $a_1(d)^2$ electronic configuration. The photochemical and photophysical properties are determined by the lowest excited state (following the Kasha's rule) or the upper states which can be populated (according to Boltzmann equilibrium distribution).

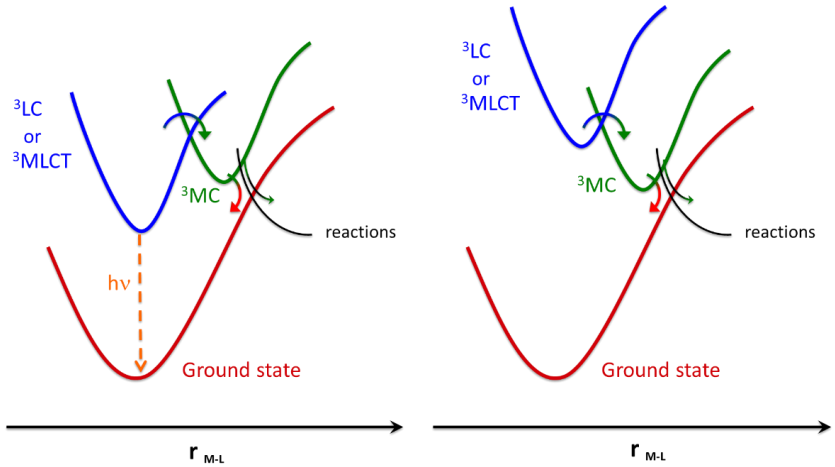

Figure 3.3. *Schematization of two limiting cases of the relative position of MC and MLCT or LC states.*

If the lowest energy exited state is MC, as a result of a very distorted geometry of the MC state compared to the ground state along the metal-ligand vibration coordination in the d^6 octahedral complexes,[9] it could lead to fast non-radiative deactivation and/or ligand dissociation reaction (see **Figure 3.3**); for this reason, at room temperature, MC excited states lifetimes are very short, it is not possible to observe luminescence phenomena[10] and bimolecular reaction does not take place.

If the lowest energy excited state does not have a high distorted geometry respect to the ground state as the MLCT and LC excited state, it could lead to a radiative decay and luminescence may also be seen (**Figure 3.3**).

The triplet MLCT excited state is more strongly influenced by the spin-orbit coupling effect than triplet LC excited state and this result in a greater radiative constant rate for the MLCT excited state. For this reason, emission from ^{3}MLCT excited state can be observed in fluid solution at room temperature and ^{3}LC emission is not observed (or less frequently observed) in such a condition. Instead, ^{3}LC excited state could lead to luminescence in a rigid matrix at low temperature.

In Ru(II) polypyridine complexes the energy position of MC, MLCT and LC may be modulated by changing the ligand,[11,12] because the energy of these states depends on the nature of the metal (i.e. redox properties) and the ligand (i.e. the ligand field strength and redox and intrinsic properties of the ligands). After a wide overview of the reduced and excited complexes with a variety of spectroscopic and electrochemical techniques,[13] the orbital involved in the ^{3}MLCT excited state is best described as localized on a single chelated unit.

It is possible to discuss the general properties of Ru(II) polypyridine complexes, using the $[Ru(bpy)_3]^{2+}$ as model.

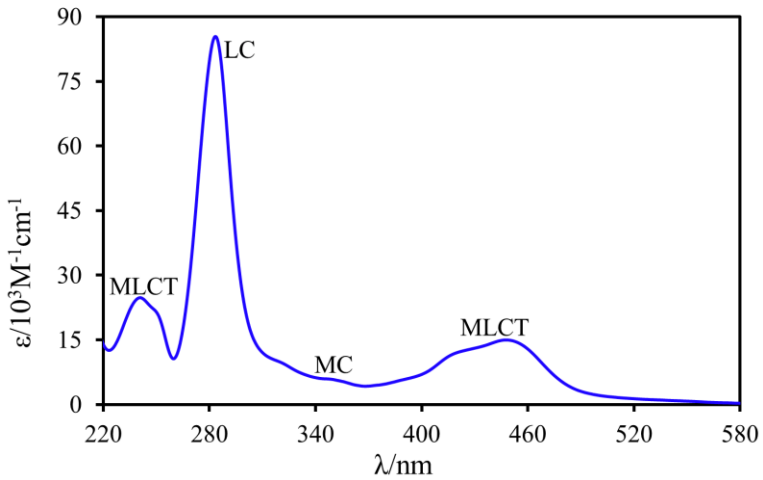

Figure 3.4. *Absorption spectrum of $[Ru(bpy)_3]^{2+}$ in acetonitrile solution at room temperature.*

As shown in **Figure 3.4**, the absorption spectrum of $[Ru(bpy)_3]^{2+}$ presents at 285 nm an intense band attributed, by comparison with the spectrum of protonated bipyridine, to the spin-allowed LC π-π* transitions.[14] It is also possible observing two intense bands due to the MLCT d-π* transition at 240 and 450 nm. The two small shoulders at 320 and 350 nm might be assigned to MC transitions.

In the same experimental conditions, the state which produces luminescence is a ^{3}MLCT spin-forbidden excited state.[15]

References

1. G. A. Crosby, *Acc. Chem. Res.*, 1975, **8**, 231-238.
2. G. A. Crosby, *Adv. Chem. Ser.*, 1976, **150**, 149-159.
3. E. M. Kober, T. J. Meyer, *Inorg. Chem.*, 1982, **21**, 3967-3977.
4. K. Mandal, T. L. D. Pearson, W. P. Krug, J. N. Demas, *J. Am. Chem. Soc.*, 1983, **105**, 701–707.
5. D. P. Rillema, D. S. Jones, H. A. Levy, *J. Chem. Soc. Chem. Commun.*, 1979, 849
6. L. E. Orgel, *J. Chem. Soc.*, 1961, 3683-3686.
7. K. Kalyanasundaram, *Coord. Chem. Rev.*, 1982, **46**, 159-244.
8. R. J. Watts, *J. Chem. Educ.*, 1983, **60**, 834-842.
9. A. W. Adamson, *J. Chem. Educ.*, 1983, **60**, 797-802.
10. P. D. Fleischauer, P. Fleischauer, *Chem. Rev.*, 1970, **70**, 199-230.
11. A. Juris, V. Balzani, F. Barigelletti, S. Campagna, P. Belser, A. von Zelewsky, *Coord. Chem. Rev.*, 1988, **84**, 85-277.
12. V. Balzani, A. Juris, M. Venturi, S. Campagna, S. Serroni, *Chem. Rev.*, 1966, **96**, 759-833.
13. (a) Y. Ohsawa, M. K. DeArmond, K. W. Hanck, D. E. Morris, *J. Am. Chem. Soc.*, 1983, **105**, 6522-6524; (b) Y. Ohsawa, M. H. Whangho, K. W. Hanck, M. K. DeArmond, *Inorg. Chem.*, 1984, **23**, 3426-3428; (c) D. E. Morris, K. W. Hanck, M. K. DeArmond, *J. Am. Chem. Soc.*, 1983, **105**, 3032-3038; (d) C. M. Elliott, *J. Chem. Soc. Chem. Commun.*, 1980, p 261; (e) G. A. Heath, L. J. Yellowlees, P. S. Braterman, *Chem. Phys. Lett.*, 1982, **92**, 646-648; (f) Y. Ohsawa, M. K. DeArmond, K. W. Hanck, C. G. Moreland, *J. Am. Chem. Soc.*, 1985, **107**, 5383-5386; (g) S. M. Angel, M. K. DeArmond, R. J. Donohoe, K. W. Hanck, D.H. Wertz, *J. Am. Chem. Soc.*, 1984, **106**, 3688-3689; (h) R. F. Dallinger, W. H. Woodruff, J. Am. Chem. Soc., 1979, 101, 4391-4393; (i) K. M, Omberg, J. R. Schoonover, J. A. Treadway, L. M.

Leasure, R. B. Dyer, T. J. Meyer, J. Am. Chem. Soc., 1997, 119, 7013-7018.

14. F. E. Lytle, D. M. Hercules, *J. Am. Chem. Soc.*, 1969, **91**, 253-257.
15. G. Wulfsberg, *Inorganic Chemistry*, University Science Books, 2000.

Chapter 4

Basic Concepts about CO_2 Reduction

4.1. Introduction

In the last years, the increasing world energy consumption has required a huge amount of energetic resources. In 2001 the worldwide energy consumption was 4.3 x 10^{20} J[1] (the 86% of which obtained by fossil resources), in 2012 this value increased to 5.8 x 10^{20} J[2] and it is expected to be triple within 2100[3]. Clearly, sooner or later, fossil resources alone will not satisfy the global energy demand. Moreover, the mass consumption of "fossil fuels" leads to an increasing amount of atmospheric CO_2, which leads to serious environmental problems, e.g. global warming[4] and greenhouse effect.[5,6] Such problems have involved our planet for over a century. Reducing CO_2 in order to obtain energy-rich chemicals, such as CO and HCOOH, could be a solution to shortages of carbon resources and for the environmental problems.[7] Moreover the solar light is a promising candidate as renewable energy source because it is inexhaustible and almost everywhere and anytime available.[8,9] Using solar light to convert CO_2 into biomass is a process that takes place in plants by the natural photosynthesis. Using suitable systems gives the chance to mimic the natural photosynthetic systems, to take advantage of the solar light and of CO_2 reduction in order to obtain the energy-rich chemicals.[10] There are several ways to achieve this aim, e.g. electrocatalysis and photocatalysis using solar light.[11]

In the molecular photocatalytic systems for CO_2 reduction electron-transfer processes take place and it is well known that the excitation by one photon can induce electron transfer. However the one-electron reduction of CO_2 is a highly endergonic process and requires a strongly negative potential to take place (eqn.1).[12]

Moreover, controlling the selective product is very difficult due to the high activity of the radical product $CO_2^{\bullet -}$:[13]

$$CO_2 + e^- \rightarrow CO_2^{\bullet -} \qquad \text{-1.9 V vs SHE} \qquad \text{eqn.1}$$

The multielectron CO_2 reduction takes place at more positive reduction potentials and there is the formation of useful and stable products (equations 2 – 7)[14].

$2\,CO_2 + 2\,e^- \rightarrow CO + CO_3^{2-}$	-0.64 V vs SHE	eqn.2
$CO_2 + 2\,e^- + 2\,H^+ \rightarrow CO + H_2O$	-0.52 V vs SHE	eqn. 3
$CO_2 + 2\,e^- + 2\,H^+ \rightarrow HCOOH$	-0.61 V vs SHE	eqn. 4
$CO_2 + 4\,e^- + 4\,H^+ \rightarrow HCHO$	-0.48 V vs SHE	eqn. 5
$CO_2 + 6\,e^- + 6\,H^+ \rightarrow CH_3OH$	-0.38 V vs SHE	eqn. 6
$CO_2 + 8\,e^- + 8\,H^+ \rightarrow CH_4$	-0.24 V vs SHE	eqn. 7

In this thesis, the reactions considered are limited to the two-electron reduction processes that are used to obtain CO and HCOOH (eqn. 2 – 4), quite interesting species from an industrial viewpoint: CO can be easily converted in liquid hydrocarbons by the Fisher-Tropsch synthesis;[15] formic acid has been investigated as potential H_2 storage material in recent years, since it is liquid at room temperature and can be easily converted in CO_2 and H_2 with suitable catalysts in moderate condition[16] or used directly as fuels in direct formic acid fuel cells (DFAFCs).[17]

The first studies on photocatalytic CO_2 reduction were conducted by Lehn and co-workers in the early 1980s. They employed *fac*-Re(bpy)$(CO)_3$Cl complexes as photocatalysts.[18,19] This kind of compounds has proved to be selective and efficient for the CO_2 reduction but showed some drawbacks such as the absorption of these complexes limited to the UV region, the low abundance of the rhenium, the low turnover number and the necessary presence of an electron donor.[20]

Later, Willner and his co-worker developed a system for the photocatalytic CO_2-fixation into organic substrates such as malic and isocitric acid using enzymes as catalysts.[21]

More recently, Deronzier and co-workers used several Os(II) complexes as catalysts for the photocatalytic CO_2 reduction.[22] Their results show a catalytic amount of CO produced with only traces of hydrogen and that the activity of these complexes is more active than the rhenium's one. However, they noted a slower CO formation in the first 4 hours of irradiation in respect to the rhenium complexes.

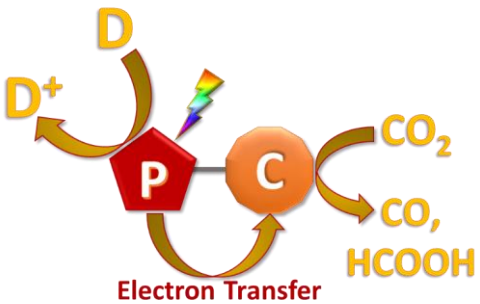

Figure 4.1. *Schematization of supramolecular system for CO_2 reduction.*

In order to maximize the efficiency of the photocatalysis, it is crucial to introduce a sensitizer to the previously known catalysts. In order to use the visible light in the best way, in recent years the aim of the research has been the introduction of a link (a bridging ligand) between the photosensitizer and the catalyst (see **Figure 4.1**). To this goal, the photocatalytic reduction of CO_2 using multinuclear metal complexes that combine the redox photosensitizers (PS), which can mediate a photoinduced electron transfer from a reductant (D) to a catalyst, and the catalysts (Cat) itself, the so-called *supramolecular photocatalysts*, has been extensively investigated.[23,24]

In supramolecular photocatalysts there is a faster electron transfer between the PS and Cat subunits and this leads to an improvement of the performances of these systems with respect to the separated species in solution, due to an

increase in the photocatalysis speed and to a higher durability of the photosensitizer subunit, since the unstable intermediate state is consumed faster than in separated mixed systems.

In photocatalysis there are several steps including the photoinduced electron transfer that leads to the accumulation of electrons on the catalyst subunit. The photoinduced electron transfer can follow two different pathways: the *reductive* and the *oxidative* electron transfer. The starting step of each pathway is the absorption of a photon by the PS subunit with the formation of the excited state of the photosensitizer (*PS, eqn. 8):

$$PS - Cat \overset{hv}{\rightarrow} {}^{*}PS - Cat \qquad \text{eqn. 8}$$

After that, in the **reductive electron transfer** (or reductive quenching) the electron donor (D), a specific sacrificial agent, transfers an electron to the excited state of *PS-Cat, reducing the PS (eqn. 9):

$${}^{*}PS - Cat \rightarrow PS^{\bullet -} - Cat + D^{+} \qquad \text{eqn. 9}$$

After that, an electron transfer from the photosensitiser to the catalyst takes place (eqn. 10):

$$PS^{\bullet -} - Cat \rightarrow PS - Cat^{-} \qquad \text{eqn. 10}$$

Instead, in the **oxidative electron transfer** (or oxidative quenching) the electron transfer takes place from the *PS to the Cat, giving a charge separated species (eqn. 11):

$${}^{*}PS - Cat \rightarrow PS^{+} - Cat^{-} \qquad \text{eqn. 11}$$

After that, PS^{+} takes an electron from the electron donor D to restore the neutral species (eqn. 12):

$$PS^{+} - Cat^{-} + D \rightarrow PS - Cat^{-} + D^{+} \qquad \text{eqn. 12}$$

In this second mechanism there is a rapid intramolecular backward electron transfer that leads to less efficiency of the systems. For this reason, the more efficient systems for the CO_2 reduction proceed via reductive electron transfer.[25] The photocatalytic activities of a supramolecular photocatalyst are evaluated in terms of the following properties:[26]

1. Selectivity (Γ) for the products, i.e., the ratio of the amount of target product to the total amount of reduced products. In many cases, H_2 is generated as a by-product during the photocatalytic reaction.
   $\Gamma = [\text{target product (mol)}]/[\text{reduced compounds(mol)}]$ eqn. 13

2. Quantum yield (Φ) of the product, which is calculated using the following equation.
   $\Phi = [\text{product (mol)}]/[\text{absorbed photons(einstein)}]$ eqn. 14

3. Turnover number (TON), which indicates the stability of the photocatalyst.
   $TON = [product(mol)]/[photosensitizer\ (mol)]$ eqn. 15

4. Turnover frequency (TOF), which indicates the speed of the photocatalytic cycle.
   $TOF = TON/[reaction\ time\ (\text{min}\ or\ h)]$ eqn. 16

A brief overview of the more important components of the supramolecular systems used in literature is reported hereunder.

4.2. Redox Photosensitizer

The role of the photosensitizer in the CO_2 reduction is absorbing photons in order to mediate the electron transfer from the electron donor to the catalyst. A good photosensitizer should have the following characteristics:

1. A wide absorbance in the visible region in order to obtain an efficient utilization of the solar radiation;

2. Stability of the ground and excited state;
3. Lifetime of the excited state relatively long in order to obtain an efficient reductive quenching process;
4. Strong oxidating or reducing power in the excited state;
5. High stability of the One Electron Reduced Species (OERS) or the One Electron Oxidized Species (OEOR) produced after the mono-electron transfer process.

Moreover, in order to design an effective supramolecular system for the CO_2 reduction, the reduction potential of the photosensitizer subunit should be equal or more negative than the one of the catalyst subunit. In addition, the characteristics of the bridging ligand play an important role in the efficiency of the photocatalysis. Indeed, it is reported in literature that supramolecular systems which contain a conjugated bridging ligand could not act as effective photocatalysts.[27]

Two important indicators of the photoinduced electron transfer from the electron donor to the excited state of the photosensitizer are the quenching rate constant (k_q – obtained using a Stern-Volmer plot and the lifetime of the photosensitizer) and the quenching fraction (η_q – calculated by eqn.17):

$$\eta_q = \frac{1}{1+K_q\tau \times [Electron\ donor]} \qquad \text{eqn. 17}$$

The most employed complexes as photosensitizers for CO_2 reduction are Ru(II) diimine complexes.[28,29] These complexes present all the photophysical and redox characteristics suitable to be used as photosensitizers.[30,31]

A disadvantage of these complexes is that the one-electron reduced species of Ru(II)-diimine complexes are stable in the dark but the photoexcitation could lead to the loss of one diimine ligand with the substitution with two solvent molecules. The resulting complexes can also act as catalyst for the CO_2 reduction but could lead to the formation of by-product.[32]

With the purpose of increasing the absorption in the visible region also the Os(II)-diimine complexes have been recently studied.[33] These complexes show a wider absorption band at longer wavelengths in the visible region than their analogous complexes of Ru(II). Indeed, they present a significative singlet to triplet metal-to-ligand charge-transfer (MLCT) absorption band around 500-700 nm caused by the larger heavy-atom effect.[34] These Os(II) complexes present also shorter emission lifetimes and more negative reduction potentials respect to the corresponding Ru(II) complexes.

Moreover, recently in literature have been reported examples where Ir(II) complexes[35] and metalloporphyrines[36,37] are used as alternative photosensitizers.

4.3. Catalysts

There are several examples of catalysts for photochemical CO_2 reduction. The catalysts should accept the electron from the photosensitiser, accumulate the two electrons required for the CO_2 reduction, make one or multiple bonds to activate the CO_2 and do not evolve H_2 which competes with the CO_2 reduction reaction. Using different metal complexes in supramolecular photocatalysis gives the possibility of obtaining selectively only one product (CO or HCOOH).

As previously noted, the first catalysts for the CO_2 reduction used by Lehn and co-workers were the Re(I) carbonyl diimine complexes fac-$[Re(N\hat{}N)(CO)_3X]^{n+}$ (N^N= diimine ligand; X = Cl^-, Br^-, pyridine, PR_3, MeCN, ecc…).[20] These complexes lead to the selective formation of CO from the reduction of CO_2.[38] Some of these complexes can act also as photosensitizer because the emission lifetime of their excited state is sufficiently long.[39]

The other types of catalysts for the CO_2 reduction are two types of Ru(II) complexes: *cis*-$[Ru(N\hat{}N)_2(CO)_2]^{2+}$[40] and *cis,trans*-$Ru(N\hat{}N)(CO)_2Cl_2$[41]. These complexes are used for HCOOH formation and their selectivity depends on the solvent and the electron donor chosen.[42] However, these complexes lead to

polymerization during the photocatalytic reaction, yielding a black polymer that decreases the efficiency of the photocatalytic systems.

Also complexes of Ni(II) with macrocycle ligands are reported in literature for the selective formation of CO from CO_2 obtaining H_2 as by-product. The selectivity of these catalysts strongly depends on pH.[43,44]

Recently, also Mn(II) complexes (fac-Mn(bpy)$(CO)_3$Br) have been investigated for the photocatalytic CO_2 reduction.[45]

Finally, very recent (and rare) examples of Ir(III)[46] complexes and Co[47] and Fe[48] porphyrin complexes as catalysts for CO_2 reduction have been reported.

4.4. Electron Donors

The characteristics of the electron donor strongly affect the efficiency of the photocatalytic systems, i.e. turnover number, quantum yield and turnover frequency. In order to maximize the reductive quenching process (the initial stage in almost all photocatalytic systems) in which the excited state of the photosensitizer is reductively quenched by the sacrificial agent, this one should have the following characteristics:

1. It should be a good reducing compound, with the potential to reduce the excited state of the photosensitizer;
2. The oxidized form of the reductant should have a short lifetime: preferentially, the electron donor should undergo irreversible oxidation. If the oxidized electron donor is stable, it could lead to a back-electron transfer from the reduced photosensitizer to the oxidized form of the electron donor. This phenomenon could reduce the performances of the photocatalytic system;
3. The products of the oxidized electron donor should not inhibit the photocatalytic reaction.

For all this reasons, different classes of compounds are investigated as sacrificial agent for the photocatalytic reaction, i.e. aliphatic amine,[49] ascorbate,[50,51]

NAD(P)H model compound[52] and dihydrobenzoimidazole derivatives[53].
The action mechanisms of the last two classes of sacrificial agents, the most used in supramolecular photocatalysis, are illustrated below.

4.4.1 NAD(P)H Model Compound

The typical NAD(P)H model compound, employed as sacrificial agent in many photocatalytic reactions of CO_2 reduction, is the 1-benzyl-1,4-dihydronicotinamide (BNAH). The working mechanism of BNAH is schematized in **Scheme 4.1**. The redox potential of BNAH ($E°(BNAH/BNAH^{\bullet+})$ = 0.57 V vs SCE[52]) is suitable to reduce the excited state of the typical Ru(II) based photosensitizer.

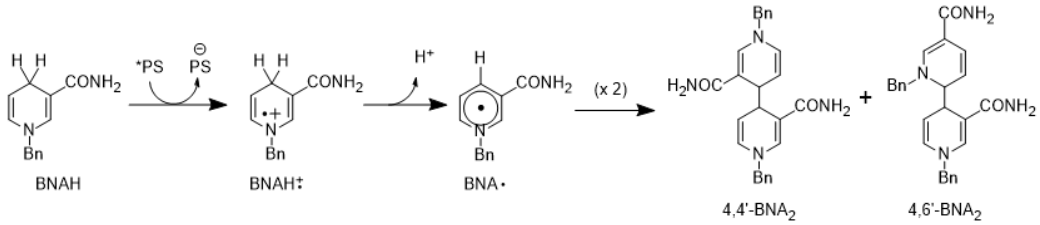

Scheme 4.1.

In the first step of the reaction, the electron transfer proceeds from BNAH to the excited state of the photosensitizer unit with the formation of the oxidized species $BNAH^{\bullet+}$. Subsequently, the deprotonation of the oxidized species $BNAH^{\bullet+}$ occurs and it leads to the formation of the radical species BNA•, but this step could be faster in presence of bases as triethanolamine (TEOA) that can capture the proton. This last product could move toward the dimerization with the formation of two possible dimers: 4,4'-BNA_2 and 4,6'-BNA_2. However, the formation of dimers causes a decrease in the photocatalytic reaction because they are stronger electron donor than BNAH ($E°^{ox}$(4,4'-BNA_2) = 0.26 V vs SCE).[54] For this reason, the BNA dimers and BNAH compete as electron donor of the excited state of the photosensitizer, but the oxidized forms of the dimers are so stable that the back electron transfer from the reduced form of the

photosensitizer to the oxidized form of the dimers occurs preferentially. This phenomenon causes a loss in the efficiency of the photocatalytic processes.

4.4.2 Dihydrobenzoimidazole Derivatives

One of the most employed dihydrobenzoimidazole derivatives is 1,3-dimethyl-2-phenyl-2,3-dihydro-1H-benzo[d]-imidazole (BIH). It presents a stronger reductive power than BNAH ($E_{1/2}^{ox}$(BIH/BIH$^{\bullet+}$) = 0.33 V vs. SCE)[55] and efficiently quenches the excited state of photosensitizer Ru(II) based. The action process is represented in **Scheme 4.2**.

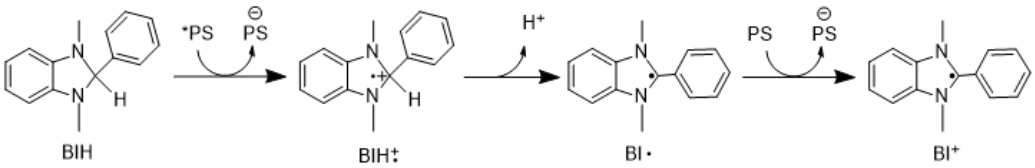

Scheme 4.2.

Instead of BNAH, BIH can donate two electrons by only one photon excitation of photosensitizer unit. The first electron is donated from BIH to the excited state of the photosensitizer, giving the oxidized form of BIH (BIH$^{\bullet+}$). This last species loses a proton very quickly, giving the radical species BI$^{\bullet}$. This species is a better electron donor than BIH (E_p^{ox}= −2.06 V vs. Fc^+/Fc)[56] and it can donate an electron also to the photosensitizer in the ground state. Also in this case the presence of a base (i. e. the TEOA) could increase the photocatalytic activity and the absence of TEOA decreases the activity because the BIH acts as proton acceptor and its protonated form ($BIHH^+$) should not work as quencher for the excited state of the photosensitizer units. Finally, the full-oxidized form BI^+ does not affect the photocatalytic activity.

References

1. Energy Information Administration International Energy Outlook; US Department of Energy: Washington, DC, 2004.
2. Energy Information Administration International Energy Outlook; US Department of Energy: Washington, DC, 2016.
3. N. S. Lewis, D. G. Nocera, *Proc. Natl. Acad. Sci. U. S. A.*, 2006, **103**, 15729−15735.
4. O. Hodnebrog, M. Etminan, J. S. Fuglestvedt, G. Marston, G. Myhre, C. J. Nielsen, K. P. Shine, T. J. Wallington, *Reviews of Geophysics*, 2013, **51**, 300 – 378.
5. T. R. Karl, K. E. Treberth, *Science*, 2003, **302**, 1719 - 1723.
6. H. Akimoto, *Science*, 2003, **302**, 1716 - 1719.
7. S. C. Roy, O. K. Varghese, M. Paulose, C. A. Grimes, *ACS Nano*, 2010, **4**, 1259 - 1278.
8. N.S. Lewis, D.G. Nocera, *Proc. Natl. Acad. Sci. USA*, 2006, **103**, 15729 - 15735.
9. S. Berardi, S. Drouet, L. Francàs, C. Gimbrt-Suriñach, M. Guttentag, C. Richmond, T. Stoll, A. Llobet, *Chem. Soc. Rev.*, 2014, **43**, 7501 - 7519.
10. V. Balzani, G. Pacchioni, M. Prato, A. Zecchina, *Rendiconti Lincei. Scienze Fisiche e Naturali*, 2019, **30**, 443 - 452.
11. C. D. Windle, R. N. Perutz, *Coordination Chemistry Reviews*, 2012, **256**, 2562 - 2570.
12. W.H. Koppenol, J.D. Rush, *J. Phys. Chem.*, 1987, **91**, 4429 - 4430.
13. W.H. Koppenol, J. D. Rush, *J. Phys. Chem.*, 1987, **91**, 4429–4430.
14. E. Fujita, *Coord. Chem. Rev.*, 1999, **373**, 185–186.
15. D. Hildebrandt, D. Glasser, B. Hausberger, B. Patel, B.J. Glasser, *Science*, 2009, **323**, 1680–1681.
16. A.K. Singh, S. Singh, A. Kumar, *Catal. Sci. Technol.*, 2016, **6**, 12 - 40.
17. X. Yu, P. G. Pickup, *J. Power Sources*, 2008, **182**, 124 - 132.

18. J. Hawecker, J.-M. Lehn, R. Ziessel, *J. Chem. Soc., Chem. Commun.*, 1983, 536 - 538.
19. J. Hawecker, J.-M. Lehn, R. Ziessel, *Helv. Chim. Acta*, 1986, **69**, 1990 - 2012.
20. J.-M. Lehn, R. Ziessel, *Proc. Natl. Acad. Sci. U.S.A.*, 1982, **79**, 701 - 704.
21. l. Willner, D. Mandler, A. Riklin, *J. Chem. Soc., Chem. Commun.*, 1986, 1022 - 1024.
22. J. Chauvin, F. Lafolet, S. Chardon-Noblat, A. Deronzier, M. Jakonen, M. Haukka, *Chem. Eur. J.*, 2011, **17**, 4313 - 4322.
23. Y. Yamazaki, H. Takeda, O. Ishitani, *J. Photochem. Photobiol. C*, 2015, **25**, 106 - 137.
24. S. Das, W. M. A. Wan Daud, *RSC adv.*, 2014, **40**, 20856 - 20893.
25. G.J. Kavarnos, N.J. Turro, *Chem. Rev.*, 1986, **86**, 401–449.
26. Y. Tamaki, O. Ishitani, *ACS Catal*, 2017, **7**, 3394 - 3409.
27. B. Gholamkhass, H. Mametsuka, K. Koike, T. Tanabe, M. Furue, O. Ishitani, *Inorg. Chem.*, 2005, **44**, 2326−2336.
28. J.V. Caspar, T.J. Meyer, *J. Am. Chem. Soc.*, 1983, **105**, 5583–5590.
29. Y. Tamaki, K. Watanabe, K. Koike, H. Inoue, T. Morimoto, O. Ishitani, *FaradayDiscuss.*, 2012, **155**, 115–127.
30. A. Juris, V. Balzani, F. Barigelletti, S. Campagna, P. Belser, A. von Zelewsky, *Coord. Chem. Rev.*, 1988, **84**, 85–277.
31. A. Ito, T.J. Meyer, *Phys. Chem. Chem. Phys.*, 2012, **14**, 13731–13745.
32. K. Kalyanasundaram, *Coord. Chem. Rev.*, 1982, **46**, 159–244.
33. Y. Tamaki, K. Koike, T. Morimoto, Y. Yamazaki, O. Ishitani, *Inorg. Chem.*, 2013, **52**, 11902–11909.
34. E.M. Kober, J.V. Caspar, R.S. Lumpkin, T.J. Meyer, *J. Phys. Chem.*, 1986, **90**, 3722–3734.
35. Y. Kuramochi, O. Ishitani, *Inorg. Chem.*, 2016, **55**, 5702−5709.

36. J. Schneider, K. Q. Vuong, J. A. Calladine, X.-Z. Sun, A. C. Whitwood, M. W. George, R. N. Perutz, *Inorg. Chem.*, 2011, **50**, 11877−11889.
37. C. D. Windle, M. V. Campian, A.-K. Duhme-Klair, E. A. Gibson, R. N. Perutz, J. Schneider, *Chem. Commun.*, 2012, **48**, 8189−8191.
38. (a) H. Takeda, K. Koike, H. Inoue, O. Ishitani, *J. Am. Chem. Soc.*, 2008, **130**, 2023–2031; (b) S. Meister, R. O. Reithmeir, A. Ogrodnik, B. Rieger, ChemCatChem, 2015, **7**, 3562 – 3569; (c) H. Hori, F.P.A. Johnson, K. Koike, O. Ishitani, T. Ibusuki, *J. Photochem. Photobiol.A*, 1996, **96**, 171–174; (d) P. Kurz, B. Probst, B. Spingler, R. Alberto, *Eur. J. Inorg. Chem.*, 2006, **2006**, 2966–2974; T. Morimoto, T. Nakajima, S. Sawa, R. Nakanishi, D. Imori, O. Ishitani, *J. Am.Chem. Soc.*, 2013, **135**, 16825–16828.
39. (a) K. Kalyanasundaram, *J. Chem. Soc. Faraday Trans.*, 1986, **82**, 2401–2415; (b) C. Kutal, M.A. Weber, G. Ferraudi, D. Geiger, *Organometallics*, 1985, **4**, 2161–2166; (c) C. Kutal, A.J. Corbin, G. Ferraudi, *Organometallics*, 1987, **6**, 553–557.
40. H. Ishida, T. Terada, K. Tanaka, T. Tanaka, *Inorg. Chem.*, 1990, **29**, 905–911.
41. K. Sekizawa, K. Maeda, K. Domen, K. Koike, O. Ishitani, *J. Am. Chem. Soc.*, 2013, **135**, 4596–4599.
42. Y. Kuramochi, J. Itabashi, K. Fukaya, A. Enomoto, M. Yoshida, H. Ishida, *Chem.Sci.*, 2015, **6**, 3063–3074.
43. K. Mochizuki, S. Manaka, I. Takeda, T. Kondo, *Inorg. Chem.*, 1996, **35**, 5132–5136.
44. M. Bourrez, F. Molton, S. Chardon-Noblat, A. Deronzier, *Angew. Chem. Int. Ed.50*, 2011, 9903–9906.
45. H. Takeda, H. Koizumi, K. Okamoto, O. Ishitani, *Chem. Commun.*, 2014, **50**, 1491–1493.

46. (a) S. Sato, T. Morikawa, T. Kajino, O. Ishitani, *Angew. Chem. Int. Ed.*, 2013, **52**, 988–992; (b) R.O. Reithmeier, S. Meister, B. Rieger, A. Siebel, M. Tschurl, U. Heiz, E. Herdtweck, *Dalton Trans.*, 2014, 43, 13259–13269.

47. (a) T. Dhanasekaran, J. Grodkowski, P. Neta, P. Hambright, E. Fujita, *J. Phys. Chem.A*, 1999, **103**, 7742–7748; (b) D. Behar, T. Dhanasekaran, P. Neta, C.M. Hosten, D. Ejeh, P. Hambright, E. Fujita, *J. Phys. Chem. A*, 1998, **102**, 2870–2877.

48. J. Grodkowski, D. Behar, P. Neta, P. Hambright, *J. Phys. Chem. A*, 1997, **101**, 248–254.

49. X. Ci, D.G. Whitten, Light-induced redox reactions of dyes, metal complexes and amines: one- vs. two-electron transfer reactions and C–C bond cleavage process, in: M.A. Fox, M. Chanon (Eds.), Photoinduced Electron Transfer Part C, Elsevier, Amsterdam, 1998, pp. 555–561.

50. C. Bachmann, B. Probst, M. Guttentag, R. Alberto, *Chem. Commun.*, 2014, **50**, 6737–6739.

51. B.H.J. Bielski, A.O. Allen, H.A. Schwarz, *J. Am. Chem. Soc.*, 1981, **103**, 3516–3518.

52. S. Fukuzumi, S. Koumitsu, K. Hironaka, T. Tanaka, *J. Am. Chem. Soc.*, 1987, **109**, 305−316.

53. Y. Tamaki, K. Koike, T. Morimoto, O. Ishitani, *J. Catal.*, 2013, **304**, 22–28.

54. M. Patz, Y. Kuwahara, T. Suenobu, S. Fukuzumi, *Chem. Lett.*, 1997, **26**, 567−568.

55. E. Hasegawa, S. Takizawa, T. Seida, A. Yamaguchi, N. Yamaguchi, H. Chiba, T. Takahashi, H. Ikeda and K. Akiyama, *Tetrahedron*, 2006, **62**, 6581-6588.

56. X.-Q. Zhu, M.-T. Zhang, A. Yu, C.-H. Wang, J.-P. Cheng, *J. Am. Chem. Soc.*, 2008, **130**, 2501−2516.

Chapter 5

Photocatalytic CO_2 Reduction by Multinuclear Metal Complexes

In Chapter 4 the essential elements to obtain efficient supramolecular systems for the CO_2 reduction are discussed. For the purpose of obtaining supramolecular complexes that can efficiently integrate the suitable photosensitizers and catalysts subunits, three different bridging ligands (shown in **Figure 5.1**) were designed and prepared, and their photophysical and redox properties studied. Photocatalytic properties have been performed in collaboration with Professor Osamu Ishitani from Tokyo Institute of Technology.

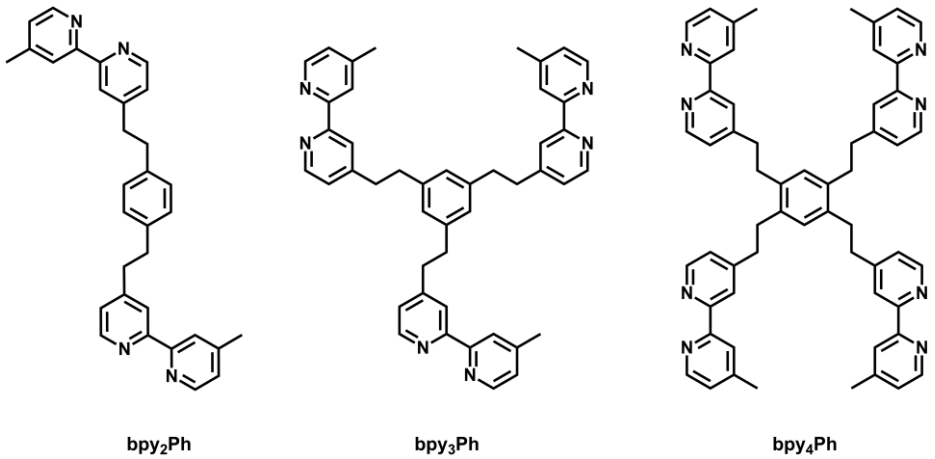

Figure 5.1. *Molecular structure of the synthesized ligands.*

The ligands designed are very versatile because they present a different number of chelating sites (the bipyridine subunits) connected by aromatic rings. This allows the assembling of metal complexes with a different number of photosensitizers and catalysts subunits, therefore it gives the possibility of analysing the effect on the photocatalytic activity of supramolecular systems with different ratios of photosensitizer and catalyst units.

Another reason lead the design of the ligands and their metal complexes: in most literature data, the bridging ligands used to integrate metal subunits acting as photosensitizers and catalysts in a single "supramolecular" array for CO_2 reduction are ethynyl bridges. This allowed to obtain fast intercomponent electron transfer processes, but inevitably kept the subunits spatially close one another, so also allowing back electron transfer processes. The structural design of the ligands reported here would allow to increase the separation between the subunits, reducing poisoning back processes. The presence of aromatic rings within the bridge could allow to favour forward electron transfer, in spite of the larger distance. If photocatalytic processes are still active in the systems here introduced (we can anticipate they are, as discussed in the following paragraphs) the consequence is to open new avenues for the design of photocatalytic mixed metal systems for CO_2 reduction occurring at the molecular level.

5.1 Ligand bpy$_2$Ph and its metal complexes

5.1.1 Synthesis of ligand bpy$_2$Ph

The synthesis of **bpy$_2$Ph** has been performed at low temperature (-33°C) under inert atmosphere in anhydrous condition in one step using 4,4'-dimethyl-2,2'-bipiridine (hereafter dmb) and 1,4-di(bromomethyl)benzene in presence of lithiumdiisopropylamide (LDA) as shown in **Scheme 1.1**.[1] The LDA was added, in slight excess, slowly dropwise to a THF solution of dmb at -33°C. LDA is a strong base suitable to remove a hydrogen from one methyl substituent on the bipyridine. Later, a THF solution of 1,4-di(bromomethyl)benzene was added. The resulting reaction mixture gradually reached room temperature and was left stirring overnight. The colour of solution changes from dark brown to pale yellow. The reaction was quenched with water. The presence of two equivalent methyl groups on the bipyridine and the reaction condition lead to the formation of a mixture of products. The crude was purified by chromatography column on silica gel using DCM/MeOH (9:1 v/v) as eluent. The first band eluted was the unreacted

dmb. The required product was isolated as second fraction and recrystallized from ethanol, leading to the final product with moderate yield (52%).

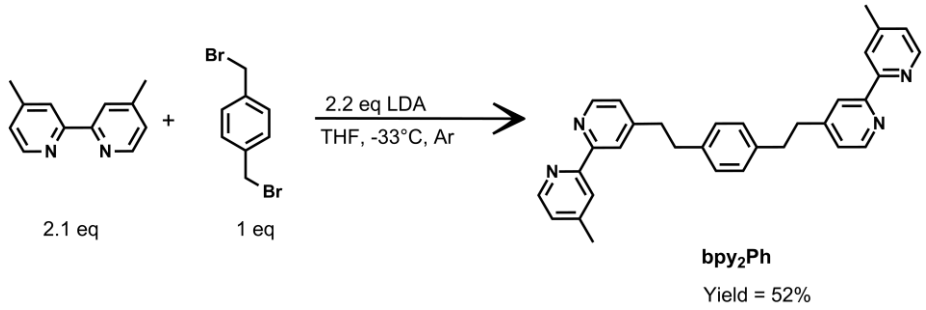

Scheme 5.1.

The characterization was performed by ^{1}H and ^{13}C NMR spectroscopy in CD_2Cl. The absence of the signal of the aliphatic protons of 1,4-di(bromomethyl)benzene at $\delta = 4.49$ ppm and the new peak at $\delta = 2.96$ ppm are the clear indication of the formation of the required product. This ligand results to be suitable to obtain a binuclear supramolecular complex that can integrate a photosensitizer subunit and a catalyst one.

5.1.2 *Synthesis of RuRe complex*

Considering the properties of the ruthenium complexes[2] (exposed in Chapter 3) and their good behaviour as photosensitizer for the CO_2 reduction[3] (as explained in Chapter 4) it has been decided to use the ligand **bpy$_2$Ph** to synthetize a binuclear complex containing as photosensitizer a subunit based on the **[Ru(dmb)$_3$]$^{2+}$** model. As reported in literature and as already discussed in Chapter 4, **Re(dmb)(CO)$_3$Cl** results to be a good catalyst for CO_2 reduction[4,5] and for this reason it has been decided to use it in this kind of supramolecular system.

For the synthesis of the final supramolecular metal complex the "cal/cam" (complex as ligand/complex as metal) approach was employed.[6] The precursor used for this synthetic strategy can be classified, as follows, relying on the characteristics of their active site:

1. *Complexes as metal:* they present, in their coordination sphere, ligands easy to remove and to exchange with other suitable ligands, thus acting as metal in relation to the latter;
2. *Complexes as ligand:* they consist in complexes that present in their coordination sphere one or more polydentate ligands with one or more free coordination sites useful for further reactions;
3. *Closed complexes:* they do not present any site suitable for other reactions unless extreme reactions.

Consequently, the synthesis of the complex **Ru(bpy$_2$Ph)** was performed starting from the ligand **bpy$_2$Ph** and the metal-complex **Ru(dmb)$_2$Cl$_2$** in a EtOH/1,2-dichloroethane 1:1 v/v mixture at reflux under argon atmosphere (**Scheme 5.2**).

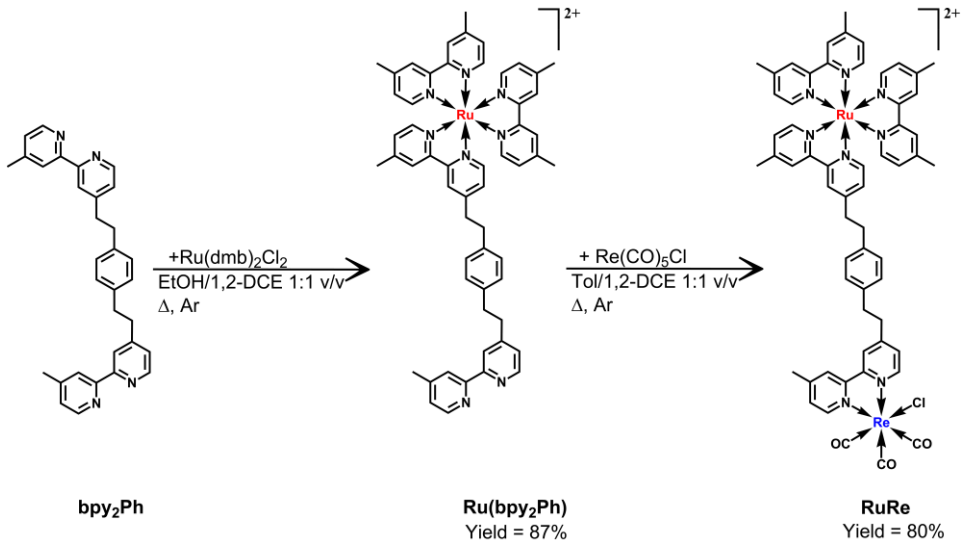

bpy$_2$Ph | **Ru(bpy$_2$Ph)** Yield = 87% | **RuRe** Yield = 80%

Scheme 5.2.

The presence of two equivalent bipyridine units in the ligand **bpy$_2$Ph** leads to the competitive formation of the by-product **Ru$_2$(bpy$_2$Ph)**. In order to minimize the formation of this latter complex, a large excess of ligand **bpy$_2$Ph** was employed (i.e. until a 4:1 ratio in respect of the metallic precursor). To remove the excess of ligand it is possible to take advantage of the different solubility of the product and the ligand in water thus separating the unreacted ligand by filtration. The required

product was obtained with a yield of 86.7%. The second synthetic step was the reaction of the ligand-complex **Ru(bpy$_2$Ph)** with the **Re(CO)$_5$Cl** metal-complex in a Toluene/1,2-dichloroethane (1:1 v/v) mixture at reflux under inert atmosphere (**Scheme 5.2**).

The synthesis was controlled using the UV-Vis absorption spectroscopy following the appearance of the **Re(dmb)(CO)$_3$Cl** ^{1}MLCT absorption band at 360 nm. The product was purified by precipitation adding NH_4PF_6 and it was washed with diethylether to remove the unreacted rhenium precursor. The final **RuRe** product was obtained with a yield of 80%.

5.1.2.1 Absorption Spectra and Photophysical Properties

The absorption spectra in acetonitrile of the new species synthesized are reported in **Figure 5.2** and the spectroscopic and photophysical data are reported in **Table 5.1**.

Table 5.1. *Photophysical properties measured in deaerated MeCN*[(a)]

	Absorption	Luminescence		
	λ_{max} /nm (ε_{460}/M^{-1}cm^{-1})[(b)]	λ_{max} / nm	τ / ns [(c)]	Φ_{em} [(c)]
Ru	460 (15300)	624	890 (120)	0.086 (0.016)
RuRe	460 (15800)	625	900 (119)	0.088 (0.016)
[Ru(dmb)$_3$]$^{2+}$[(d)]	458 (16300)	622	875	0.089[(e)]
Re(dmb)CO$_3$Cl	364 (3630) [(f)]	600[(g)]	49[(g)]	0.0057[(h)]

(a) All data are measured in MeCN at 293 K. (b) Only the low energy maximum is reported. (c) Data in parenthesis refer to air-equilibrated solution. (d) From reference 7. (e) From reference 8. (f) From reference 9. (g) From reference 10. (h) In MeTHF.

As it can be observed in **Figure 5.2**, the absorption spectrum of the mononuclear **Ru(bpy$_2$Ph)** species is characterized by a strong absorption band between 450 and 465 nm assigned to spin-allowed transition ^{1}MLCT (metal to ligand charge transfer) which involves a charge transfer from an orbital mainly centred on the Ru(II) to an orbital mainly centred on the polypyridine ligands. In the UV-Vis

region it is possible to observe an intense absorption band due to the π-π* transition centred on the orbitals of the ligands.

The spectrum of the species **RuRe** (shown in **Figure 5.2**) presents the same contributions present in the **Ru(bpy$_2$Ph)** spectrum and an additional contribution between 280 and 410 nm due to the ^{1}MLCT transition involving the Re(I) center.

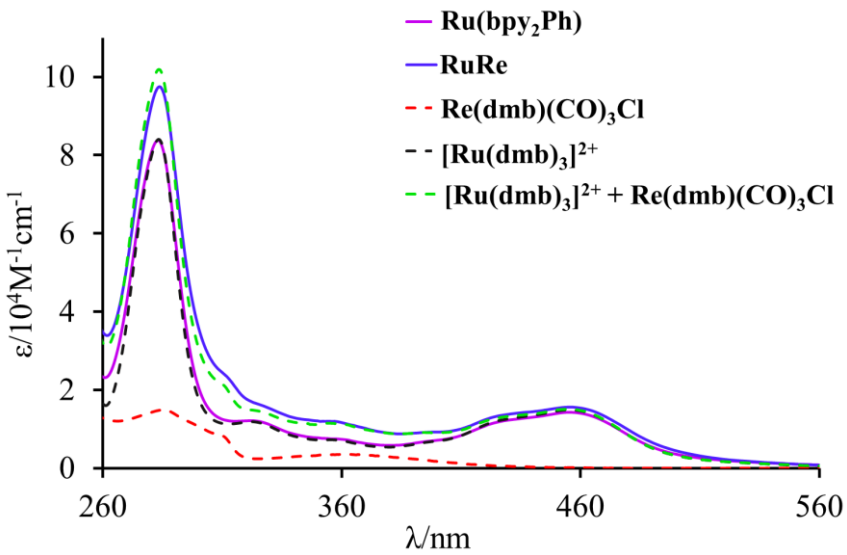

Figure 5.2. *Absorption spectra of the model species* ***[Ru(dmb)$_3$]$^{2+}$*** *(**black** dashed line),* ***Re(dmb)CO$_3$Cl*** *(**red** dashed line) and their sum (**green** dashed line) superimposed with the spectra of the species mononuclear* ***Ru(bpy2Ph)*** *(**violet** solid line) and* ***RuRe*** *(**blue** solid line).*

The sum spectrum of the model species **[Ru(dmb)$_3$]$^{2+}$** and **Re(dmb)(CO)$_3$Cl** can be superimposed to the one of the supramolecular species **RuRe**.

This suggests that there are not strong electronic interactions between the Ru(II) and Re(I) metal centers in the ground state. Consequently, the photophysical properties of each metal center are independent and additive.

All metal complexes are luminescent in acetonitrile fluid solution at room temperature (see **Figure 5.3** and **Table 5.1**). For the mononuclear species **Ru(bpy$_2$Ph),** the emission is due to the radiative deactivation of the ^{3}MLCT state, which involves the Ru(II) center and the polypyridine ligands. The emission recorded for the binuclear species **RuRe** can be overlapped with the one of the

precursor species **Ru(bpy$_2$Ph)**, regardless of the excitation wavelength and also by exciting it in the spectral range where the Re(I) absorption contribute is larger.

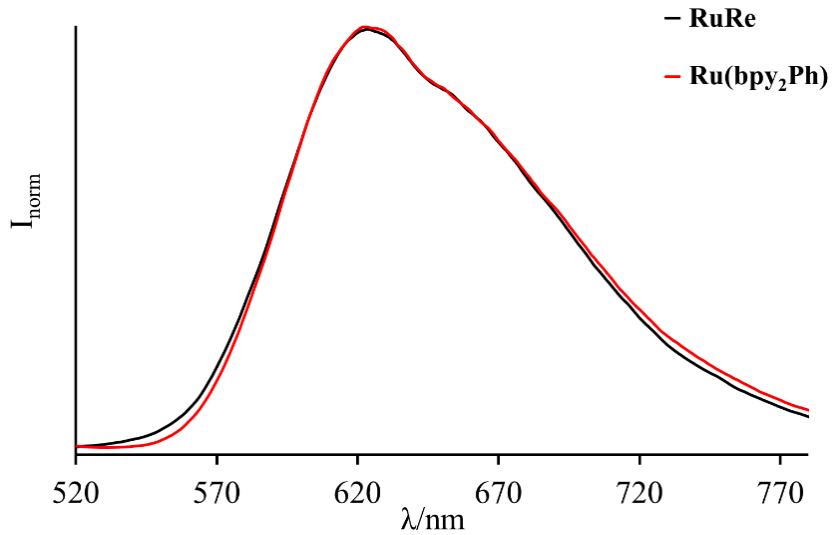

Figure 5.3. *Normalized emission spectra of **Ru(bpy2Ph)** (**red** solid line) and **RuRe** (**Black** solid line) in acetonitrile at room temperature at λ_{exc} = 450 nm.*

The excitation spectrum for the supramolecular species **RuRe** is independent from the emission wavelength.

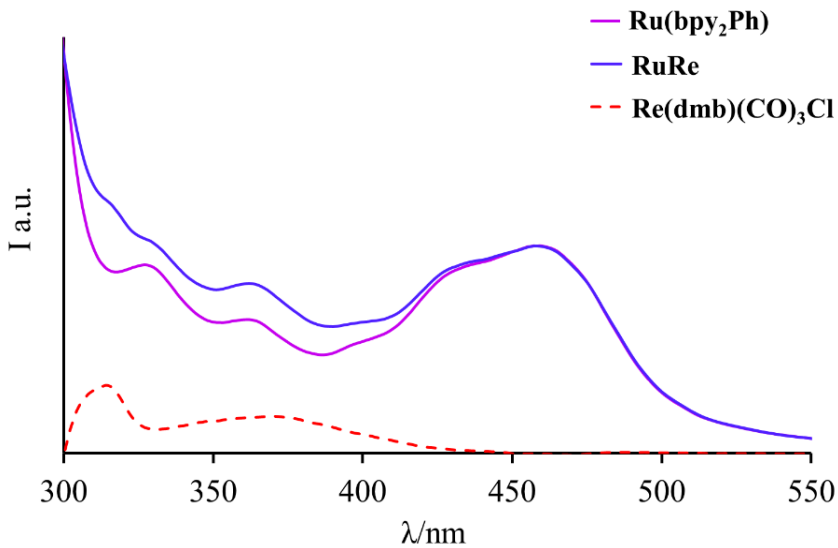

Figure 5.4. *Excitation spectra of **Ru(bpy2Ph)** (**violet** solid line) and **RuRe** (**blue** solid line) at 610 nm and difference spectrum (**red** dashed line).*

By comparing the excitation spectra of **Ru(bpy2Ph)** and **RuRe** recorded at 610 nm (see **Figure 5.4**) it can be noted that in the latter the excited Re(I) state contributes to the population of the luminescent state. This is a clear indication of the photoinduced energy transfer from the excited state of Re(I) to the Ru(II) subunits.

The emission lifetimes for the monomer and dimer are around 800 ns in deoxygenated acetonitrile solution and the emission quantum yields are almost 0.08 in both cases. These results are comparable to the ones observed for the model species **$[Ru(dmb)_3]^{2+}$**.

5.1.2.2 Redox Properties

The redox properties of the complexes **Ru(bpy$_2$Ph)** and **RuRe** have been investigated by voltametric analysis, such as cyclic, differential pulsed and square wave voltammetry. The results are reported in **Table 5.2**.

Table 5.2. *Redox properties*

	$E_{1/2}$, V vs SCE[(a)]					
	E_{Ox2}	**E_{Ox1}**	**E_{Red1}**	**E_{Red2}**	**E_{Red3}**	**E_{Red3}**
Ru		+1.14 [1]	-1.43 [1]	-1.62[1]	-1.87[1]	-2.17
RuRe	+1.38 irr	+1.14 [1]	-1.42[2]	-1.58[1]	-1.85[1]	-2.36
$[Ru(dmb)_3]^{2+}$[(b)]		+1.10 [1]	-1.45[1]			
$[Re(dmb)(CO)_3Cl]$[(c)]		+1.36 irr	-1.43 [1]			

(a) Electrochemical Properties measured at room temperature in MeCN containing 0.1 M TBAH. All values are obtained using the redox couple ferrocene/ferrocenium (395 mV vs. SCE in acetonitrile) as internal reference. The numbers in parentheses refer to the number of exchanges electrons. Irr indicates an irreversible process: in this case, the E values reported in table refer to peak potentials in pulse voltammetry experiments. (b) From reference 11. (c) From reference 10.

In the voltammogram of the **Ru(bpy$_2$Ph)** monomeric species there is a reversible oxidation process due to the oxidation process of the Ru(II) and three different

reduction processes which involve the reduction of the three different bipyridine moieties (see **Figure 5.5** and **Figure 5.6**).

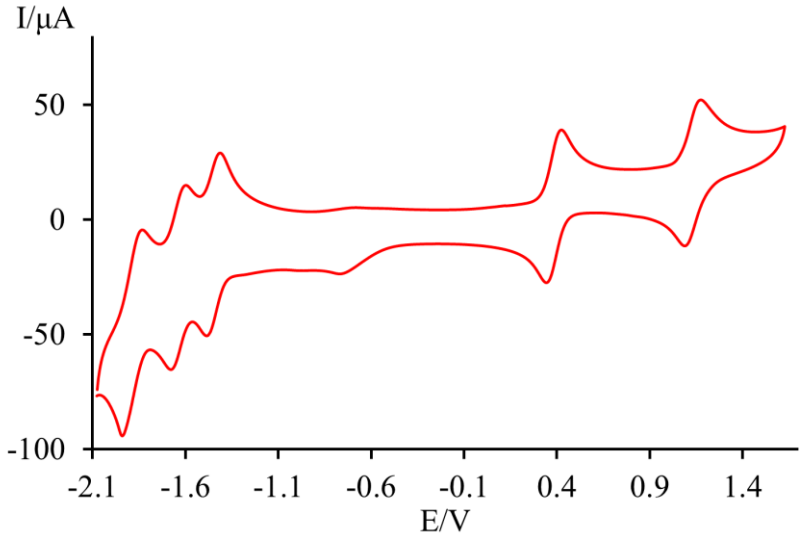

Figure 5.5. *CV analysis of* ***Ru(bpy$_2$Ph)*** *(0.5 mM) in argon purged MeCN at room temperature using Bu_4NPF_6 (0.05 M) as supporting electrolyte. As internal reference, it was used the redox couple ferrocene/ferrocenium (395 mV vs. SCE in acetonitrile). Scan rate 200 mV/s.*

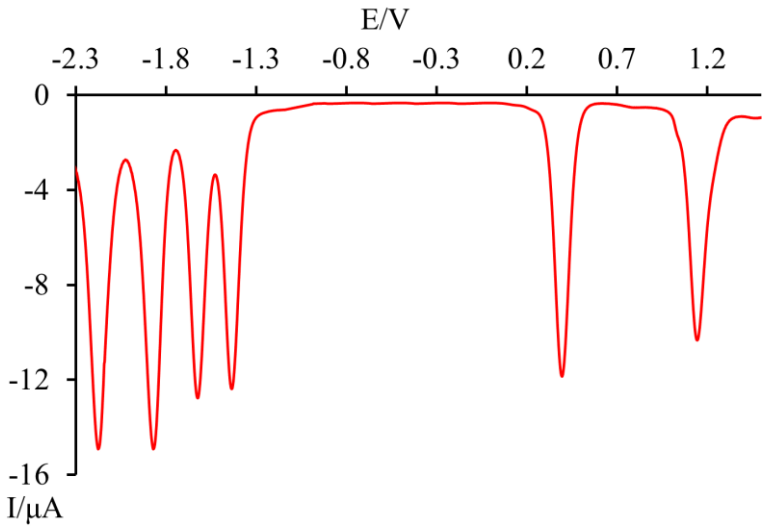

Figure 5.6. *DPV analysis of* ***Ru(bpy$_2$Ph)*** *(0.5 mM) in argon purged MeCN at room temperature using Bu_4NPF_6 (0.05 M) as supporting electrolyte. As internal reference, it was used the redox couple ferrocene/ferrocenium (395 mV vs. SCE in acetonitrile). Scan rate 20 mV/s.*

In the **RuRe** voltammograms a further oxidation process, due to the oxidation of the Re(I) metal center, is present (see **Figure 5.7** and **Figure 5.8**).

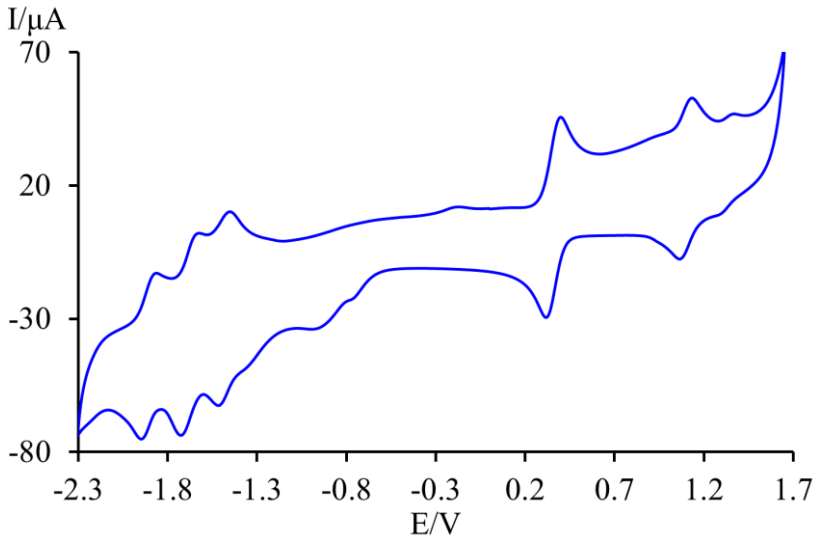

Figure 5.7. *CV analysis of **RuRe** (0.5 mM) in argon purged MeCN at room temperature using Bu_4NPF_6 (0.05 M) as supporting electrolyte. As internal reference, it was used the redox couple ferrocene/ferrocenium (395 mV vs. SCE in acetonitrile). Scan rate 200 mV/s.*

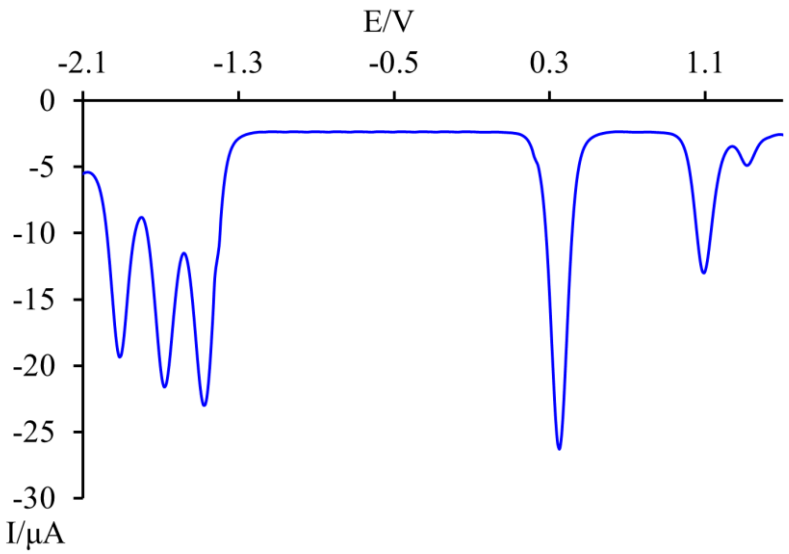

Figure 5.8. *DPV analysis of **RuRe** (0.5 mM) in argon purged MeCN at room temperature using Bu_4NPF_6 (0.05 M) as supporting electrolyte. As internal reference, it was used the redox couple ferrocene/ferrocenium (395 mV vs. SCE in acetonitrile). Scan rate 20 mV/s.*

It should be noted that in the differential pulsed voltammogram (DPV) for the **RuRe** supramolecular species the first reduction peak involves two electrons with a separation in the cyclic voltammogram between the anodic and cathodic peak of about 70 mV. This process should be assigned to the contemporaneous and independent reduction of the two bipyridine coordinates to the Ru(II) and Re(I) metal centers. The other two monoelectronic reduction processes at more negative potential are attributed to the reductions of the other two bipyridines coordinated to the Ru(II) metal complex.

The potentials found for these complexes are the same at the ones reported in literature for the model species **$[Ru(dmb)_3]^{2+}$** and **$[Re(dmb)(CO)_3Cl]$**, so it is possible to affirm that (also from an electrochemical viewpoint) the supramolecular complexes preserve the properties of the monomeric model species. The reduction potentials result to be suitable for the CO_2 reduction, because they are more negative than the reduction potential of CO_2 (-0.52 V vs SHE).[12]

5.1.2.3 Photocatalytic Analysis

The photocatalytic abilities of the binuclear **RuRe** supramolecular complex have been also investigated. In a typical run, a 3 mL CO_2-saturated mixed solution of *N*,*N*-dimethylacetamide-triethanolamine (DMA-TEOA; 5:1 v/v) containing **RuRe** (50 μM) and 1,3-dimethyl-2-phenyl-2,3-dihydro-1*H*-benzo[d]imidazole (BIH) as sacrificial electron donor was irradiated using a LED light source (530 nm, 4 mW), giving CO almost selectively. The DMA (N,N-Dimethylacetamide) was recently employed as solvent in the CO_2 reduction because it does not produce formate thanks its high stability against hydrolysis.[13] The TEOA assists the capture of CO_2 from the Re(I) catalyst subunit[14] and captures the proton generated from the oxidation process of the sacrificial agent by enhancing the photocatalytic abilities. The products of photocatalysis have been analysed by Gas Chromatography (for the quantitative analysis of CO and

H_2) and Capillary Electrophoresis (for the quantification of HCOOH formation). The results are summarized in **Table 5.3** and the time course for the product formation are shown in **Figure 5.9**.

Table 5.3. *Photocatalytic properties of **RuRe** using BIH.*[a]

	Product / μmol (TON)[b]			Φ_{CO} /%[c]	Γ_{CO}/%[a,d]
	CO	HCOOH	H_2		
RuRe	253.8 (1692)	0	0.012 (0.08)	41	99
RuRe[e]	66 (2200)	1.2 (38)	0.024 (0.8)	-	98.25
RuRe[f]	110.0 (3657 ± 29)	1.1 (36)	0.03	30 ± 1.1	99

[a]*CO_2-saturated DMA-TEOA (5:1 v/v) solution containing **RuRe** (50 μM) and BIH as sacrificial electron donor (0.1 M) was irradiated.* [b]*3-mL solution was irradiated for 20 h using a LED (530 nm, 4 mW) as a light source. TONs are calculated based on the photocatalyst used.* [c]*4-mL solution was irradiated at λ_{ex} = 480 nm (light intensity: 1 × 10^{-8} einstein s^{-1}).* [d]*The selectivity for CO production.* [e]*[**RuRe2**] = 10 μM, 60-h irradiation.* [f]*[**RuRe**] = 10 μM, 60-h irradiation.*

The quantum yield for CO production (Φ_{CO}) was around 41% for **RuRe** using 480-nm light (light intensity: 1.0 × 10^{-8} einstein s^{-1}). The selectivity for the CO formation reaches the 99%.

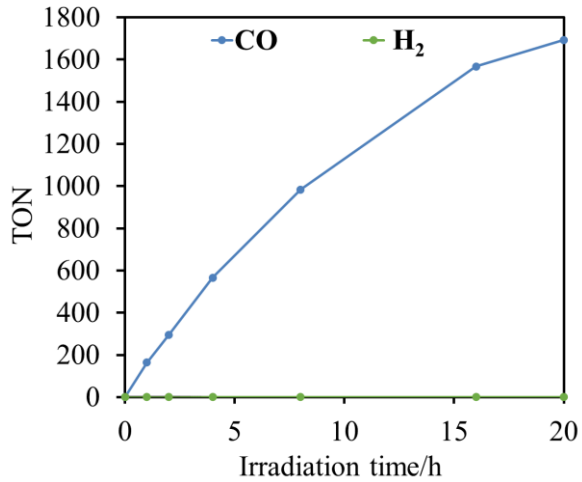

Figure 5.9. *Photocatalytic formation of CO (**blue** line) and H_2 (**green** line) as function of irradiation time using **RuRe** (50 μM) CO_2-saturated DMA-TEOA (5:1 v/v, 3 mL) solutions and BIH (0.1 M) irradiated using a LED (530 nm, 4 mW) as a light source.*

Since CO is a two-electron reduced compound of CO_2 and BIH has been reported to function as a two-electron donor,[15] it is possible to calculate the consumption of BIH during the photocatalysis experiment in these experimental conditions. The TON is expressed by the equation 1:

$$TON = [product(mol)]/[photosensitizer\ (mol)] \qquad \text{eqn. 1}$$

So, for TON_{CO} = 1692 the BIH consumed was 0.05 x 1692 = 62.2 mM, which is 85% of BIH added originally (100 mM). This could be the reason for the slower CO formation after 20 hours of irradiation.

In order to observe the durability of the supramolecular species the concentration of the binuclear **RuRe** compound was reduced to 1/5 (i.e. 10 μM) and the samples have been irradiated until 60 hours. The results are summarized in **Table 5.3** and the time course for the photocatalytic experiments are shown in **Figure 5.10**.

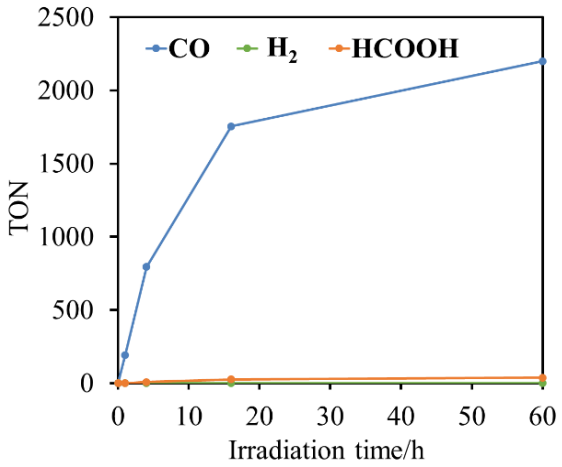

Figure 5.10. *Photocatalytic formation of CO (**blue** line), formic acid (**orange** line) and H_2 (**green** line) as function of irradiation time using **RuRe** (10 μM) CO_2-saturated DMA-TEOA (5:1 v/v, 3 mL) solutions and BIH (0.1 M) irradiated using a LED (530 nm, 4 mW) as a light source.*

After 60 hours of irradiation the turnover number for the formation of CO reached 2200. It should be noted that the starting rate of the reaction is faster than the

previous cases. For comparison, in **Table 5.3** are also reported the values obtained in the same condition for the binuclear species **RuRe** (10 μM) where the photosensitizer subunit and the catalyst subunit are connected to an ethylene chain. In this case the TON_{CO} reaches 3657.

5.2 Ligand bpy$_3$Ph and its metal complexes

5.2.1 Synthesis of ligand bpy$_3$Ph

The synthesis of **bpy$_3$Ph** ligand is reported in **Scheme 5.3**. The synthesis of **bpy$_3$Ph** has been performed at low temperature (-33°C) under inert atmosphere in anhydrous condition in one step using 4,4'-dimethyl-2,2'-bipiridine and 1,3,5-tri(bromomethyl)benzene in presence of lithiumdiisopropylamide (LDA).[1] The LDA was added in slight excess slowly dropwise to a THF solution of dmb at -33°C. LDA is a strong base suitable to remove a hydrogen from one methyl substituent on the bipyridine. Later, a THF solution of 1,3,5-tri(bromomethyl)benzene was added. The resulting reaction mixture gradually reached room temperature and was left stirring overnight. The colour of the solution changes from dark brown to pale yellow.

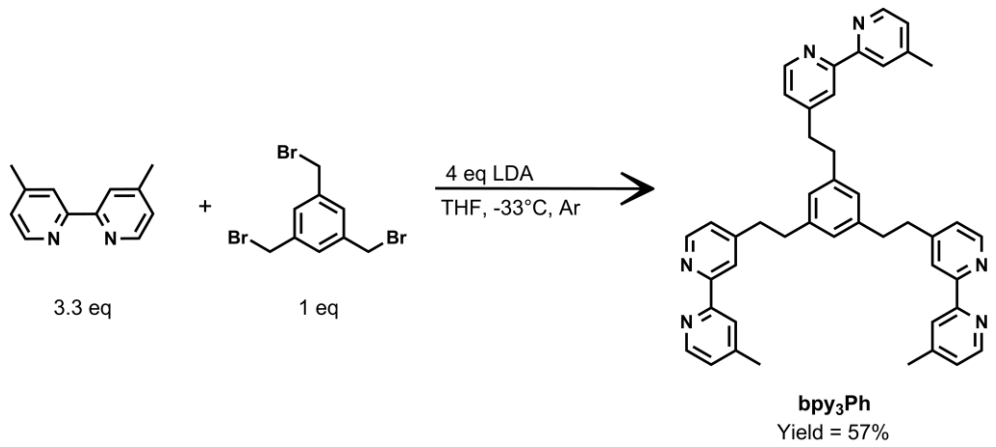

Scheme 5.3.

The reaction was quenched with water. The presence of two equivalent methyl groups on the bipyridine leads to the formation of a mixture of products. The

crude was purified by chromatography column on silica gel using DCM/MeOH (9:1 v/v) as eluent. The first eluted band is the unreacted dmb. The required product was eluted as second band and recrystallized from ethanol, leading to the final product with moderate yield (57%). The characterization was performed by ^{1}H and ^{13}C and ^{1}H-^{13}C HQSC NMR spectroscopy in CD_2Cl. The absence of the signal of the aliphatic protons of 1,3,5-tri(bromomethyl)benzene at $\delta = 4.45$ ppm and the new peak of the twelve proton of the ethylene chains at $\delta = 2.82$ ppm are the clear indication for the formation of the required product. This ligand results to be suitable to obtain different trinuclear complexes that integrate photosensitizer and catalyst subunits with different ratios.

5.2.2 Synthesis of RuRe2 and Ru2Re Supramolecular Complexes

The synthesis of the supramolecular species **RuRe2** and **Ru2Re** are represented in **Scheme 5.4**.

The synthesis was performed with the "cal/cam" approach employed also for the **RuRe** supramolecular complex. In order to obtain complexes with different number of photosensitizer subunits, the ligand **bpy$_3$Ph** was put to react with one, two or three equivalents of the metal-complex **Ru(dmb)$_2$Cl$_2$** in a EtOH/MeOH 1:1 v/v mixture at reflux under argon atmosphere (**Scheme 5.4**). The presence of three equivalent bipyridine units in the ligand **bpy$_3$Ph** leads to the competitive formation of a mixture of the three different supramolecular complexes **Ru(bpy$_3$Ph)**, **Ru$_2$(bpy$_3$Ph)** and **Ru$_3$(bpy$_3$Ph)**, charged respectively +2, +4 and +6. The mixture was separated by ionic exchange chromatography taking advantage of the different charge of the metal complexes using CM Sephadex C-25, a ionic exchange resin, as stationary phase and a solution of NaCl in H_2O/acetone (5:3 v/v) as eluent. Increasing progressively the ionic force of the medium, by changing the concentration of NaCl in solution, leads to the selective elution of the three different complexes from the least to the most charged one.

The presence in **Ru(bpy$_3$Ph)** and **Ru$_2$(bpy$_3$Ph)** of respectively two and one free dmb moieties gives the possibility to use these complexes to react with a suitable

precursor in order to obtain the supramolecular complexes, which also present the catalyst subunit.

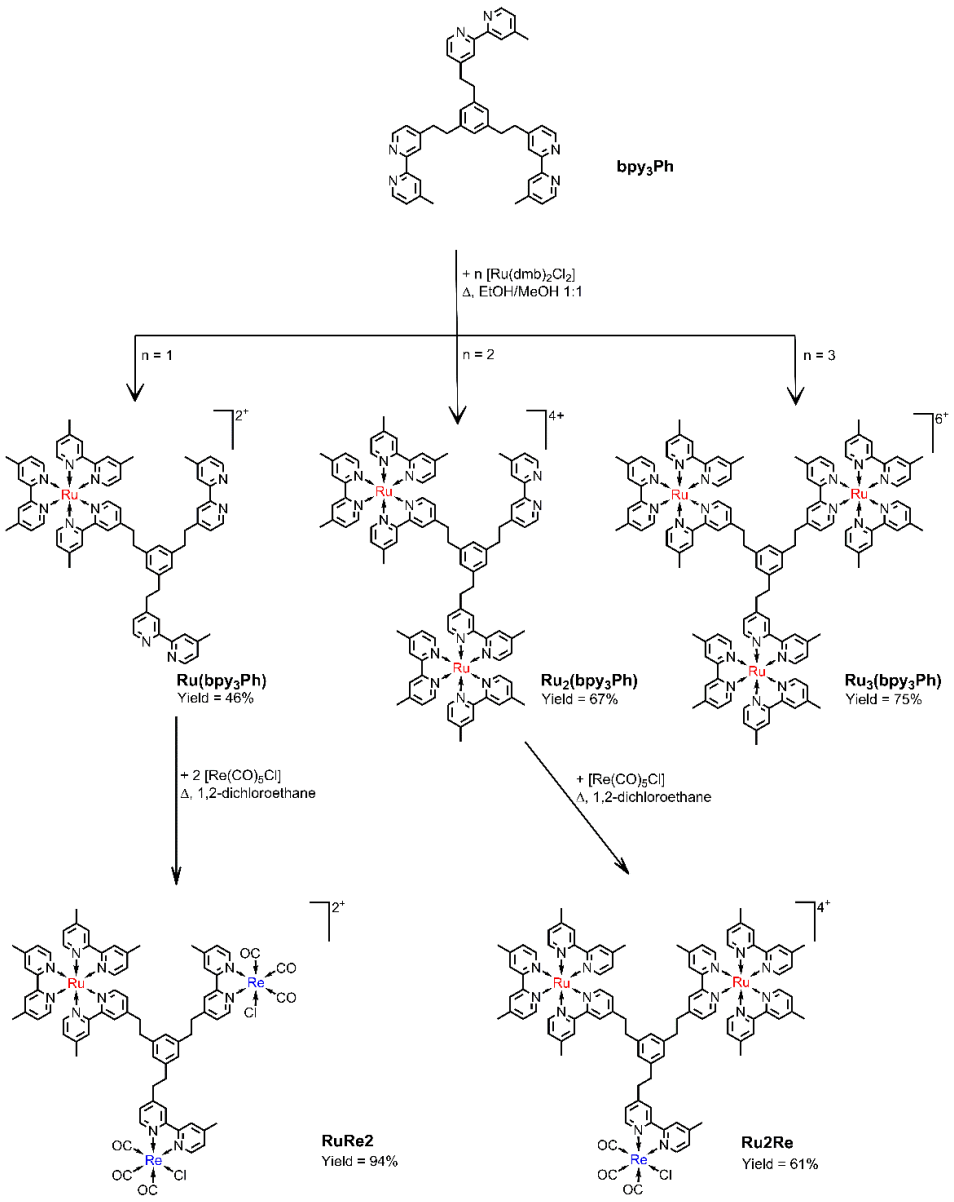

Scheme 5.4.

Consequently, the second synthetic step was the reaction of the ligand-complex, **Ru(bpy$_3$Ph)** or **Ru$_2$(bpy$_3$Ph)**, with a strong excess of **Re(CO)$_5$Cl** in 1,2-dichloroethane at reflux under inert atmosphere (**Scheme 5.4**).

The reaction was monitored by UV-Vis absorption spectroscopy following the presence of the new **Re(dmb)(CO)$_3$Cl** ^{1}MLCT absorption band at 360 nm. The product was purified by precipitation adding NH_4PF_6 and it was washed with diethylether to remove the unreacted rhenium precursor. The final **Ru2Re** and **RuRe2** products were obtained with a yield of 61% and 94% respectively.

5.2.2.1 Absorption Spectra and Photophysical Properties

The absorption spectra of the species **Ru(bpy$_3$Ph)**, **Ru$_2$(bpy$_3$Ph)** and **Ru$_3$(bpy$_3$Ph)** recorded in acetonitrile are shown in **Figure 5.11** and all the photophysical properties are summarized in **Table 5.4**.

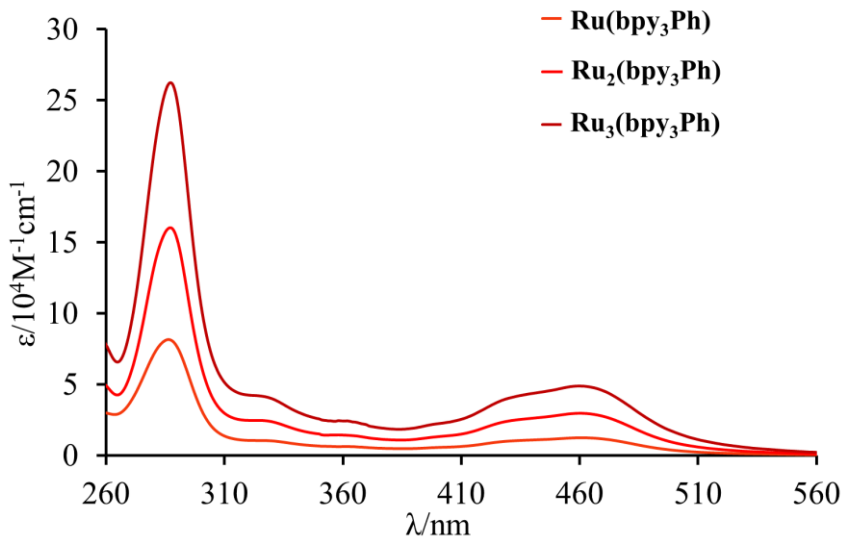

Figure 5.11. *Absorption spectra of the species* ***Ru(bpy$_3$Ph)***, ***Ru$_2$(bpy$_3$Ph)*** *and* ***Ru$_3$(bpy$_3$Ph)*** *in acetonitrile.*

All the absorption spectra of the precursor species are characterized by a strong absorption band between 450 and 465 nm assigned to spin-allowed transitions ^{1}MLCT (metal to ligand charge transfer) which involve a charge transfer from an orbital mainly centred on the Ru(II) to an orbital mainly centred on the polypyridine ligands.

Table 5.4. *Photophysical properties measured in deaerated MeCN*[a]

	Absorption	Luminescence		
	λ_{max} /nm (ε_{460}/$M^{-1}cm^{-1}$)[b]	λ_{max} / nm	τ / ns [c]	Φ_{em} [c]
Ru(bpy$_3$Ph)	460 (14760)	624	878 (120)	0.085 (0.016)
Ru$_2$(bpy$_3$Ph)	460 (31180)	625	851 (115)	0.086 (0.016)
Ru$_3$(bpy$_3$Ph)	460 (44500)	625	847 (117)	0.087 (0.016)
RuRe2	460 (14500)	624	867 (119)	0.085 (0.016)
Ru2Re	460 (28550)	625	852 (117)	0.086 (0.016)
[Ru(dmb)$_3$]$^{2+}$[d]	458 (16300)	622	875	0.089[e]
Re(dmb)CO$_3$Cl	364 (3630) [f]	600[g]	49[g]	0.0057[h]

(a) All data are measured in MeCN at 293 K. (b) Only the low energy maximum is reported. (c) Data in parenthesis refer to air-equilibrated solution. (d) From reference 7. (e) From reference 8. (f) From reference 9. (g) From reference 10. (h) In MeTHF.

The increase of the molar extinction coefficient moving from the mononuclear to the trinuclear species is due to the higher number of metal centers, but the shapes of the spectra are very similar between them. In the UV-Vis region it is possible to observe an intense absorption band, at around 285 nm, due to the π-π* transition centred on the orbitals of the ligands.

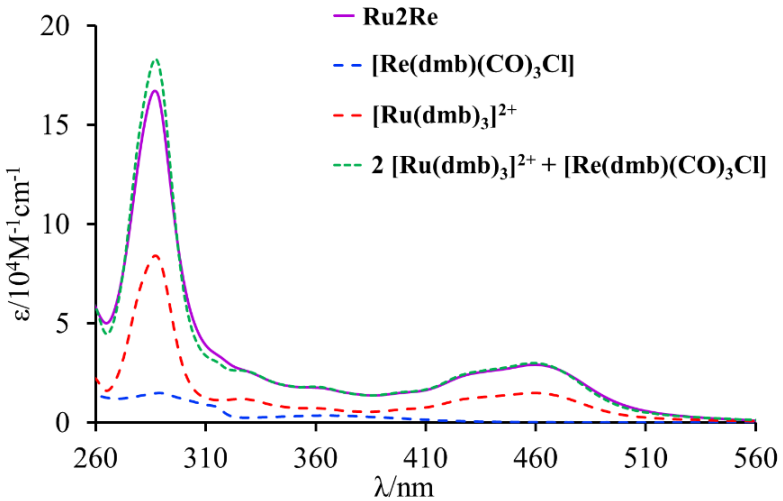

Figure 5.12. *Absorption spectra of the model species **[Ru(dmb)$_3$]$^{2+}$** (**red** dashed line), **Re(dmb)CO$_3$Cl** (**blue** dashed line) and their sum (**green** dotted line) superimposed with the spectra of the species trinuclear **Ru2Re** (**violet** solid line).*

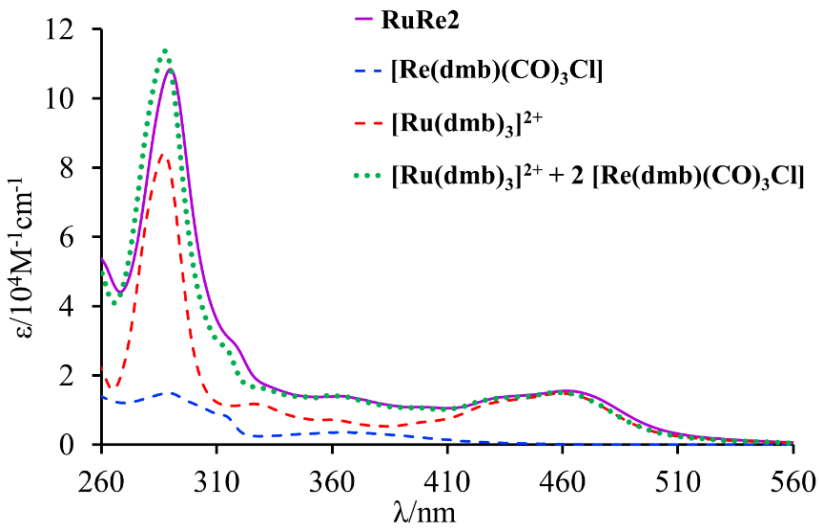

Figure 5.13. *Absorption spectra of the model species* ***[Ru(dmb)$_3$]$^{2+}$*** *(**red** dashed line),* ***Re(dmb)CO$_3$Cl*** *(**blue** dashed line) and their sum (**green** dotted line) superimposed with the spectra of the species trinuclear* ***RuRe2*** *(**violet** solid line).*

The absorption spectra of the species **RuRe2** and **Ru2Re** (shown in **Figure 5.12** and **Figure 5.13**) present the same contributions as the precursor species and an additional contribution between 280 and 410 nm due to the ^{1}MLCT transition involving the Re(I) center.[16]

The weighed sum spectra of the model species **[Ru(dmb)$_3$]$^{2+}$** and **Re(dmb)(CO)$_3$Cl** can be superimposed to the ones of the supramolecular species **Ru2Re** and **RuRe2**. This suggests that there are no strong electronic interactions between the Ru(II) and Re(I) metal centers in the ground state. Consequently, the photophysical properties of each metal center are independent and additive.

All metal complexes are luminescent in acetonitrile fluid solution at room temperature (see **Figure 5.14**, **Figure 5.15** and **Table 5.4**).

For the mononuclear species **Ru(bpy$_3$Ph)** and the binuclear species **Ru$_2$(bpy$_3$Ph)**, the emission is due to the radiative deactivation of the ^{3}MLCT state, which involves the Ru(II) center and the polypyridine ligand. The emission recorded for the trinuclear species **Ru2Re** and **RuRe2** can be overlapped with the one of the precursor species **Ru(bpy$_3$Ph)** and **Ru$_2$(bpy$_3$Ph)**, regardless of the

excitation wavelength (see **Figure 5.14** and **Figure 5.15**), even by exciting them in the spectral range where the Re(I) absorption contribute is bigger.

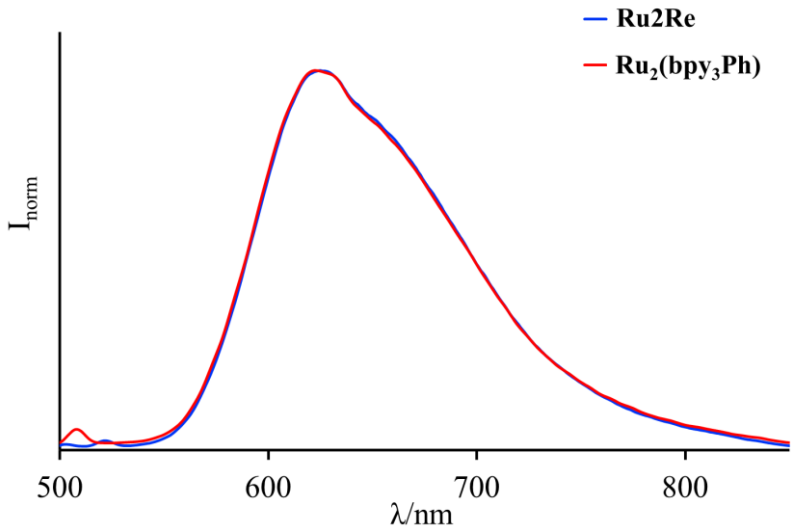

Figure 5.14. *Normalized emission spectra of* ***Ru$_2$(bpy$_3$Ph)*** *(**red** solid line) and* ***Ru2Re*** *(**blue** solid line) in acetonitrile at room temperature at λ_{exc} = 450 nm.*

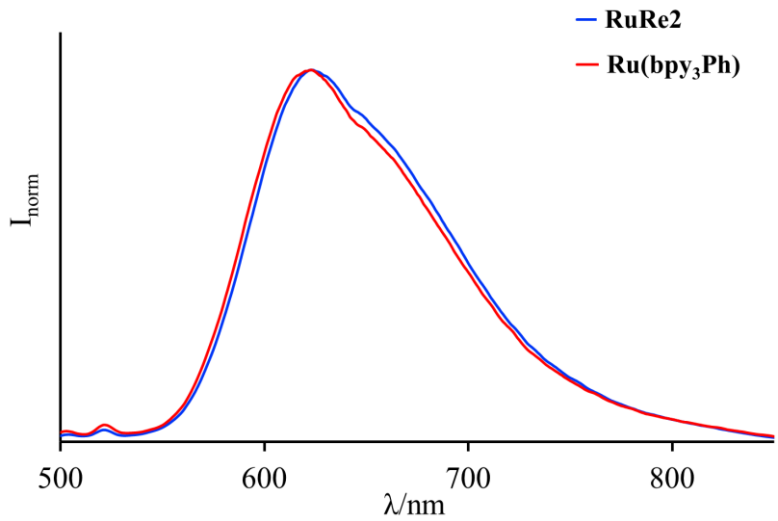

Figure 5.15. *Normalized emission spectra of* ***Ru(bpy$_3$Ph)*** *(**red** solid line) and* ***RuRe2*** *(**blue** solid line) in acetonitrile at room temperature at λ_{exc} = 450 nm.*

The emission quantum yields and lifetimes of the species **Ru2Re** and **RuRe2** are independent of the presence of the Rhenium subunit(s). All these results give the possibility to affirm that there are no strong electronic interactions between the excited photosensitizer Ru(II) subunit(s) and the catalysts Re(I) subunit(s).

5.2.2.2 Redox Properties

The redox properties of the precursor complexes **Ru(bpy$_3$Ph)** and **Ru$_2$(bpy$_3$Ph)** and the final trinuclear complexes **Ru2Re** and **RuRe2** have been investigated by voltametric analysis, such as cyclic, differential pulsed and square wave voltammetry. The results are summarized in **Table 5.5**.

Table 5.5. *Redox properties.*

	$E_{1/2}$, V vs SCE[(a)]				
	E_{Ox2}	**E_{Ox1}**	**E_{Red1}**	**E_{Red2}**	**E_{Red3}**
Ru(bpy$_3$Ph)		+1.15 [1]	-1.44 [1]	-1.63[1]	-1.85[1]
Ru$_2$(bpy$_3$Ph)		+1.15 [2]	-1.43 [2]	-1.61[2]	-1.89[2]
Ru$_3$(bpy$_3$Ph)		+1.17 [3]	-1.45 [3]	-1.60[3]	-1.92[3]
Ru2Re	+1.38 irr	+1.14 [2]	-1.42[3]	-1.58[2]	-1.85[2]
RuRe2	+1.36 irr	+1.14 [1]	-1.41[3]	-1.67[1]	-1.88[1]
[Ru(dmb)$_3$]$^{2+}$[(b)]		+1.10 [1]	-1.45[1]		
[Re(dmb)(CO)$_3$Cl][(c)]		+1.36 irr	-1.43 [1]		

(a) Electrochemical Properties measured at room temperature in MeCN containing 0.1 M TBAH. All values are obtained using the redox couple ferrocene/ferrocenium (395 mV vs. SCE in acetonitrile) as internal reference. The numbers in parentheses refer to the number of exchanges electrons. Irr indicates an irreversible process: in this case, the E values reported in table refer to peak potentials in pulse voltammetry experiments. (b) From reference 11. (c) From reference 10.

In the voltammograms of the **Ru(bpy$_3$Ph)** and **Ru$_2$(bpy$_3$Ph)** species it is possible observing a reversible oxidation process due to the oxidation process of the Ru(II) and three different reduction processes which involve the reduction of the three different bipyridine moieties (see **Figure 5.16**).

In the **Ru2Re** and **RuRe2** voltammograms a further irreversible oxidation process, due to the oxidation of the Re(I) metal center, is present (see **Figures 5.17**, **5.18**, **5.19** and **5.20**). It should be noted that in the differential pulsed voltammogram for the **Ru2Re** supramolecular species the first reduction peak involves three electrons (see voltammogram in **Figure 5.17**) with a separation in

the cyclic voltammogram (**Figure 5.18**) between the anodic and cathodic peak of about 70 mV.

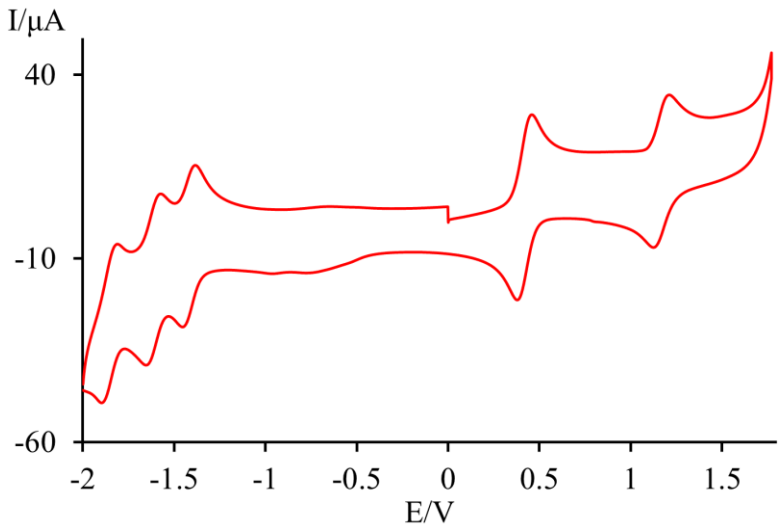

Figure 5.16. *Cyclic voltammogram of* ***Ru(bpy$_3$Ph)*** *(0.5 mM) in argon purged MeCN at room temperature using Bu_4NPF_6 (0.05 M) as supporting electrolyte. As internal reference, it was used the redox couple ferrocene/ferrocenium (395 mV vs. SCE in acetonitrile). Scan rate 200 mV/s.*

This process should be assigned to the contemporaneous and independent reductions of the three bipyridines coordinated to the Ru(II) and Re(I) metal center. The other two dielectronic reduction processes, at more negative potential, are attributed to the reductions of the other two bipyridines coordinated to the Ru(II) metal complexes.

The same conclusions could be reached also for the trinuclear species **RuRe2**. In the differential pulsed voltammogram of the **RuRe2** supramolecular species the first reduction peak involves three electrons (see the differential pulsed voltammogram in **Figure 5.19**) with a separation in the cyclic voltammogram (**Figure 5.20**) between the anodic and cathodic peak of about 70 mV. This process should be assigned to the contemporaneous and independent reductions of the three bipyridines coordinated to the Ru(II) and Re(I) metal centers.

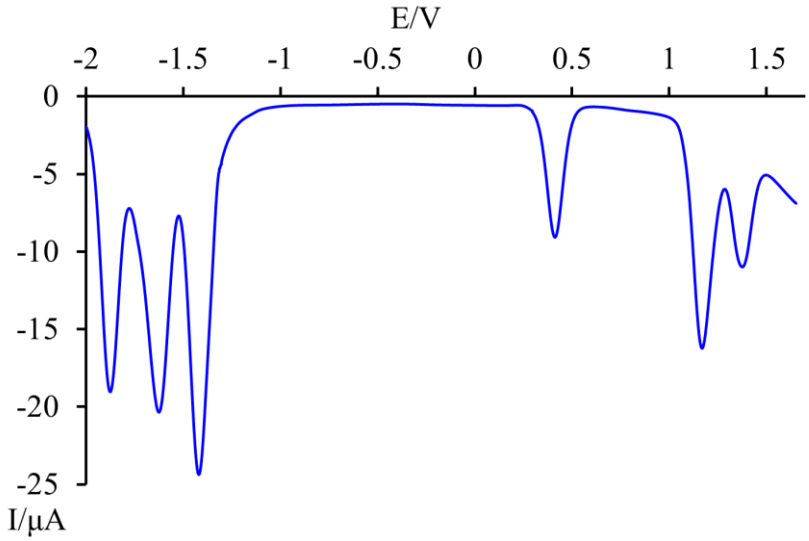

Figure 5.17. *DPV analysis of **Ru2Re** (0.5 mM) in argon purged MeCN at room temperature using Bu_4NPF_6 (0.05 M) as supporting electrolyte. As internal reference, it was used the redox couple ferrocene/ferrocenium (395 mV vs. SCE in acetonitrile). Scan rate 20 mV/s.*

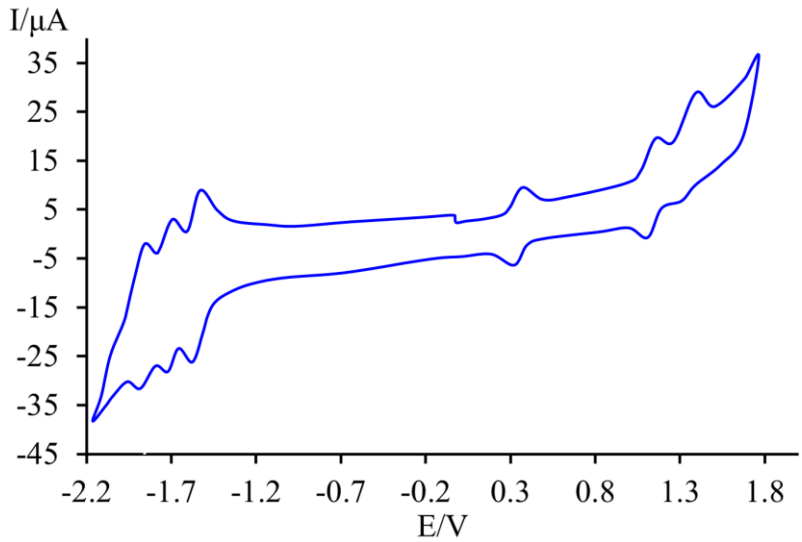

Figure 5.18. *Cyclic voltammogram of **Ru2Re** (0.5 mM) in argon purged MeCN at room temperature using Bu_4NPF_6 (0.05 M) as supporting electrolyte. As internal reference, it was used the redox couple ferrocene/ferrocenium (395 mV vs. SCE in acetonitrile). Scan rate 200 mV/s.*

The other two monoelectronic reduction processes, at more negative potential, are attributed to the reductions of the other two bipyridines coordinated to the Ru(II) metal complexes.

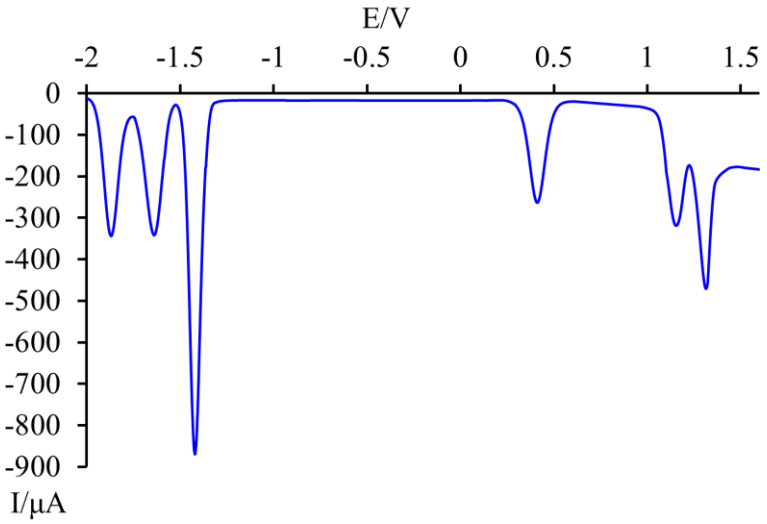

Figure 5.19. *Differential pulsed voltammogram of **RuRe2** (0.5 mM) in argon purged MeCN at room temperature using Bu_4NPF_6 (0.05 M) as supporting electrolyte. As internal reference, it was used the redox couple ferrocene/ferrocenium (395 mV vs. SCE in acetonitrile). Scan rate 20 mV/s.*

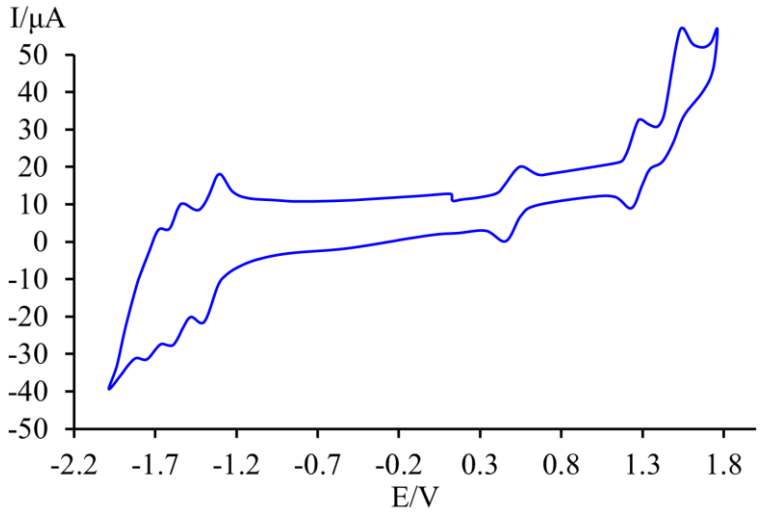

Figure 5.20. *Cyclic voltammogram of **RuRe2** (0.5 mM) in argon purged MeCN at room temperature using Bu_4NPF_6 (0.1 M) as supporting electrolyte. As internal reference, it was used the redox couple ferrocene/ferrocenium (395 mV vs. SCE in acetonitrile). Scan rate 200 mV/s.*

The analysis of the redox behaviour of the trinuclear components confirms that the metal subunits are electrochemically independent.

5.2.2.3 Photocatalysis Studies

The photocatalytic abilities of the trinuclear **Ru2Re** and **RuRe2** supramolecular complexes are also investigated. The photocatalysis analyses are performed in CO_2-satured atmosphere using a concentration of 50 μM of photosensitizer subunit to normalize the absorption properties of the complexes and compare their properties. In a typical run, a 3 mL CO_2-saturated mixed solution of *N*,*N*-dimethylacetamide/triethanolamine (DMA/TEOA; 5:1 v/v) containing **RuRe2** (50 μM) or **Ru2Re** (25 μM) and 1-benzyl-1,4-dihydronicotinamide (BNAH; 0.1 M) as a sacrificial electron donor was irradiated using a LED light source (530 nm, 4 mW), giving CO almost selectively. The DMA (N,N-Dimethylacetamide) was recently employed as solvent in the CO_2 reduction because it does not produce formate thanks to its high stability against the hydrolysis.[13] The TEOA assists the capture of CO_2 from the Re(I) catalyst subunit[14] and captures the proton generated from the oxidation process of the sacrificial agent[12] by enhancing the photocatalytic abilities. The products of photocatalysis have been analysed by Gas Chromatography (for the quantitative analyses of CO and H_2) and Capillary Electrophoresis (for the quantification of HCOOH formation). The results are summarized in **Table 5.6** and the time courses for the products formation are shown in **Figure 5.21**.

From the photocatalytic analysis the TONs for the CO formation are 216 for the supramolecular **Ru2Re** species and 225 for the supramolecular **RuRe2** species. The analysis of Ru-C_n-Re complexes where the **$[Ru(dmb)_3]^{2+}$** moiety and the **$Re(dmb)(CO)_3Cl$** moiety are connected with a different length of alkyl chain demonstrates that there is a strong dependence on the number of carbon atoms of the bridging ligand.[17] In detail, for Ru-C_n-Re complex where n = 2 the TON is 180 and this value decreases by increasing the length of the alkyl chain, reaching 120 for n = 4.[18] These values are lower than the values obtained for the **Ru2Re**

and **RuRe2** supramolecular complexes even if the distance between the photosensitizer and catalyst subunits is longer than the shorter reported complex.

Table 5.6. *Photocatalytic properties of **Ru2Re** and **RuRe2** using BNAH.*[a]

	Product / μmol (TON)[b]			Φ_{CO}/%[c]	Γ_{CO}/%[b,d]	k_q[e]	η_q/%
	CO	HCOOH	H_2			$10^7\ M^{-1}s^{-1}$	
Ru2Re	17.5 (216 ± 5)	13 (77)	0.8 (10)	6.9± 0.9	56	2.0 ± 0.3	63
RuRe2	33.7 (225 ± 6)	8.6 (57)	0.2 (1)	8.3±1.2	79	2.2 ± 0.5	67

*[a]CO_2-saturated DMA-TEOA (5:1 v/v) solution containing **Ru2Re** (25 μM) or **RuRe2** (50 μM) and BNAH as sacrificial electron donor (0.1 M) was irradiated. [b]3-mL solution was irradiated for 20 h using a LED (530 nm, 4 mW) as a light source. TONs are calculated based on the photocatalyst used. [c]4-mL solution was irradiated at λ_{ex} = 480 nm (light intensity: 1 × 10^{-8} einstein s^{-1}). [d]The selectivity for CO production. [e]Quenching rate constants for emissions from the photosensitizer unit by a sacrificial electron donor obtained from linear Stern-Volmer plots and their lifetimes.*

Furthermore, the photocatalysis in the same experimental condition of 1:1 ratio of the free model species **$[Ru(dmb)_3]^{2+}$** and **$Re(dmb)(CO)_3Cl$** results in a TON for CO formation of 20 and for HCOOH formation of 120.[19] So, the trinuclear species **Ru2Re** and **RuRe2** present photocatalytic abilities much better than the ones of the systems reported in literature.

The quenching fractions of emissions from the photosensitizer unit by a sacrificial electron donor BNAH (0.1 M) were calculated as expressed by the following equation:

$$\eta = \frac{[sacrificial\ agent] \cdot k_q \cdot \tau_{em}}{1 + [sacrificial\ agent] \cdot k_q \cdot \tau_{em}} \qquad \text{eqn. 2}$$

Where τ_{em} is the emission lifetime of the excited state of the photosensitizer subunit when in solution there is not the sacrificial agent and k_q is the reductive quenching rate constant of the photosensitizer unit by the sacrificial electron donor.[20] The quenching fraction is a measure of the efficiency of the

photocatalysis since the reductive quenching is the first process of the photocatalytic reaction. In the cases of **Ru2Re** and **RuRe2** the quenching fractions are 63% and 67% respectively. The quantum yield for CO production (Φ_{CO}) was around 7% for **Ru2Re** and 8% for **RuRe2** using 480-nm light (light intensity: 1.0×10^{-8} einstein s^{-1}).

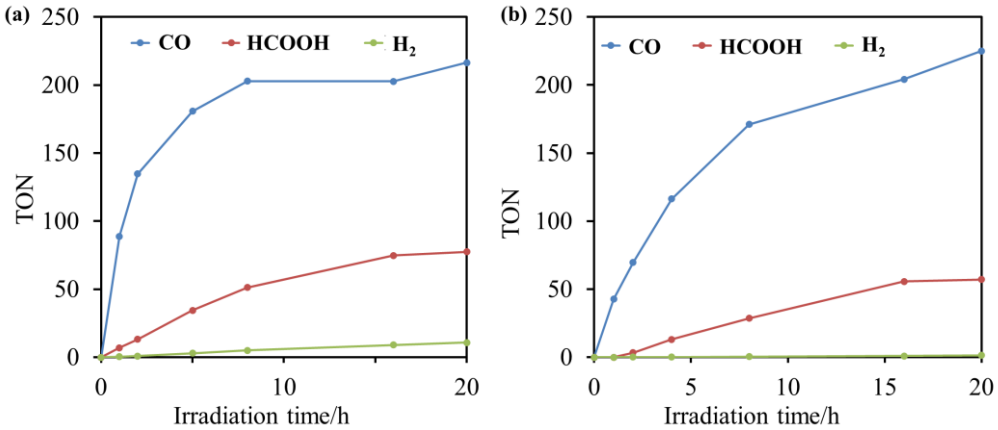

Figure 5.21. *Photocatalytic formation of CO (**blue** line), formic acid (**red** line) and H_2 (**green** line) as function of irradiation time using (a)**Ru2Re** (25 μM) and (b) **RuRe2** (50 μM) in CO_2-saturated DMA-TEOA (5:1 v/v, 3 mL) solutions and BNAH (0.1 M) irradiated using a LED (530 nm, 4 mW) as a light source.*

In order to increase the photocatalytic abilities, another electron donor was tested: the 1,3-dimethyl-2-phenyl-2,3-dihydro-1*H*-benzo[d]imidazole (BIH). This electron donor presents a reduction power ($E_{1/2}^{ox}$(BIH/BIH$^{\cdot+}$) = 0.33 V vs. SCE)[21] stronger than BNAH ($E^{\circ ox}$(BNAH/BNAH$^{\cdot+}$) = 0.57 V).[22] Moreover, BNAH works as one electron donor, otherwise BIH can act as two electron donors and the by-products of the BNAH oxidation affect the photocatalytic efficiency (see Chapter 4 for further details). The results obtained for the photocatalytic reaction using BIH as sacrificial electron donor are summarized in **Table 5.7**.

Also in this case, the photocatalysis analyses were performed in CO_2-satured atmosphere using a concentration of 50 μM of photosensitizer subunit to normalize the absorption properties of the complexes and compare their properties. In a typical run, a 3 mL CO_2-saturated mixed solution of *N*,*N*-

dimethylacetamide/triethanolamine (DMA/TEOA; 5:1 v/v) containing **RuRe2** (50 µM) or **Ru2Re** (25µ M) and BIH 0.1 M as a sacrificial electron donor was irradiated using a LED light source (530 nm, 4 mW). The selectivity for the CO formation increases (see **Figure 5.22**) and the quenching fractions, calculated with the equation 2, reach 99% in all cases.

Table 5.7. *Photocatalytic properties of **Ru2Re** and **RuRe2** using BIH.*[a]

	Product / µmol (TON)[b]			Φ_{CO} /%[c]	Γ_{CO}/%[b,d]	k_q[e]	η_q / %[f]
	CO	HCOOH	H_2			10^7 $M^{-1}s^{-1}$	
Ru2Re	186.5 (2486 ± 12)	20.2 (269)	0.009	28 ± 0.6	90	83 ± 0.8	99
Ru2Re[f]	90.6 (6038 ± 18)	21.7 (1447)	0.02	-	81	83 ± 0.8	99
RuRe2	277.4 (1850 ± 10)	3.3 (22)	~0	25 ± 0.5	99	80 ± 2.6	99
RuRe2[g]	157.0 (5232 ± 14)	5.3 (177)	~0	-	97	80 ± 2.6	99
RuRe[h]	110.0 (3657 ± 29)	1.1 (36)	0.03	30 ± 1.1	99	120(±0.5)	99

*[a]CO_2-saturated DMA-TEOA (5:1 v/v) solution containing **Ru2Re** (25 µM) or **RuRe2** (50 µM) and BIH as electron donor (0.1 M) was irradiated. [b]3-mL solution was irradiated for 20 h using a LED (530 nm, 4 mW) as a light source. TONs are calculated based on the photocatalyst used. [c]4-mL solution was irradiated at λ_{ex} = 480 nm (light intensity: 1 × 10^{-8} einstein s^{-1}). [d]The selectivity for CO production. [e]Quenching rate constants for emissions from the photosensitizer unit by a sacrificial electron donor obtained from linear Stern-Volmer plots and their lifetimes. [f][**Ru2Re**] = 5 µM, 60-h irradiation. [g][**RuRe2**] = 10 µM, 60-h irradiation. [h][**RuRe**] = 10 µM, 60-h irradiation.*

The quantum yield for CO production (Φ_{CO}) was around 25% for **Ru2Re** and 28% for **RuRe2** using 480-nm light (light intensity: 1.0 × 10^{-8} einstein s^{-1}).

Since CO is a two-electron reduced compound of CO_2 and BIH has been reported to function as a two-electron donor,[15] it is possible to calculate the consumption of BIH during the photocatalysis experiment in these experimental conditions. So, for TON_{CO} = 2486 the BIH consumed was 0.025 x 2486 = 62.2 mM, which is

62.2% of BIH added originally (100 mM) and for TON_{CO} = 1850 the BIH consumed was 0.05 x 1850 = 92.5 mM, which is 92.5% of BIH added originally (100 mM). This could be the reason for the slower CO formation after 16 hours of irradiation.

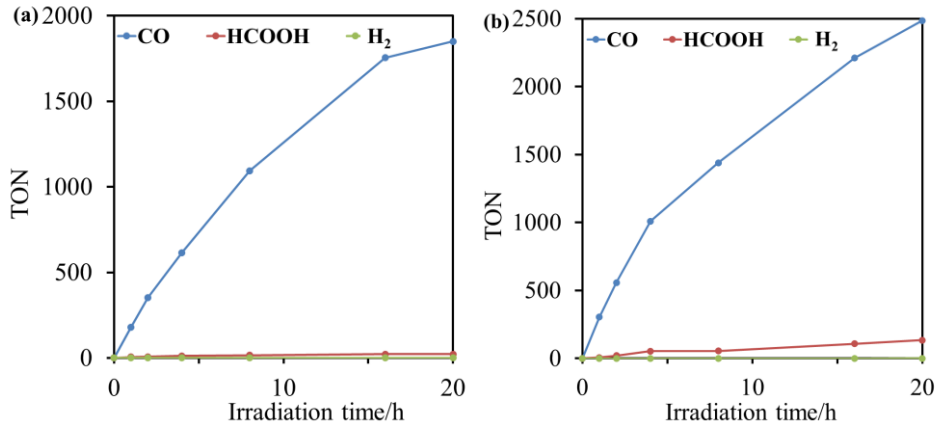

Figure 5.22. *Photocatalytic formation of CO (**blue** line), formic acid (**red** line) and H_2 (**green** line) as function of irradiation time using (a) **RuRe2** (50 µM) and (b) **Ru2Re** (25 µM) in CO_2-saturated DMA-TEOA (5:1 v/v, 3 mL) solutions and BIH (0.1 M) irradiated using a LED (530 nm, 4 mW) as a light source.*

In order to observe the durability of the supramolecular species the concentration of the supramolecular species **Ru2Re** and **RuRe2** was reduced to 1/5 (i.e. respectively 5 µM and 10 µM) and the samples have been irradiated until 60 hours. The results are summarized in **Table 5.7** and the time course for the photocatalytic experiments are shown in **Figure 5.23**. After 60 hours of irradiation the turnover number for the formation of CO reached 6038 for the supramolecular complex **Ru2Re** and 5232 for the complex **RuRe2**. These values are among the highest turnover numbers reported in literature. For comparison, in **Table 5.7,** are also reported the values obtained in the same conditions for the binuclear species **RuRe** (10 µM) where the photosensitizer and catalyst subunit are connected to an ethylene chain. In this case the TON_{CO} reaches 3657 (much lower than **Ru2Re** which presents the same number of Re unit).

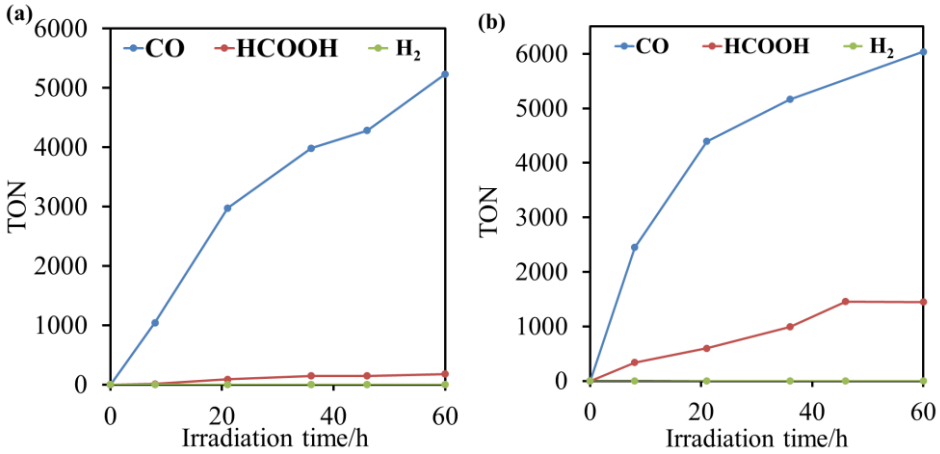

Figure 5.23. *Photocatalytic formation of CO (**blue** line), formic acid (**red** line) and H_2 (**green** line) as function of irradiation time using (a) **RuRe2** (10 µM) and (b) **Ru2Re** (5 µM) in CO_2-saturated DMA-TEOA (5:1 v/v, 3 mL) solutions and BIH (0.1 M) irradiated using a LED (530 nm, 4 mW) as a light source.*

To avoid the formation of by-products and increase the performance of the photocatalytic reaction, the photocatalytic abilities are studied starting directly with the **Re-CO_2TEOA** adduct, the intermediate usually formed as first step of the photocatalytic reaction. In order to obtain the trinuclear complexes **Ru2Re-CO_2TEOA** and **RuRe2-CO_2TEOA**, the complexes where the chloride ligand is substituted by a MeCN ligand were prepared starting from **RuRe2** and **Ru2Re** trinuclear complexes. The supramolecular complexes **RuRe2** and **Ru2Re** were left stirring in the dark for 8 days to obtain the **Re-MeCN** species. The complexes so formed were solubilized in DMA and left in the dark for 5 hours to obtain a Re-DMA compound. After, the same volume of TEOA was added to the solution and it was left overnight in the dark. The equilibrium between the Re-DMA and Re-TEOA was established. The mixture was adjusted in order to obtain a solution with a mixture 5:1 v/v of DMA/TEOA as solvent. After bubbling CO_2 in the solution, the **Re-CO_2-TEOA** adduct was formed. It is possible observing in **Figure 5.24** that the TON for the CO formation for the species **Ru2Re-CO_2TEOA** and **RuRe2-CO_2TEOA**, in the same experimental condition, increases in respect to **Ru2Re** and **RuRe2** of only 200 and 500 units respectively (i. e. 2695 for **Ru2Re** and 2368 for **RuRe2**).

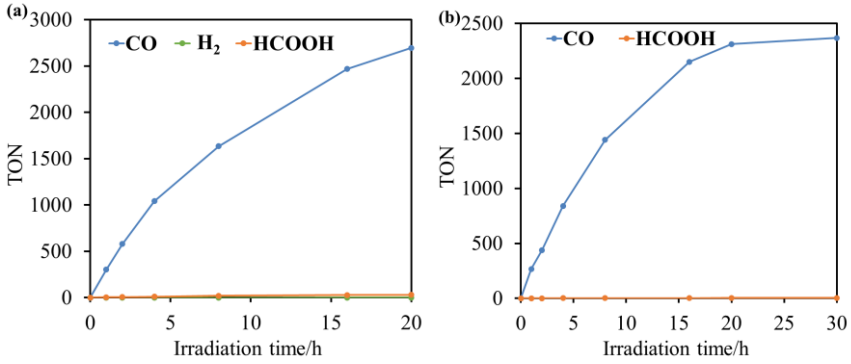

Figure 5.24. *Photocatalytic formation of CO (**blue** line), formic acid (**red** line) and H_2 (**green** line) as function of irradiation time using (a) **Ru2Re-CO₂TEOA** (25 µM) and (b) **RuRe2-CO₂TEOA** (50 µM) in CO_2-saturated DMA-TEOA (5:1 v/v, 3 mL) solutions and BIH (0.1 M) irradiated using a LED (530 nm, 4 mW) as a light source.*

Also the selectivity increases reaching the 99.9% for **RuRe2-CO₂TEOA** and 99% for **Ru2Re-CO₂TEOA**. In the cases of **RuRe2-CO₂TEOA** the time course for the CO formation reaches a plateau because the whole BIH presents in solution has been consumed.

5.2.3 Synthesis of Ru2Ru Supramolecular Complex

The synthesis of the supramolecular species **Ru2Ru** are represented in **Scheme 5.5**.

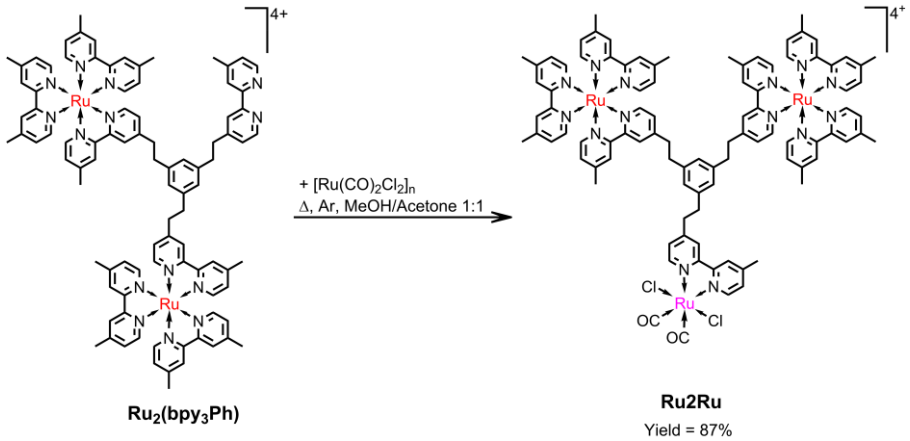

Scheme 5.5.

This complex was synthesized by reacting the ligand complex **Ru₂(bpy₃Ph)** with

a polymeric precursor **$[Ru(CO)_2Cl_2]_n$** (synthesized as reported in literature by reacting $RuCl_3 \cdot xH_2O$ with parformaldeide)[23] under argon atmosphere at reflux using as solvent a mixture MeOH/acetone (1:1 v/v).

The reaction was monitored by UV-Vis spectroscopy following the formation of a new small absorption band at 310 nm. The final complex was obtained after reprecipitation in diethyl ether as orange solid with a yield of 87%.

5.2.3.1 Absorption Spectra and Photophysical Properties

The absorption spectra of the species **$Ru_2(bpy_3Ph)$** and **Ru_2Ru** recorded in acetonitrile are shown in **Figure 5.25** and all the photophysical properties are summarized in **Table 5.8**.

Table 5.8. *Photophysical properties measured in deaerated MeCN[(a)]*

	Absorption	Luminescence		
	λ_{max} /nm (ε_{460}/$M^{-1}cm^{-1}$)[(b)]	λ_{max} / nm	τ / ns [(c)]	Φ_{em} [(c)]
$Ru_2(bpy_3Ph)$	460 (31180)	625	851 (115)	0.086 (0.013)
Ru_2Ru	460 (31550)	624	867 (117)	0.085 (0.013)
$[Ru(dmb)_3]^{2+}$[(d)]	458 (16300)	622	875	0.089[(e)]
$Ru(dmb)(CO)_2Cl_2$[(e)]	349 (1300)	n.d.[(f)]	n.d.[(f)]	n.d.[(f)]

(a) All data are measured in MeCN at 293 K. (b) Only the low energy maximum is reported. (c) Data in parenthesis refer to air-equilibrated solution. (d) From reference 7. (e) From reference 24. (f) From reference 25.

It is possible to notice in **Table 5.8** that the extinction coefficient of the model species **$Ru(dmb)(CO)_2Cl_2$** is very low if compared with the ones of the precursor metal complex **$Ru_2(bpy_3Ph)$**. As consequence, the absorption spectrum of the **Ru2Ru** species is very close to the one of the species **$Ru_2(bpy_3Ph)$** except for a small contribution around 310 nm (see **Figure 5.25**).

The complex **Ru2Ru** is luminescent in acetonitrile fluid solution at room temperature (see **Figure 5.26** and **Table 5.8**).

For the trinuclear species **Ru2Ru** the emission is due to the radiative deactivation

of the ^{3}MLCT state which involves the Ru(II)-photosensitizers centers and the polypyridine ligands. The emission of the **Ru2Ru** species can be overlapped with the one of the precursor species **$Ru_2(bpy_3Ph)$**, regardless of the excitation wavelength (see **Figure 5.26**).

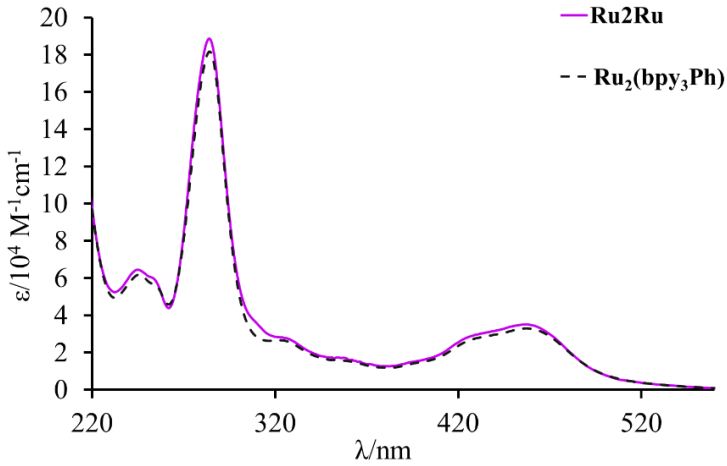

Figure 5.25. *Absorption spectra of **$Ru_2(bpy_3Ph)$** (**black** dashed line) and **Ru2Re** (**violet** solid line) in acetonitrile at room temperature.*

The emission quantum yield and lifetime of the species **Ru2Ru** are independent of the presence of the Ruthenium catalyst subunit.

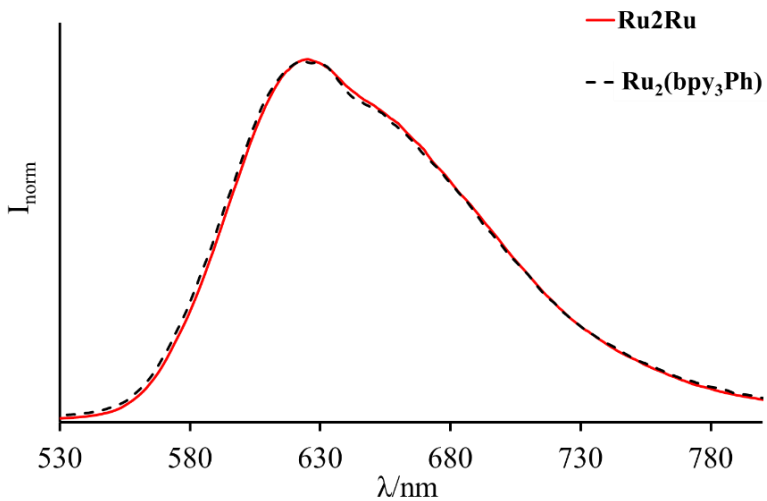

Figure 5.26. *Emission spectra of **$Ru_2(bpy_3Ph)$** (**black** dashed line) and **Ru2Ru** (**red** solid line) in acetonitrile at room temperature at λ_{exc} = 450 nm.*

All these results give the possibility to affirm that there are no strong electronic interactions between the excited photosensitizer Ru(II) subunit and the catalysts Ru(II) subunit.

5.2.3.2 Redox Properties

The redox properties of the final trinuclear complexes **Ru2Ru** have been investigated by voltametric analysis, such as cyclic, differential pulsed and square wave voltammetry. The results are summarized in **Table 5.9**. In the **Ru2Ru** voltammograms it is possible observing a reversible oxidation process due to the oxidation process of the Ru(II)-photosensitizers and three different reduction processes which involve the reduction of the three different bipyridine moieties (see **Figure 5.27**).

In the voltammogram of the final product **Ru2Ru** it is possible observing that the first reduction peak at about -1.41 V is a little bit broader and bigger than the oxidation peak for the reduction of the two bipyridines coordinated to the Ru(II) photosensitizer centers and the irreversible oxidation of the bipyridine unit coordinated to the Ru(II) catalyst center.

Table 5.9. *Redox properties*

	$E_{1/2}$, V vs SCE[(a)]			
	E_{Ox1}	**E_{Red1}**	**E_{Red2}**	**E_{Red3}**
$Ru_2(bpy_3Ph)$	+1.15 [2]	-1.43 [2]	-1.61[2]	-1.89[2]
Ru2Ru	+1.14 [2]	-1.41[br]	-1.58[2]	-1.89[2]
$[Ru(dmb)_3]^{2+}$[(b)]	+1.10 [1]	-1.45[1]		
$[Ru(dmb)(CO)_2Cl_2]$[(c)]	+ 1.60	-1.40		

(a) Electrochemical Properties measured at room temperature in MeCN containing 0.1 M TBAH. All values are obtained using the redox couple ferrocene/ferrocenium (395 mV vs. SCE in acetonitrile) as internal reference. The numbers in parentheses refer to the number of exchanges electrons. Irr indicates an irreversible process: in this case, the E values reported in table refer to peak potentials in pulse voltammetry experiments. (b) From reference 11. (c) From reference 26.

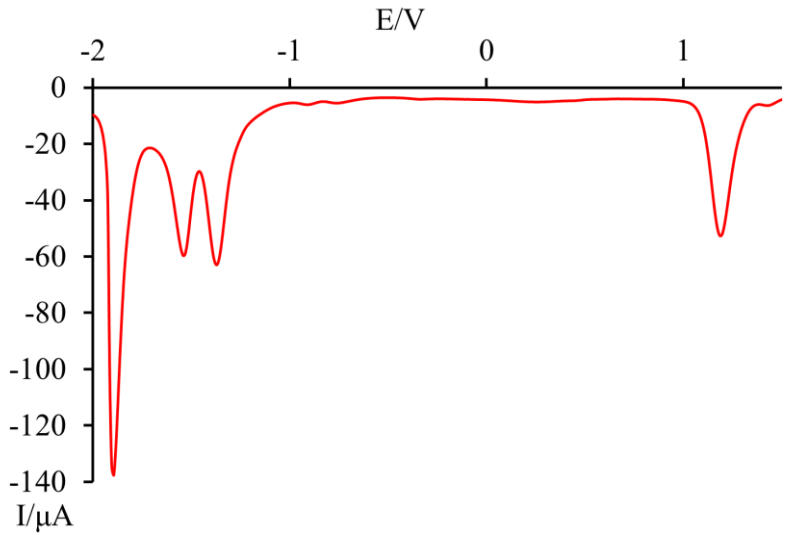

Figure 5.27. *DPV of **Ru2Ru** (0.5 mM) in argon purged MeCN at room temperature using Bu_4NPF_6 (0.05 M) as supporting electrolyte. As internal reference was used the redox couple ferrocene/ferrocenium (395 mV vs. SCE in acetonitrile). Scan rate 20 mV/s.*

5.2.3.3 Photocatalytic Analysis

Preliminary studies on the photocatalytic abilities of the trinuclear **Ru2Ru** supramolecular complex have been also carried out. The photocatalysis analysis were performed in CO_2-satured atmosphere using a concentration of 50 μM of photosensitizer subunit to normalize the absorption properties of the complexes. In a typical run, a 3 mL CO_2-saturated mixed solution of *N*,*N*-dimethylacetamide-triethanolamine (DMA-TEOA; 5:1 v/v) containing **Ru2Ru** (25 μM) and 1-benzyl-1,4-dihydronicotinamide (BNAH; 0.1 M) as sacrificial electron donor was irradiated using a LED light source (530 nm, 4 mW), giving HCOOH with good selectivity. The DMA (N,N-Dimethylacetamide) was recently employed as solvent in the CO_2 reduction because it does not produce formate thanks to its high stability against the hydrolysis.[13] The TEOA assists the capture of CO_2 from the Ru(II) catalyst subunit[14] and captures the proton generated from the oxidation process of the sacrificial agent[12] by enhancing the photocatalytic abilities. The products of photocatalysis are analysed by Gas Chromatography (for the

quantitative analysis of CO and H_2) and Capillary Electrophoresis (for the quantification of HCOOH formation). The results are shown in **Figure 5.28**.

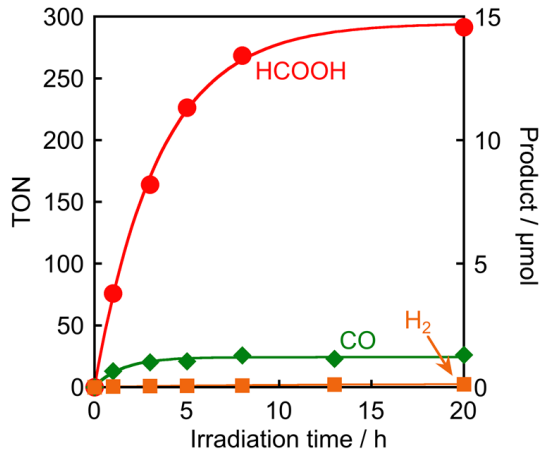

Figure 5.28. *Photocatalytic formation of CO (**blue** line) and H_2 (**green** line) as function of irradiation time using **Ru2Ru** (25 µM) CO_2-saturated DMA-TEOA (5:1 v/v, 3 mL) solutions and BIH (0.1 M) irradiated using a LED (530 nm, 4 mW) as a light source.*

The TON is quite good but further analysis on this complex are still running.

5.3 Ligand bpy$_4$Ph and its metal complexes

5.3.1 Synthesis of ligand bpy$_4$Ph

The synthesis of **bpy$_4$Ph** ligand is reported in **Scheme 5.6**. The synthesis has been performed at low temperature (-33°C) under inert atmosphere in anhydrous condition in one step using 4,4'-dimethyl-2,2'-bipiridine (hereafter dmb) and 1,2,4,5-tetrakis(bromomethyl)benzene in presence of lithium diisopropylamide (LDA).[1] The LDA was added in slight excess slowly dropwise to a THF solution of dmb at -33°C. LDA is a strong base suitable to remove a hydrogen from one methyl substituent on the bipyridine. Later, a THF solution of 1,2,4,5-tetrakis(bromomethyl)benzene was added. The resulting reaction mixture gradually reaches room temperature and is left stirring overnight. The colour of solution changes from dark brown to pale yellow. The reaction was quenched with

water. The presence of two equivalent methyl groups on the bipyridine and the reaction condition lead to the formation of a mixture of products. The crude was purified by chromatography column on silica gel using DCM/MeOH (9:1 v/v) as eluent. The first fraction eluted was the unreacted bipyridine.

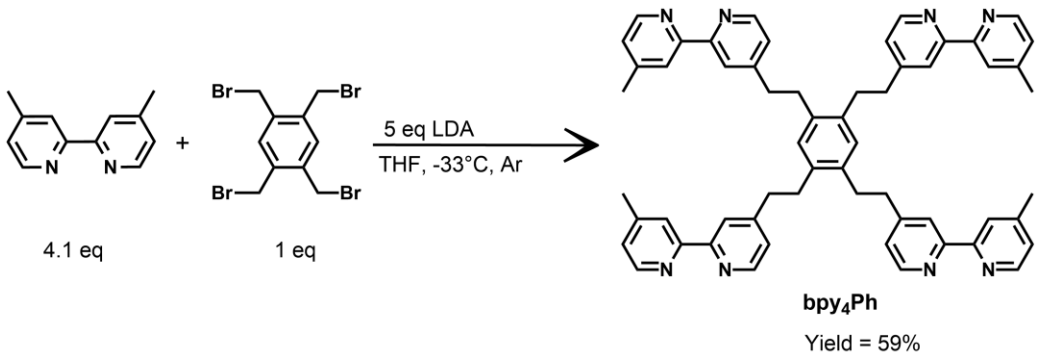

Scheme 5.6.

The required product was eluted as second fraction and recrystallized from ethanol leading to the final product with moderate yield (59%). The characterization was performed by ^{1}H and ^{13}C NMR spectroscopy in CD_2Cl. The absence of the signal of the aliphatic protons of 1,2,4,5-tetrakis(bromomethyl)benzene and the new peak of the sixteen protons of the ethylene chains at $\delta = 2.82$ ppm are the clear indication for the formation of the required product. This ligand results to be suitable to obtain different tetranuclear complexes that integrate three Ru(II)-based photosensitizer subunits and a catalyst subunit.

5.3.2 Synthesis of Ru3Re Supramolecular Complex

The synthesis of the supramolecular species **Ru3Re** is shown in **Scheme 5.7**.

The synthesis was performed with the "cal/cam" approach employed also for all the previously reported supramolecular complexes. In order to obtain complexes with three photosensitizer subunits, the ligand **bpy$_4$Ph** was put to react in 1:3

molar ratio with the metal-complex **Ru(dmb)$_2$Cl$_2$** in a EtOH/MeOH 1:1 v/v mixture at reflux under argon atmosphere (**Scheme 5.7**).

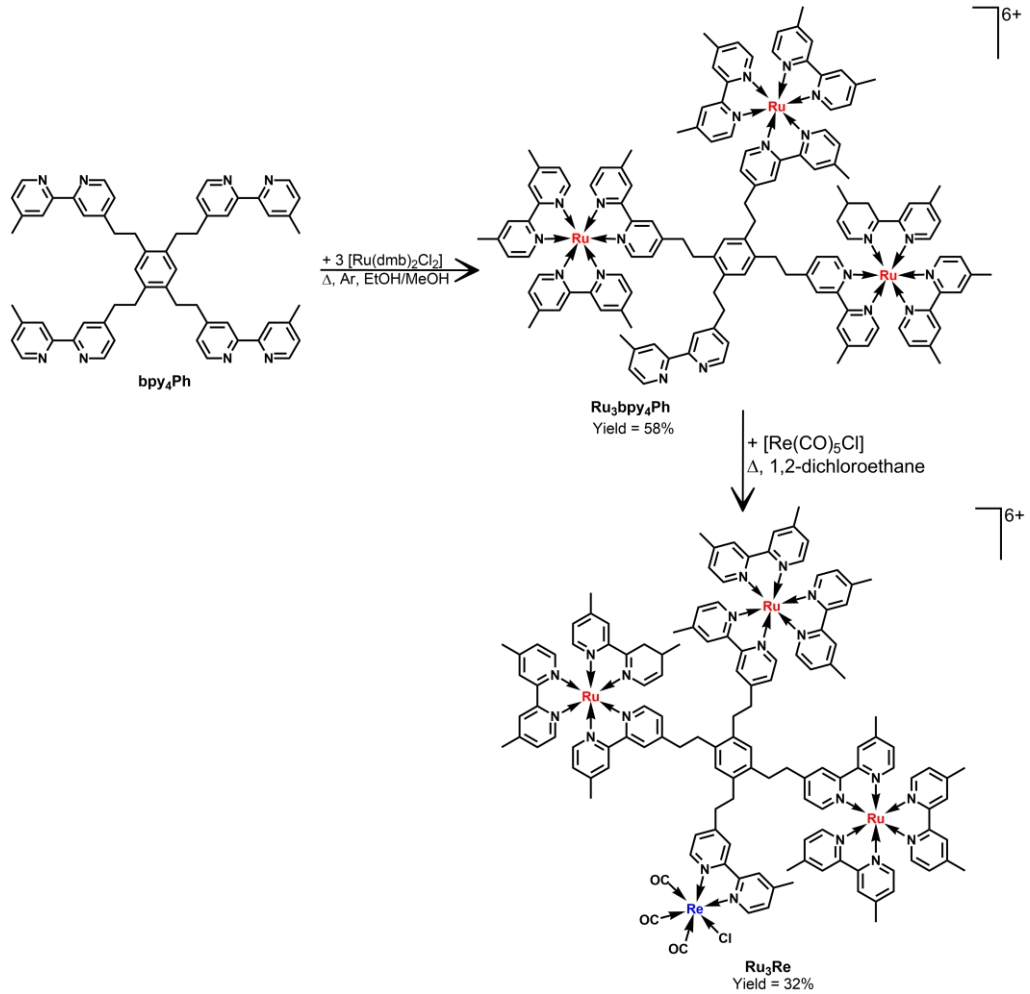

Scheme 5.7.

The presence of four equivalent bipyridine units in the ligand **bpy$_4$Ph** lead to the competitive formation of a mixture of four different supramolecular complexes **Ru(bpy$_4$Ph)**, **Ru$_2$(bpy$_4$Ph)**, **Ru$_3$(bpy$_4$Ph)** and **Ru$_4$(bpy$_4$Ph)** charged respectively +2, +4, +6 and +8. The mixture was separated by ionic exchange chromatography taking advantage of the different charge of the metal complexes using CM Sephadex C-25, an ionic exchange resin, as stationary phases and a solution of NaCl in H_2O/acetone (5:3 v/v). Changing the ionic force of the medium, by a

progressive increasing of the concentration of NaCl in solution, leads to the selective elution of the four different complexes from the lest to the most charged one. The required **$Ru_3(bpy_4Ph)$** complex was eluted in the third fraction and isolated as orange solid as PF_6^- salt with a yield of 56%. The presence in **$Ru_3(bpy_4Ph)$** of one free dmb moiety gives the possibility to use this complex to react with suitable precursor to obtain the supramolecular complexes whit also a catalyst subunit. Consequently, the second synthetic step was the reaction of the ligand-complex **$Ru_3(bpy_4Ph)$** with the **$Re(CO)_5Cl$** in 1,2-dichloroethane at reflux under inert atmosphere (**Scheme 5.7**). The reaction was controlled using the UV-Vis absorption spectroscopy following the presence of the new **$Re(dmb)(CO)_3Cl$** ^{1}MLCT absorption band at 360 nm. The product was purified by precipitation adding NH_4PF_6 and it was washed with diethylether to remove the unreacted rhenium precursor. The final **Ru3Re** product was obtained with a yield of 32%.

5.3.2.1 Absorption Spectra and Photophysical Properties

The absorption spectra of the species **$Ru_3(bpy_4Ph)$** and **RuRe** recorded in acetonitrile are shown in **Figure 5.29** and all the photophysical properties are summarized in **Table 5.10**. The absorption spectrum of the precursor complex **$Ru_3(bpy_4Ph)$** is characterized by a strong absorption band between 450 and 465 nm assigned to spin-allowed transition ^{1}MLCT (metal to ligand charge transfer) which involves a charge transfer from orbital mainly centred on the Ru(II) to an orbital mainly centred on the polypyridine ligands. The molar extinction coefficient of the supramolecular complex is about three times the one of the model species **$[Ru(dmb)_3]^{2+}$**, as expected, (due to the presence of three metal center). In the UV-Vis region it is possible to observe an intense absorption band, at around 285 nm, due to the π-π* transition centred on the orbitals of the ligands.

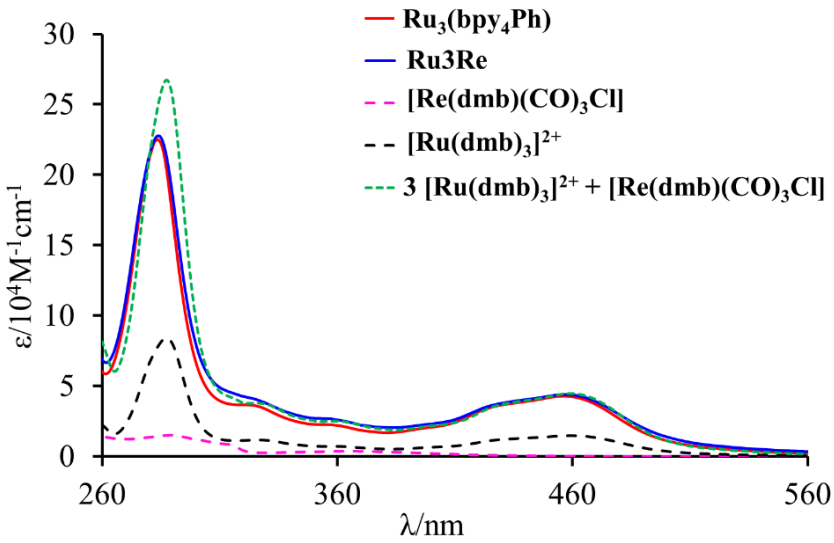

Figure 5.29. *Absorption spectra of the model species* ***[Ru(dmb)$_3$]$^{2+}$*** *(**black** dashed line),* ***Re(dmb)CO$_3$Cl*** *(**pink** dashed line) and their weighted sum (**green** dotted line) superimposed with the spectra of the species trinuclear* ***Ru2Re*** *(**blue** solid line) and of the precursor* ***Ru$_3$(bpy$_4$Ph)*** *(**red** solid line).*

The absorption spectrum of the species **Ru3Re** (shown in **Figure 5.29**) presents the same contributions of the precursor species and an additional contribution between 280 and 410 nm due to the ^{1}MLCT transition involving the Re(I) center.

Table 5.10. *Photophysical properties measured in deaerated MeCN*[(a)]

	Absorption	Luminescence		
	λ_{max} /nm (ε_{460}/M^{-1}cm^{-1})[(b)]	λ_{max} / nm	τ / ns [(c)]	Φ_{em} [(c)]
Ru$_3$(bpy$_4$Ph)	460 (41000)	625	851 (115)	0.086 (0.014)
Ru3Re	460 (42500)	629	852 (117)	0.086 (0.013)
[Ru(dmb)$_3$]$^{2+}$[(d)]	458 (16300)	622	875	0.089[(e)]
Re(dmb)CO$_3$Cl	364 (3630) [(f)]	600[(g)]	49[(g)]	0.0057[(h)]

(a) All data are measured in MeCN at 293 K. (b) Only the low energy maximum is reported. (c) Data in parenthesis refer to air-equilibrated solution. (d) From reference 7. (e) From reference 8. (f) From reference 9. (g) From reference 10. (h) In MeTHF.

The weighed sum spectrum of the model species **[Ru(dmb)$_3$]$^{2+}$** and **Re(dmb)(CO)$_3$Cl** can be superimposed to the ones of the supramolecular species

Ru3Re. This suggests that there are no strong electronic interactions between the Ru(II) and Re(I) metal centers in the ground state. Consequently, the photophysical properties of each metal center are independent and additive. All metal complexes are luminescent in acetonitrile fluid solution at room temperature (see **Figure 5.30** and **Table 5.10**).

For the trinuclear species **$Ru_3(bpy_4Ph)$**, the emission is due to the radiative deactivation of the ^{3}MLCT state which involves the Ru(II) centers and the polypyridine ligands.

The emission recorded for the trinuclear species **Ru3Re** can be overlapped with the one of the precursor **$Ru_3(bpy_4Ph)$**, regardless of the excitation wavelength (see **Figure 5.30**) and also by exciting the sample in the spectral range where the Re(I) absorption contribute is bigger.

The emission quantum yield and lifetime of the species **Ru3Re** are independent of the presence of the rhenium subunit.

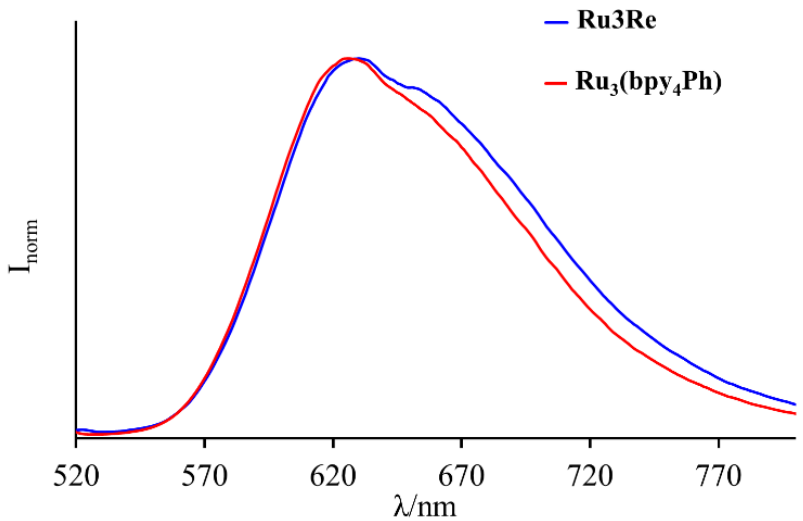

Figure 5.30. Normalized *emission spectra of* ***$Ru_3(bpy_4Ph)$*** *(**red** solid line) and* ***RuRe2*** *(**Blue** solid line) in acetonitrile at room temperature at λ_{exc} = 450 nm.*

All these results give the possibility to affirm that there are no strong electronic interactions between the excited photosensitizers Ru(II) subunits and the catalyst Re(I) subunit.

5.3.2.2 Redox Properties

The redox properties of precursor trinuclear metal complex **$Ru_3(bpy_4Ph)$** and final tetranuclear metal complex **Ru3Re** have been investigated by cyclic, differential pulsed and square wave voltammetry. The results are summarized in **Table 5.11**.

In the voltammograms of the **$Ru_3(bpy_4Ph)$** species it is possible observing a reversible oxidation process due to the oxidation process of the Ru(II) and three different reduction processes which involve the reduction of the three different bipyridine moieties coordinated to the Ru(II) metal centers (see **Figure 5.31**).

In the **Ru3Re** voltammogram a further irreversible oxidation process, due to the oxidation of the Re(I) metal center, is present. In reduction it is possible observing three different reduction processes.

Table 5.11. *Redox properties*

	$E_{1/2}$, V vs SCE[(a)]				
	E_{Ox2}	**E_{Ox1}**	**E_{Red1}**	**E_{Red2}**	**E_{Red3}**
$Ru_3(bpy_4Ph)$		+1.14 [3]	-1.40 [3]	-1.61[3]	
Ru3Re	+1.42 irr	+1.15 [2]	-1.41[3]	-1.59	-1.90
$[Ru(dmb)_3]^{2+}$[(b)]		+1.10 [1]	-1.45[1]		
$[Re(dmb)(CO)_3Cl]$[(c)]		+1.36 irr	-1.43 [1]		

(a) Electrochemical properties measured at room temperature in MeCN containing 0.1 M TBAH. All values are obtained using the redox couple ferrocene/ferrocenium (395 mV vs. SCE in acetonitrile) as internal reference. The numbers in parentheses refer to the number of exchanges electrons. Irr indicates an irreversible process: in this case, the E values reported in table refer to peak potentials in pulse voltammetry experiments. (b) From reference 11. (c) From reference 10.

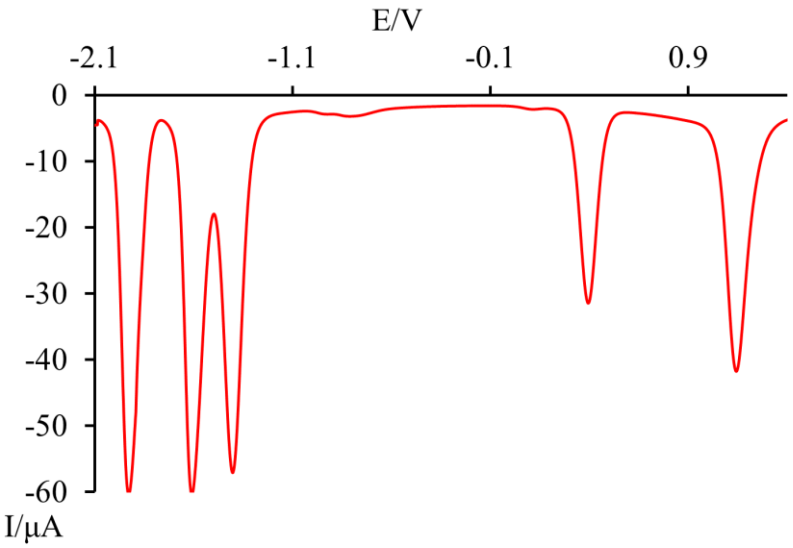

Figure 5.31. *DPV of $Ru_3(bpy_4Ph)$ (0.5 mM) in argon purged MeCN at room temperature using Bu_4NPF_6 (0.05 M) as supporting electrolyte. As internal reference was used the redox couple ferrocene/ferrocenium (395 mV vs. SCE in acetonitrile). Scan rate 200 mV/s.*

The first reduction processes involve the reduction of the three different bipyridine moieties coordinated to the Ru(II) metal centers and the dmb subunit coordinated to the Re(I) metal center.

5.3.2.3 Photocatalysis Analysis

The photocatalytic abilities of the tetranuclear **Ru3Re** supramolecular complex are also investigated. The photocatalysis analysis are performed in CO_2-satured atmosphere using a concentration of 50 μM of photosensitizer subunit to normalize the absorption properties of the complexes. In a typical run, a 3 mL CO_2-saturated mixed solution of *N*,*N*-dimethylacetamide/triethanolamine (DMA/TEOA; 5:1 v/v) containing **Ru3Re** (16 μM) and 1,3-dimethyl-2-phenyl-2,3-dihydro-1*H*-benzo[d]imidazole (BIH) as sacrificial electron donor was irradiated using a LED light source (530 nm, 4 mW), giving CO almost selectively. The DMA (N,N-Dimethylacetamide) was recently employed as solvent in the CO_2 reduction because it does not produce formate thanks to its high stability against the hydrolysis.[13] The TEOA assists the capture of CO_2 from

the Re(I) catalyst subunit[14] and captures the proton generated from the oxidation process of the sacrificial agent[12] by enhancing the photocatalytic abilities. The products of photocatalysis are analysed by Gas Chromatography (for the quantitative analysis of CO and H_2) and Capillary Electrophoresis (for the quantification of HCOOH formation). The results are shown in **Figure 5.32**.

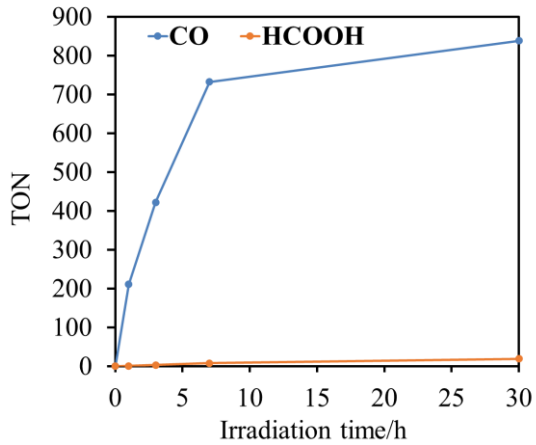

Figure 5.32. *Photocatalytic formation of CO (**blue** line) and HCOOH (**orange** line) as function of irradiation time using **Ru2Re** (50 µM) CO_2-saturated DMA-TEOA (5:1 v/v, 3 mL) solutions and BIH (0.1 M) irradiated using a LED (530 nm, 4 mW) as a light source.*

The TON_{CO} reaches 838 in 30 hours and the selectivity for the CO formation is 97.8%. This one is the worse supramolecular complex studied. Experiment to understand the reason of this bad catalytic performance are still in progress.

5.3.3. Synthesis of Ru3Ru Supramolecular Complex

The synthesis of the supramolecular species **Ru3Ru** are represented in **Scheme 5.8**. This complex was synthesized by reacting the ligand complex **Ru_3(bpy$_4$Ph)** with a polymeric precursor **$[Ru(CO)_2Cl_2]_n$** (synthesized as reported in literature by reacting $RuCl_3 \cdot xH_2O$ with parformaldeide)[23] under argon atmosphere at reflux using as solvent a mixture MeOH/acetone (1:1 v/v). The reaction was monitored by UV-Vis spectroscopy following the formation of a new

small absorption band at 310 nm. The product was isolated as PF_6^- salt with a yield of 78%.

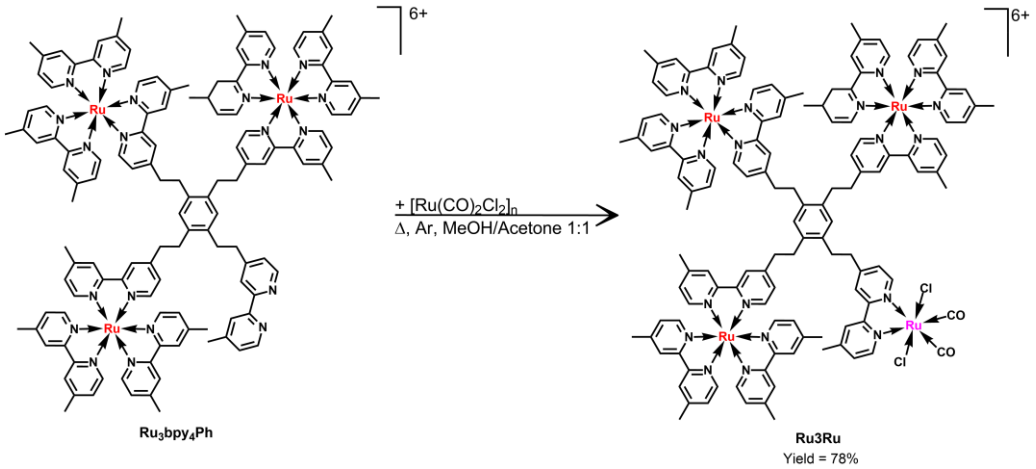

Scheme 5.8.

5.3.3.1 Absorption Spectra and Photophysical properties

The absorption spectra of the species **$Ru_3(bpy_4Ph)$** and **Ru_3Ru** recorded in acetonitrile are shown in **Figure 5.33** and all the photophysical properties are summarized in **Table 5.12**.

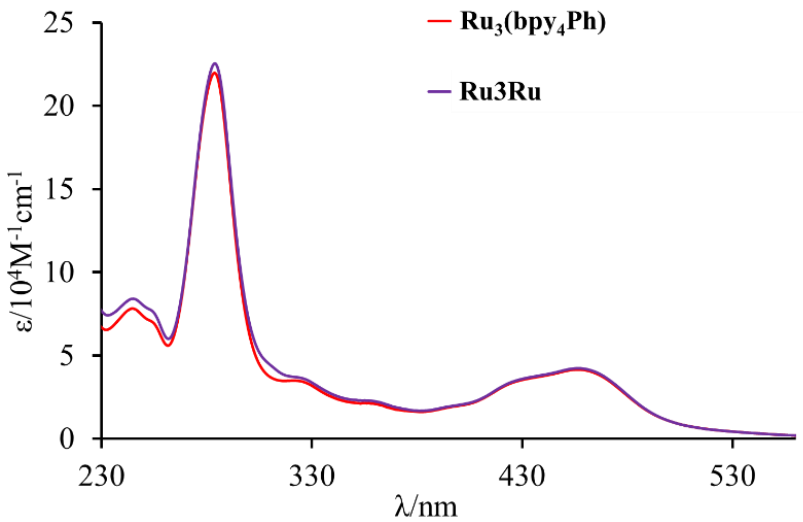

Figure 5.33. *Absorption spectra of **$Ru_3(bpy_4Ph)$** (**red** solid line) and **Ru3Ru** (**violet** solid line) in acetonitrile at room temperature.*

It is possible to note in **Table 5.12** that the extinction coefficient of the model species **Ru(dmb)(CO)$_2$Cl$_2$** is very low if compared to the ones of the precursor metal complex **Ru$_3$(bpy$_4$Ph)**. As consequence, the absorption spectrum of the **Ru3Ru** species is very close to the one of the species **Ru$_3$(bpy$_4$Ph)** except for a small contribution around 310 nm (see **Figure 5.33**).

Table 5.12. *Photophysical properties measured in deaerated MeCN*[(a)]

	Absorption	Luminescence		
	λ_{max} /nm (ε_{460}/M^{-1}cm^{-1})[(b)]	λ_{max} / nm	τ / ns [(c)]	Φ_{em} [(c)]
Ru$_3$(bpy$_4$Ph)	460 (41000)	625	851 (115)	0.086 (0.014)
Ru3Ru	460 (41500)	624	867 (117)	0.085 (0.013)
[Ru(dmb)$_3$]$^{2+}$[(d)]	458 (16300)	622	875	0.089[(e)]
Ru(dmb)(CO)$_2$Cl$_2$[(e)]	349 (1300)	n.d.[(f)]	n.d.[(f)]	n.d.[(f)]

(a) All data are measured in MeCN at 293 K. (b) Only the low energy maximum is reported. (c) Data in parenthesis refer to air-equilibrated solution. (d) From reference 7. (e) From reference 24. (f) From reference 25.

The complex **Ru3Ru** is luminescent in acetonitrile fluid solution at room temperature (see **Figure 5.34** and **Table 5.12**).

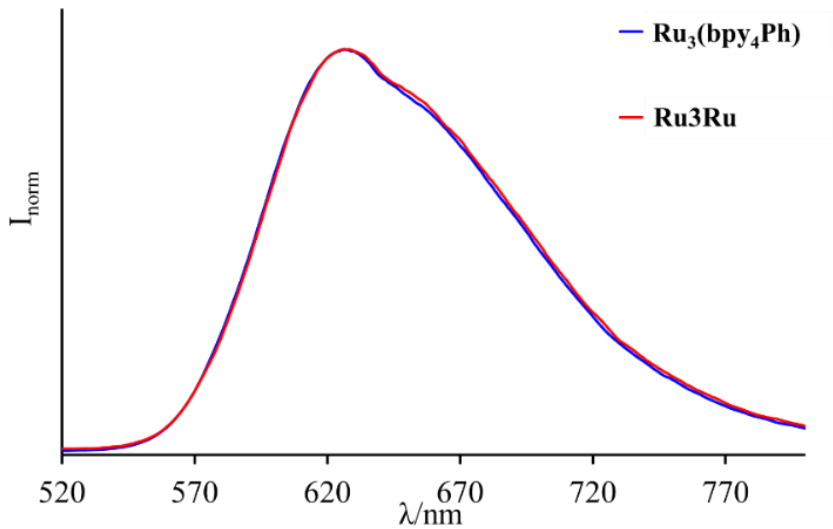

Figure 5.34. *Emission spectra of **Ru$_3$(bpy$_4$Ph)** (**blue** solid line) and **Ru3Ru** (**red** solid line) in acetonitrile at room temperature at λ_{exc} = 450 nm.*

For the trinuclear species **Ru3Ru** the emission is due to the radiative deactivation of the ^{3}MLCT state which involves the Ru(II)-photosensitizers centers and the polypyridine ligands. The emission of the **Ru3Ru** species can be overlapped with the one of the precursor species **Ru_2(bpy$_3$Ph)**, regardless of the excitation wavelength (see **Figure 5.34**).

The emission quantum yield and lifetime of the species **Ru3Ru** are independent of the presence of the Ruthenium catalyst subunit. All these results give the possibility to affirm that there are no strong electronic interactions between the excited photosensitizers Ru(II) subunits and the catalyst Ru(II) subunit.

5.3.3.2 Redox Properties

The redox properties of the final trinuclear complex **Ru3Ru** has been investigated by voltametric analysis, such as cyclic, differential pulsed and square wave voltammetry. The results are summarized in **Table 5.13**.

In the **Ru3Ru** voltammograms (see **Figure 5.35**) it is possible observing a reversible oxidation process due to the oxidation process of the Ru(II) and three different reduction processes which involve the reduction of the three different bipyridine moieties.

Table 5.13. *Redox properties*

	$E_{1/2}$, V vs SCE[(a)]		
	E_{Ox1}	**E_{Red1}**	**E_{Red2}**
Ru_3(bpy$_4$Ph)	+1.14 [3]	-1.40 [3]	-1.61[3]
Ru3Ru	+1.14 [3]	-1.41[br]	-1.58
[Ru(dmb)$_3$]$^{2+}$[(b)]	+1.10 [1]	-1.45[1]	
[Ru(dmb)(CO)$_2$Cl$_2$][(c)]	+ 1.60	-1.40	

(a) Electrochemical properties measured at room temperature in MeCN containing 0.1 M TBAH. All values are obtained using the redox couple ferrocene/ferrocenium (395 mV vs. SCE in acetonitrile) as internal reference. The numbers in parentheses refer to the number of exchanges electrons, when this data is available. Irr indicates an irreversible process: in this case, the E values reported in table refer to peak potentials in pulse voltammetry experiments. (b) From reference 11. (c) From reference 26.

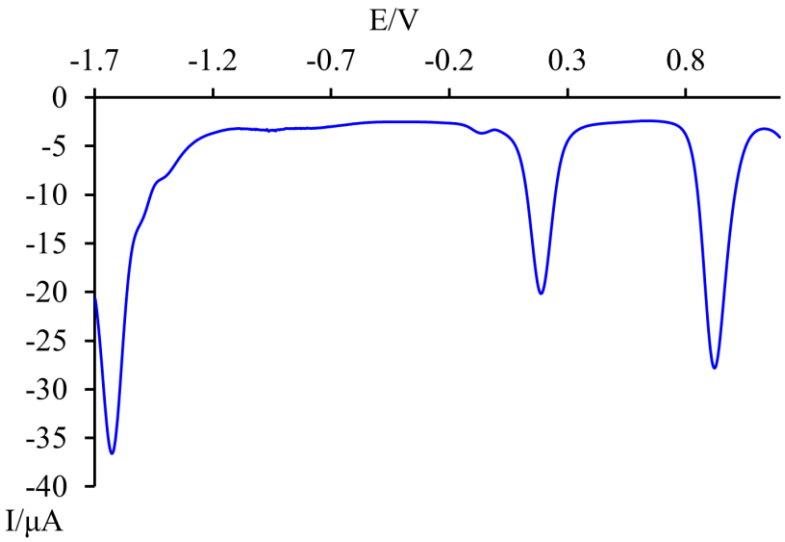

Figure 5.35. *DPV of **Ru3Ru** (0.5 mM) in argon purged MeCN at room temperature using Bu_4NPF_6 (0.05 M) as supporting electrolyte. As internal reference was used the redox couple ferrocene/ferrocenium (395 mV vs. SCE in acetonitrile). Scan rate 20 mV/s.*

In the voltammogram of the final product **Ru3Ru** (show in **Figure 5.35**) it is possible observing that the first reduction peak at about -1.41 V is a little bit broader and bigger than the oxidation peak for the reduction of the three bipyridines coordinated to the Ru(II) photosensitizer centers and the irreversible oxidation of the bipyridine unit coordinated to the Ru(II) catalyst center.

5.3.3.3 Photocatalytic Analysis

Preliminary studies on the photocatalytic abilities of the trinuclear **Ru3Ru** supramolecular complex are also carried out. The photocatalysis analyses are performed in CO_2-satured atmosphere using a concentration of 50 μM of photosensitizer subunit to normalize the absorption properties of the complexes. In a typical run, a 3 mL CO_2-saturated mixed solution of *N*,*N*-dimethylacetamide/triethanolamine (DMA/TEOA; 5:1 v/v) containing **Ru3Ru** (16.7 μM) and 1-benzyl-1,4-dihydronicotinamide (BNAH; 0.1 M) as sacrificial electron donor, was irradiated using a LED light source (530 nm, 4 mW), giving HCOOH with good selectivity. The DMA (N,N-

Dimethylacetamide) was recently employed as solvent in the CO_2 reduction because it does not produce formate thanks to its high stability against the hydrolysis.[13]

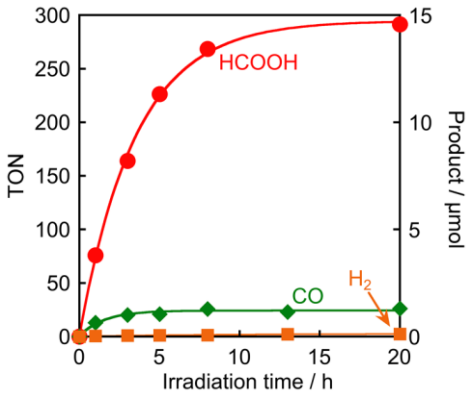

Figure 5.36. *Photocatalytic formation of CO (**blue** line) and H_2 (**green** line) as function of irradiation time using **Ru2Ru** (25 µM) CO_2-saturated DMA-TEOA (5:1 v/v, 3 mL) solutions and BIH (0.1 M) irradiated using a LED (530 nm, 4 mW) as a light source.*

The TEOA assists the capture of CO_2 from the Re(I) catalyst subunit[14] and captures the proton generated from the oxidation process of the sacrificial agent[12] by enhancing the photocatalytic abilities.

The products of photocatalysis are analysed by Gas Chromatography (for the quantitative analysis of CO and H_2) and Capillary Electrophoresis (for the quantification of HCOOH formation). The results are shown in **Figure 5.36**.

The TON is quite good. Unfortunately, the impact of the pandemic emergency delayed the study, so further analyses on this complex are still running.

5.4 Second generation: dendritic mixed metal photocatalysts

5.4.1 Synthesis of RuRe3 and RuRe6 Supramolecular Complexes

As a consequence of the better photocatalytic performance obtained for the **RuRe2** metal complex in respect to the supramolecular complex **Ru2Re,** it

has been decided to improve the number of catalytic subunits compared to the photosensitizer subunit.

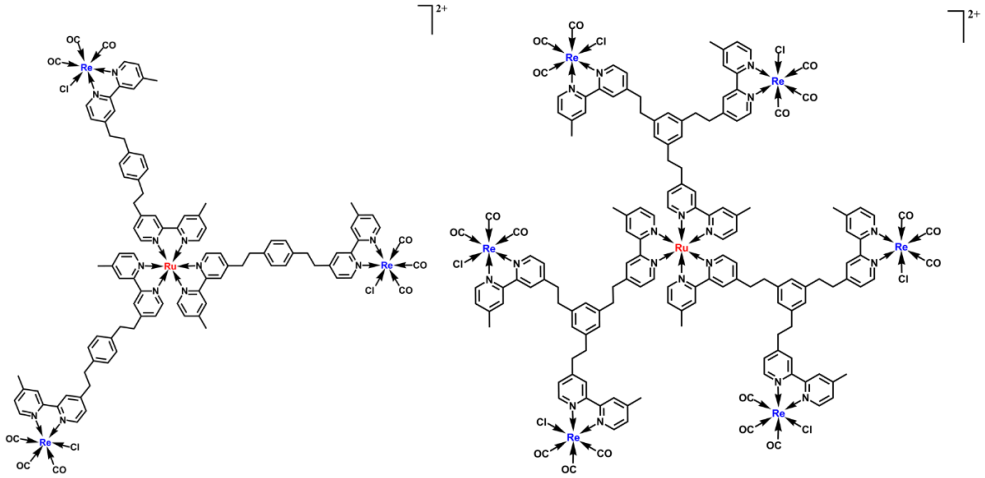

Figure 5.37. *Structure of the multinuclear complexes* ***RuRe3*** *(left) and* ***RuRe6*** *(right).*

For this reason, by using bridging ligands **bpy$_2$Ph** and **bpy$_3$Ph** as components, two new multinuclear complexes containing only one photosensitizer unit and three or six catalysts units (respectively **RuRe3** and **RuRe6** in **Figure 5.37**) have been designed and synthesized.

As shown in **Figure 5.37**, the **RuRe3** and **RuRe6** complexes belong to the class of dendrimers. Generally, dendrimers present a tree-like structure (the name comes from Greek “dendrons”, which means tree) and can be synthesized via an iterative sequence of reaction steps. The synthetic strategies for the preparation are of two kinds: the divergent and the convergent approach.[27]

In the divergent approach, see **Scheme 5.9**, the dendrimer is synthesized starting from a core on which, by several reaction steps, repetitive units are assembled. The first reaction step leads to the formation of a first-generation dendrimer. In the case where the ancillary units contain further reactive sites the first-generation dendrimer can react again to increase the generation. Such process can be iterated in order to obtain successive generations. This synthetic path grants a rapid increasing of the peripheral sites of the system.

The second synthetic approach is the convergent one, see **Scheme 5.10**.

In this case, the dendritic structure is build up starting from the periphery: the first step is the synthesis of ramification and the final step is to assemble these ramifications on the core. In the case of dendrimer systems based on metal center, the starting building block can be defined (as in the former syntheses of metal complexes) in function of the reactive sites as metal-complexes and ligand-complexes.

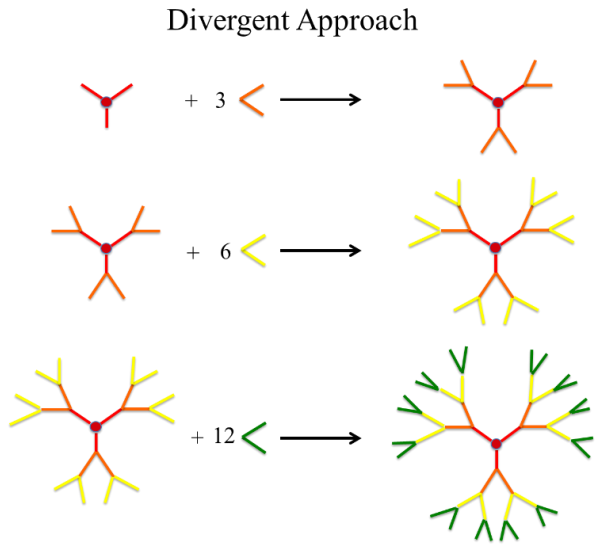

Scheme 5.9.

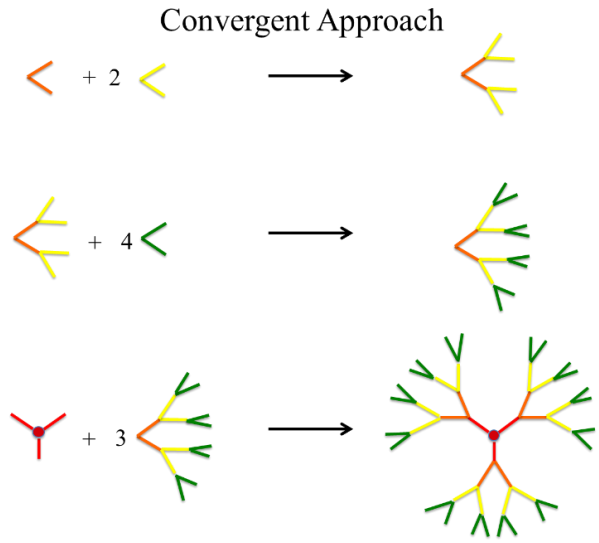

Scheme 5.10.

At first, the synthetic strategy adopted to obtain multinuclear systems were the divergent one.

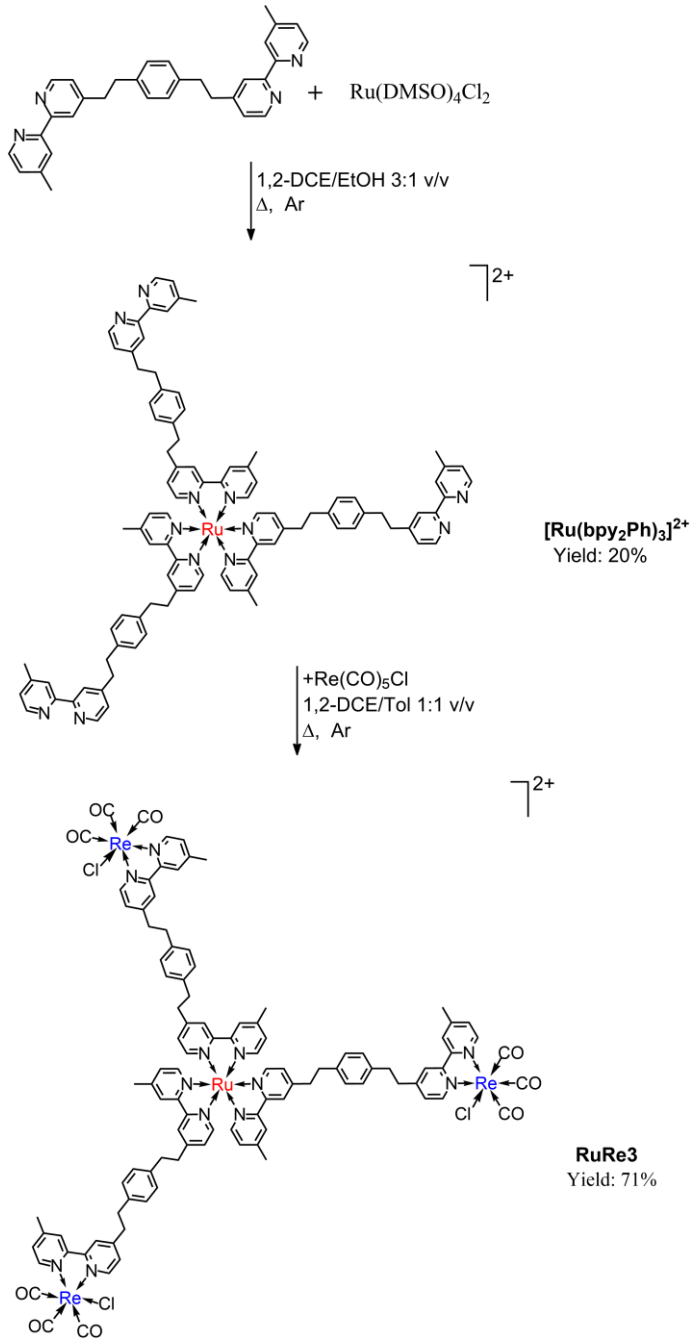

Scheme 5.11.

The linear ligand **bpy$_2$Ph** was employed to synthetize the mononuclear species **[Ru(bpy$_2$Ph)$_3$]$^{2+}$**. The reaction was conducted with an excess of ligand **bpy$_2$Ph**

in respect to the metallic precursor **$Ru(DMSO)_4Cl_2$** using as solvent a 1,2-DCE/EtOH (3:1, v/v) mixture as shown in **Scheme 5.11**. In these experimental conditions, the presence of two equivalent chelating sites with poor electronic communication among them, leads to the formation of an orange crude. The equivalent reactivity of the two chelating sites leads also to the formation of several multinuclear by-products with the mononuclear required complex. The crude was purified by size exclusion chromatography (using Sephadex LH-20 as stationary phase) and ethanol as eluent. The mononuclear complex was isolated as PF_6^- salt from the first eluted fraction with a yield of about 20%. The mononuclear species has been employed as ligand-complex in the following synthetic step. Consequently, the second synthetic step was the reaction of the ligand-complex **$[Ru(bpy_2Ph)_3]^{2+}$** with a strong excess of **$Re(CO)_5Cl$** in 1,2-dichloroethane/toluene (1:1 v/v) at reflux under inert atmosphere (**Scheme 5.11**). The reaction was controlled using the UV-Vis absorption spectroscopy following the presence of the new **$Re(dmb)(CO)_3Cl$** ^{1}MLCT absorption band at 360 nm. The product was purified by precipitation in diethylether to remove the unreacted rhenium precursor. The final **RuRe3** product was obtained with a yield of 32%.

A similar synthetic strategy was adopted to prepare the heptanuclear species. The **bpy_3Ph** ligand was employed to synthetize the mononuclear species **$[Ru(bpy_3Ph)_3]^{2+}$** as shown in **Scheme 5.12**.

The presence of three equivalent chelating sites with poor electronic communication among them, leads to an even more unspecific reaction. Particularly, despite the precaution such as a huge excess of ligand in respect to the metal precursor, several multinuclear species, hard to characterize and isolate, were obtained. The orange crude was purified, as in the previous synthesis, at first by size exclusion chromatography. The first eluted band was further purified by chromatography using alumina as stationary phase and DCM/EtOH (9:1, v/v) as mobile phase. The **$[Ru(bpy_3Ph)_3]^{2+}$** mononuclear complex was isolated as PF_6^- salt with a yield of around 15%. The core has been employed as ligand-complex

in the following synthetic step in order to obtain the final complex **RuRe6**, shown in **Scheme 5.12**.

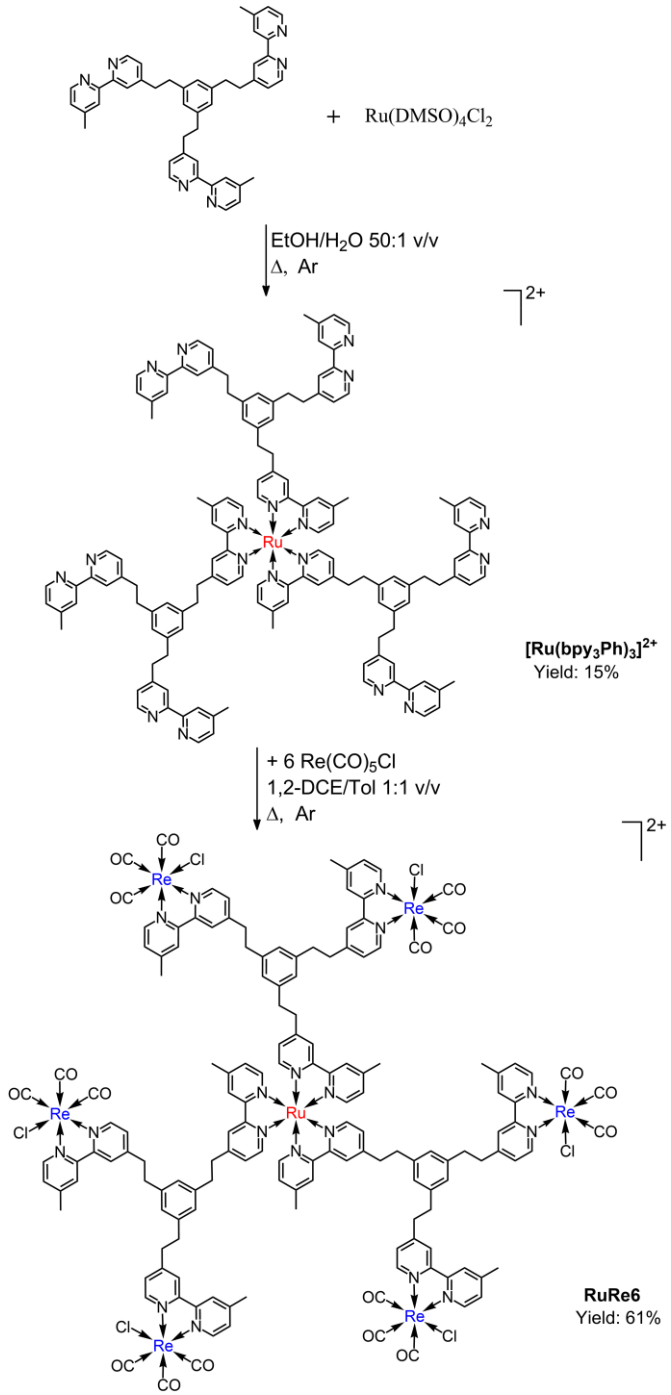

Scheme 5.12.

Consequently, the second synthetic step was the reaction of the ligand-complex **$[Ru(bpy_3Ph)_3]^{2+}$** with a strong excess of **$Re(CO)_5Cl$** in 1,2-dichloroethane/toluene (1:1 v/v) at reflux under inert atmosphere (**Scheme 5.12**). The reaction was controlled using the UV-Vis absorption spectroscopy following the presence of the new **$Re(dmb)(CO)_3Cl$** ^{1}MLCT absorption band at 360 nm. The product was purified by precipitation in diethylether to remove the unreacted rhenium precursor. The final **RuRe6** product was obtained with a yield of 32%.
In order to increase the reaction yield and minimize the by products (and as consequence also the waste of reactant) a convergent approach was adopted.

A huge excess of the ligand **bpy_2Ph** was solubilized in toluene and it was put to react with **$Re(CO)_5Cl$** solubilized in methanol added slowly to the ligand solution (see **Scheme 5.13**). The final product **$Re(bpy_2Ph)(CO)_3Cl$** was extracted from the crude with acetonitrile. The yellow final product was obtained with a yield of 65%. The product **$Re(bpy_2Ph)(CO)_3Cl$** was put to react, in huge excess, with **$Ru(DMSO)_4Cl_2$** using as solvent a mixture 1,2- DCE/EtOH (1:1, v/v) under argon atmosphere at reflux. The yellow mixture became orange.
The crude product was purified by column chromatography using alumina as stationary phase and acetonitrile/toluene (3:1, v/v) as eluent. The final product was isolate as PF_6^- salt with a yield of 20%.
A similar synthetic strategy was adopted to prepare the heptanuclear species. The ligand **bpy_3Ph** was solubilized in toluene and it was put to react with **$Re(CO)_5Cl$** solubilized in methanol added slowly to the ligand solution (see **Scheme 5.14**). The presence of three equivalent bipyridine moieties with poor electronic communication among them, led to an even more unspecific reaction.
For this reason the ligand **bpy_3Ph** was put in ratio 3.5:2 in respect to the precursor **$Re(CO)_5Cl$**. The final product **$Re_2(bpy_3Ph)$** was extracted from the crude with acetonitrile. The yellow final product was obtained with a yield of 60%. The product **$Re_2(bpy_2Ph)$** present another free chelating site so, it was put to react, in

huge excess, with **Ru(DMSO)$_4$Cl$_2$** using as solvent a mixture 1,2-DCE/EtOH (1:1, v/v) under argon atmosphere at reflux.

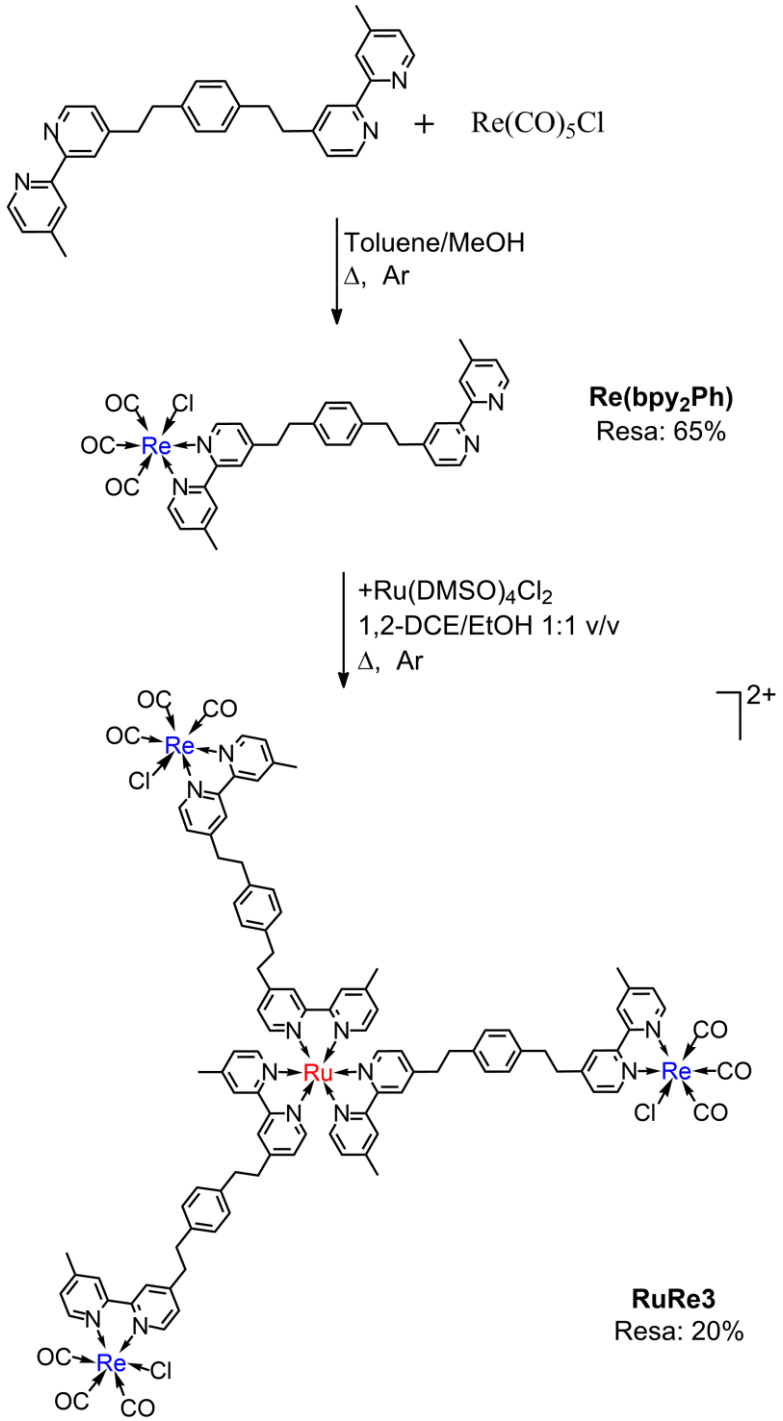

Scheme 5.13.

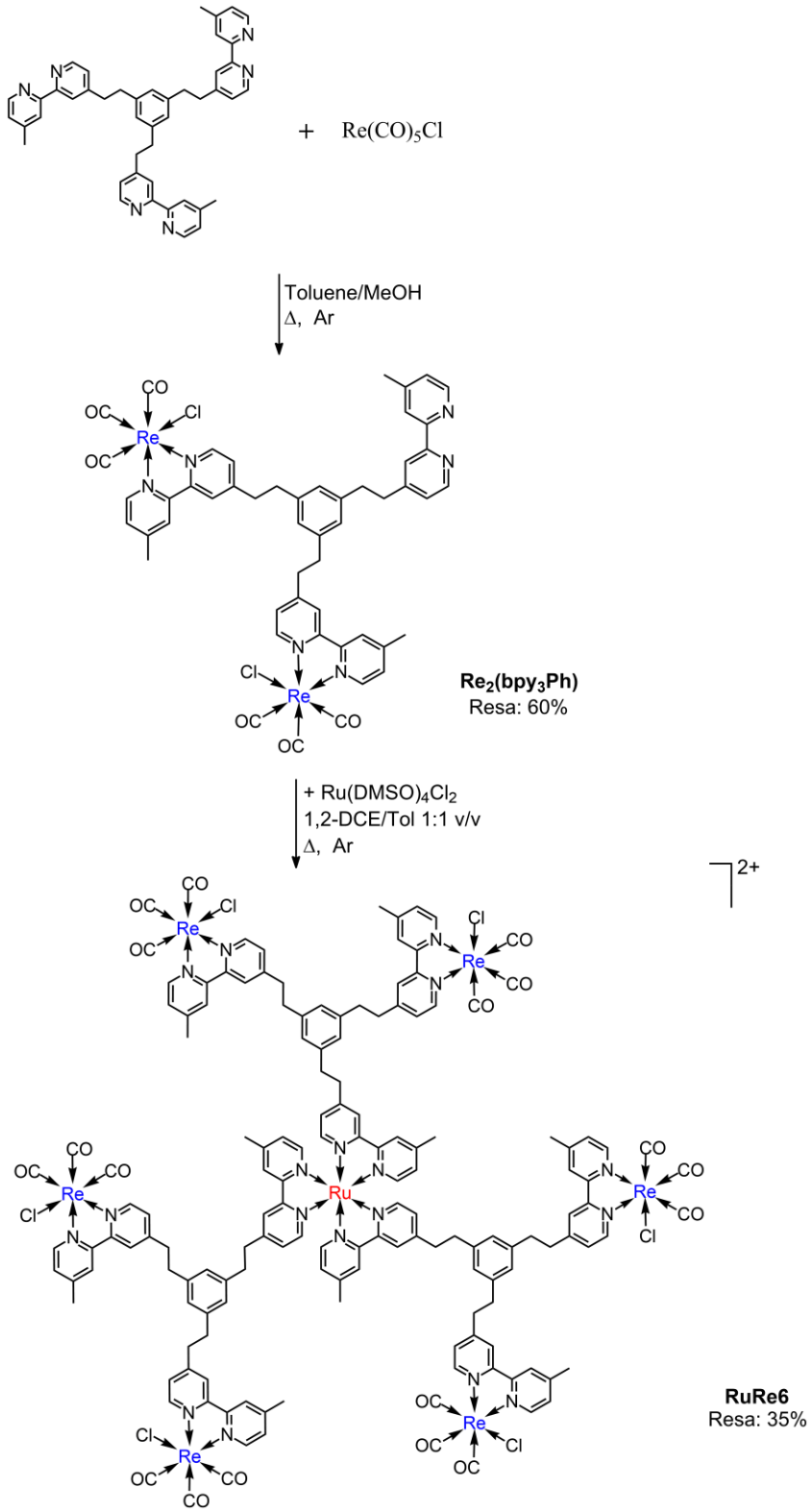
+ Re(CO)5Cl
Toluene/MeOH
Δ, Ar
Re2(bpy3Ph)
Resa: 60%
+ Ru(DMSO)4Cl2
1,2-DCE/Tol 1:1 v/v
Δ, Ar
2+
RuRe6
Resa: 35%

Scheme 5.14.

The yellow mixture became orange. The crude was purified by column chromatography using alumina as stationary phase and acetonitrile/toluene (3:1, v/v) as eluent. The product was isolated as PF_6^- salt with a yield of 35%.

5.4.1.1 Absorption Spectra and Photophysical Properties

The absorption spectra of the new species **RuRe3** and **RuRe6** in acetonitrile are reported in **Figure 5.38** and **Figure 5.39** and the spectroscopic and photophysical data are reported in **Table 5.14**.

As it can be observed in **Figure 5.38** and **Figure 5.39**, the absorption spectra of the mononuclear **Ru(bpy$_2$Ph)$_3$** and **Ru(bpy$_3$Ph)$_3$** species are characterized by a strong absorption band between 450 and 465 nm assigned to spin-allowed transition ^{1}MLCT (metal to ligand charge transfer) which involves a charge transfer from orbital mainly centred on the Ru(II) to an orbital mainly centred on the polypyridine ligands. In the UV-Vis region, at around 280 nm, it is possible to observe an intense absorption band due to the π-π* transition centred on the orbitals of the ligands.

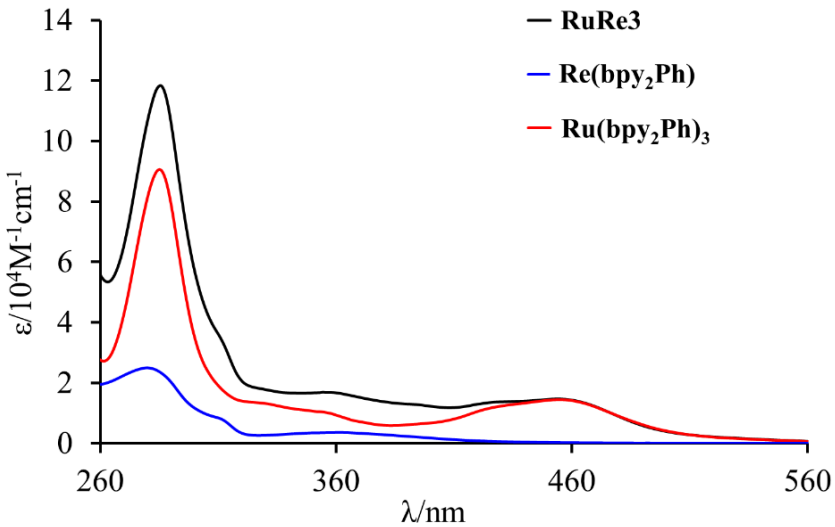

Figure 5.38. *Absorption spectra of **Ru(bpy$_2$Ph)$_3$** (**red** solid line), **Re(bpy$_2$Ph)** (**blue** solid line) and **RuRu3** (**black** solid line) in acetonitrile at room temperature.*

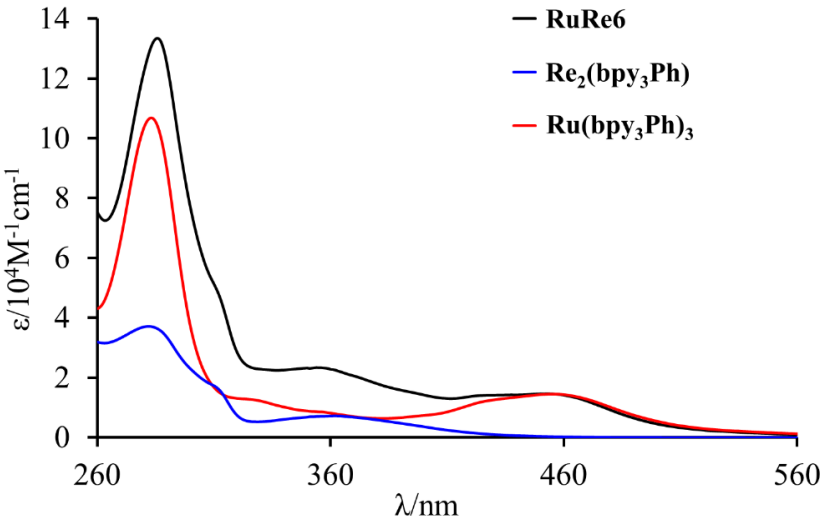

Figure 5.39. *Absorption spectra of* ***Ru(bpy$_3$Ph)$_3$*** *(**red** solid line),* ***Re$_2$(bpy$_3$Ph)*** *(**blue** solid line) and* ***RuRu6*** *(**black** solid line) in acetonitrile at room temperature.*

In the spectra of the multinuclear species it is possible observing a further band in the spectral range between 300 and 400 nm due to the transition ^{1}MLCT involving the rhenium subunits and the polypyridine ligands.

Table 5.14. *Photophysical properties measured in deaerated MeCN*[(a)]

	Absorption	Luminescence		
	λ_{max} /nm (ε_{460}/M^{-1}cm^{-1})[(b)]	λ_{max} / nm	τ / ns [(c)]	Φ_{em} [(c)]
Ru(bpy$_2$Ph)$_3$	455 (14500)	623	878 (120)	0.085 (0.016)
Ru(bpy$_3$Ph)$_3$	460 (14300)	623	851 (115)	0.086 (0.016)
Re(bpy$_2$Ph)	360 (3580)	608		
Re$_2$(bpy$_3$Ph)	360 (7100)	607		
RuRe3	454 (14500)	624	867 (119)	0.085 (0.016)
RuRe6	460 (18550)	625	852 (117)	0.086 (0.016)
[Ru(dmb)$_3$]$^{2+}$[(d)]	458 (16300)	622	875	0.089[(e)]
Re(dmb)CO$_3$Cl	364 (3630) [(f)]	600[(g)]	49[(g)]	0.0057[(h)]

(a) All data are measured in MeCN at 293 K. (b) Only the low energy maximum is reported. (c) Data in parenthesis refer to air-equilibrated solution. (d) From reference 7. (e) From reference 8. (f) From reference 9. (g) From reference 10. (h) In MeTHF.

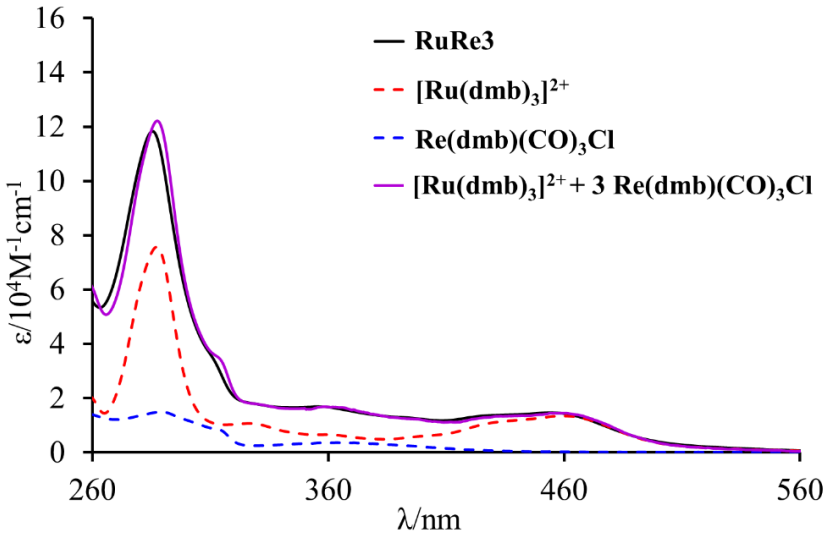

Figure 5.40. *Absorption spectra of the model species* ***[Ru(dmb)$_3$]$^{2+}$*** *(**red** dashed line),* ***Re(dmb)CO$_3$Cl*** *(**blue** dashed line) and their sum (**violet** solid line) superimposed with the spectra of the heptanuclear species* ***RuRe3*** *(**black** solid line).*

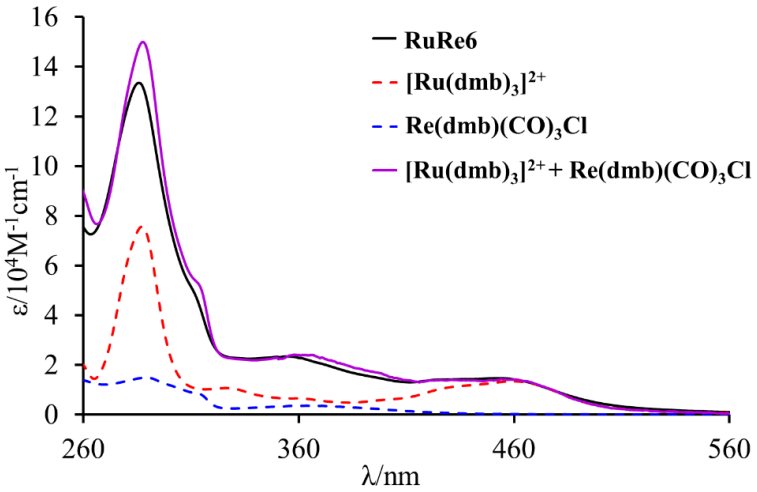

Figure 5.41. *Absorption spectra of the model species* ***[Ru(dmb)$_3$]$^{2+}$*** *(**red** dashed line),* ***Re(dmb)CO$_3$Cl*** *(**blue** dashed line) and their sum (**violet** solid line) superimposed with the spectra of the heptanuclear species* ***RuRe6*** *(**black** solid line).*

The intensity of this band is proportional to the number of the Re(I) subunits in the final supramolecular complexes. The spectra obtained by summing the spectra

of the model species of Ru(II) and Re(I) in 1:3 and 1:6 ratio, can be superimposed with the ones of the multinuclear species **RuRe3** and **RuRe6**, see **Figure 5.40** and **Figure 5.41**.

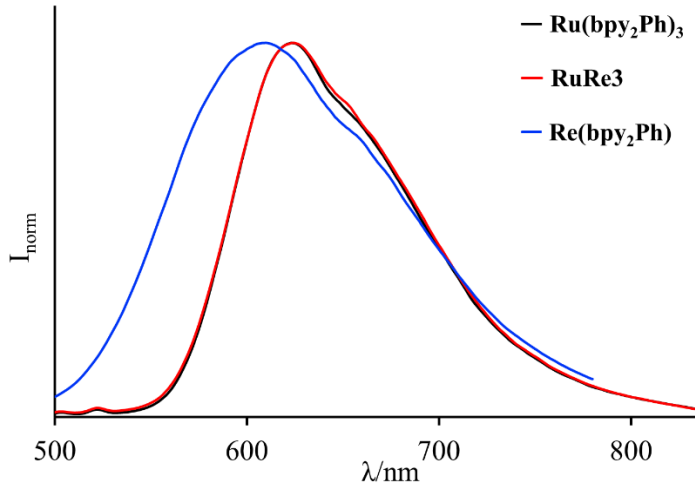

Figure 5.42. *Emission spectra of* ***Ru$_2$(bpy$_3$Ph)*** *(**black** solid line) and* ***RuRe3*** *(**red** solid line) in acetonitrile at room temperature at λ_{exc} = 450 nm and* ***Re(bpy$_2$Ph)*** *(**blue** solid line) in acetonitrile at room temperature at λ_{exc} = 400 nm.*

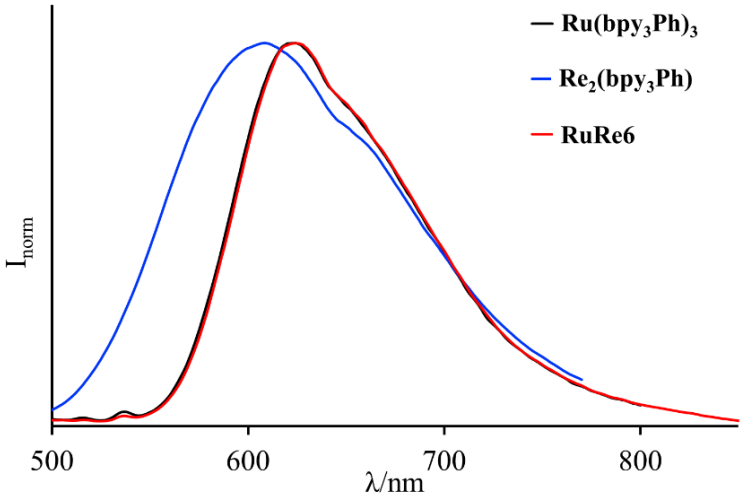

Figure 5.43. *Emission spectra of* ***Ru(bpy$_2$Ph)*** *(**black** solid line) and* ***RuRe6*** *(**red** solid line) in acetonitrile at room temperature at λ_{exc} = 450 nm and* ***Re$_2$(bpy$_3$Ph)*** *(**blue** solid line) in acetonitrile at room temperature at λ_{exc} = 400 nm.*

This confirms that there is no electronic communication in the ground state among the metal centers in **RuRe3** and **RuRe6** supramolecular complexes.

All the synthesized species are luminescent at room temperature in fluid solution of acetonitrile as it is possible to observe in **Figure 5.42**, **Figure 5.43** and **Table 5.14**. In the case of the mononuclear **Ru(bpy$_2$Ph)$_3$** and **Ru(bpy$_3$Ph)$_3$** species the emissions are due to the deactivation of the excited state ^{3}MLCT of the Ru(II). The emission quantum yield and lifetime are the same as the ones of the model species **[Ru(dmb)$_3$]$^{2+}$**. The emissions of the mononuclear **Re(bpy$_2$Ph)** and binuclear **Re$_2$(bpy$_3$Ph)** metal complexes present the maxima similar to the one of the model species **Re(dmb)(CO)$_3$Cl** and a shorter wavelength (about 15 nm less) respect to the emission of the ruthenium center. It is possible to affirm that, as consequence of the low quantum yield of the Re(I) subunits in respect to the Ru(II) subunit, the emissions of the tetranuclear and heptanuclear species are due to the independent deactivation of two isoenergetic states localized respectively on the rhenium and ruthenium subunits.

5.4.1.2 Redox Properties

The redox properties of the species prepared have been investigated by voltametric analysis, such as cyclic, differential pulsed and square wave voltammetry. The results are summarized in **Table 5.15**.

The mononuclear species **Ru(bpy$_2$Ph)$_3$** shows only one oxidation process attributed, by comparison with the potential of the model species **[Ru(dmb)$_3$]$^{2+}$**, to the monoelectronic reversible oxidation of the ruthenium centre (see **Figure 5.44**).

In reduction it is possible to observe two reduction processes (with intensity comparable with the oxidation process) attributable to the reduction of the first and second bipyridine coordinated to the metal center; at more negative potential there is the reduction of the third bipyridine coordinated to the metal center and of the free bipyridines subunits (see **Figure 5.45**).

Table 5.15. *Redox properties*

	$E_{1/2}$, V vs SCE[(a)]				
	E_{Ox2}	**E_{Ox1}**	**E_{Red1}**	**E_{Red2}**	**E_{Red3}**
$Ru(bpy_2Ph)_3$		+1.15 [1]	-1.41 [1]	-1.59[1]	-1.86 irr.
$Ru(bpy_3Ph)_3$		+1.14 [1]	-1.40 [1]	-1.58[1]	-1.89 irr
$Re(bpy_2Ph)$		+ 1.36 irr	-1.41		
$Re_2(bpy_3Ph)$		+1.37 irr	-1.40		
RuRe3	+1.31 irr	+1.15 [1]	-1.41[4]		
RuRe6	+1.38 irr	+1.17 [1]	-1.42[7]		
$[Ru(dmb)_3]^{2+}$[(b)]		+1.10 [1]	-1.45[1]		
$[Re(dmb)(CO)_3Cl]$[(c)]		+1.36 irr	-1.43 [1]		

(a) Electrochemical Properties measured at room temperature in MeCN containing 0.1 M TBAH. All values are obtained using the redox couple ferrocene/ferrocenium (395 mV vs. SCE in acetonitrile) as internal reference. The numbers in parentheses refer to the number of exchanges electrons. Irr indicates an irreversible process: in this case, the E values reported in table refer to peak potentials in pulse voltammetry experiments. (b) From reference 11. (c) From reference 10.

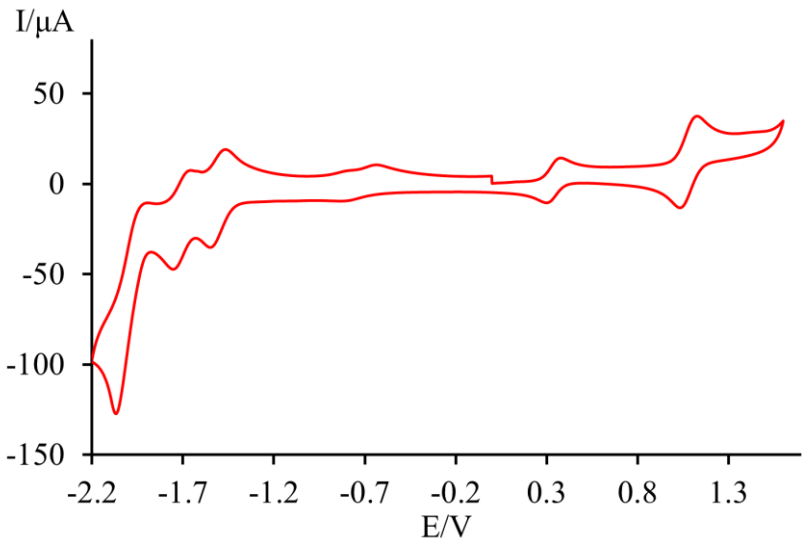

Figure 5.44. *Cyclic voltammogram of **$Ru(bpy_2Ph)_3$** (0.5 mM) in argon purged MeCN at room temperature using Bu_4NPF_6 (0.1 M) as supporting electrolyte. As internal reference was used the redox couple ferrocene/ferrocenium (395 mV vs. SCE in acetonitrile). Scan rate 200 mV/s.*

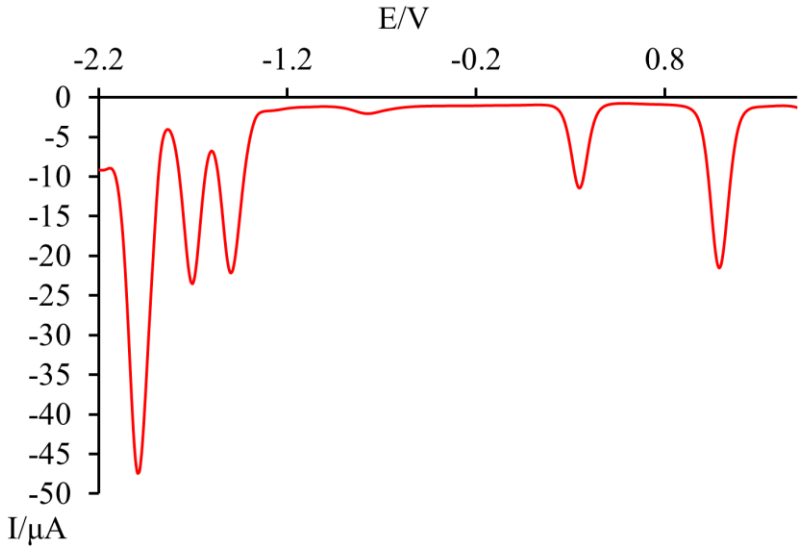

Figure 5.45. *DPV analysis of* ***Ru(bpy$_2$Ph)$_3$*** *(0.5 mM) in argon purged MeCN at room temperature using Bu_4NPF_6 (0.05 M) as supporting electrolyte. As internal reference was used the redox couple ferrocene/ferrocenium (395 mV vs. SCE in acetonitrile). Scan rate 20 mV/s.*

The voltammograms of the mononuclear species **Ru(bpy$_3$Ph)$_3$** present a similar behaviour. The species **Ru(bpy$_3$Ph)$_3$** shows only one oxidation process attributed, by comparison with the potential of the model species **[Ru(dmb)$_3$]$^{2+}$**, to the monoelectronic reversible oxidation of the ruthenium centre. In reduction it is possible to observe two reduction processes (with intensity comparable with the oxidation process) attributable to the reduction of the first and second bipyridine coordinated to the metal center; at a more negative potential there is the reduction of the third bipyridine coordinated to the metal center and of the six free bipyridines subunits (see **Figure 5.46**).

The precursor species **Re(bpy$_2$Ph)** and **Re$_2$(bpy$_3$Ph)**, present only one irreversible oxidation band at about +1.36 V, ascribable to the irreversible oxidation of the Re(I) metal center(s) and a reduction process attributable to the reduction of the bipyridine coordinate to the Re(I) metal center(s).

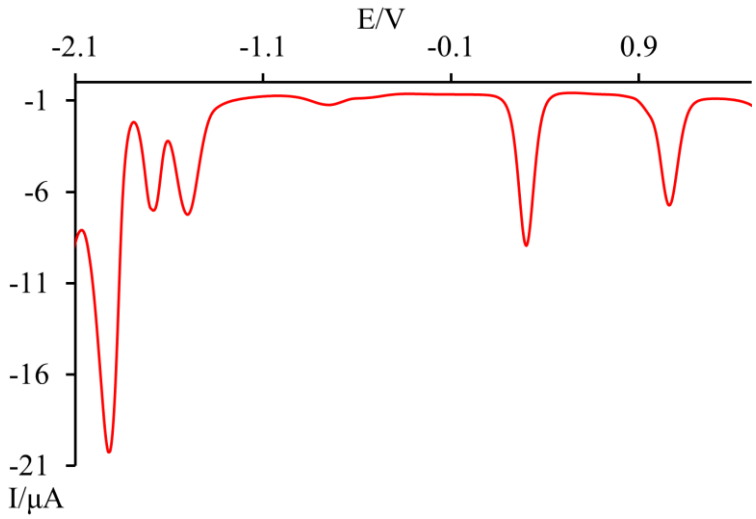

Figure 5.46. *DPV analysis of* ***Ru(bpy$_3$Ph)$_3$*** *(0.5 mM) in argon purged MeCN at room temperature using Bu_4NPF_6 (0.05 M) as supporting electrolyte. As internal reference was used the redox couple ferrocene/ferrocenium (395 mV vs. SCE in acetonitrile). Scan rate 20 mV/s.*

In the multinuclear complexes **RuRe3**, there are two processes in oxidation (see **Figure 5.47**). The first one at 1.14 assignable to the reversible monoelectronic oxidation of the Ru(II) core, the second one, at more positive potential, is due to the irreversible oxidation of the Re(I) centers.

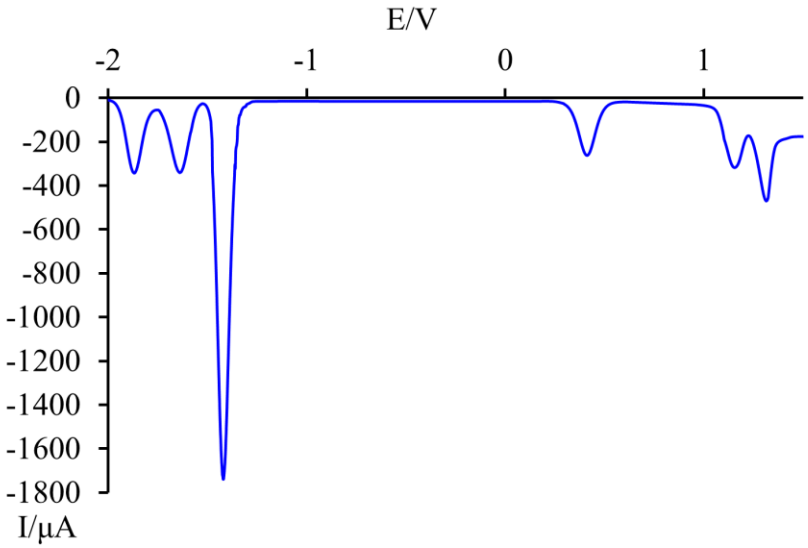

Figure 5.47. *DPV analysis of* ***RuRe3*** *(0.5 mM) in argon purged MeCN at room temperature using Bu_4NPF_6 (0.05 M) as supporting electrolyte. As internal reference was used the redox couple ferrocene/ferrocenium (395 mV vs. SCE in acetonitrile). Scan rate 20 mV/s.*

The comparison with the oxidation potential of the model species **[Ru(dmb)$_3$]$^{2+}$** and **Re(dmb)(CO)$_3$Cl**, shows as the electronic communication, from an electrochemical viewpoint, among the metal centers is negligeable. It is also possible observing in the voltammograms three reduction processes. The first reduction process at -1.40 V is due to the simultaneous and independent reduction of the three dmb coordinated to the Re(I) and the first dmb coordinated to the Ru(II) metal center. By comparing the reduction potential of the model species **[Ru(dmb)$_3$]$^{2+}$** and **Re(dmb)(CO)$_3$Cl** (see **Table 5.15**), it should be noted as the reduction potential of the dmb of the two species takes place at the same potential. The comparison between the peak area of the first oxidation and reduction processes, give the possibility to confirm that the process involves four electrons. Analogous behaviour is shown by the heptanuclear species **RuRe6**, in the same experimental condition. The voltammograms for the species **RuRe6** show two oxidation processes (see **Figure 5.47**).

The first one at 1.14 assignable to the reversible monoelectronic oxidation of the Ru(II) core, the second one, at more positive potential, is due to the irreversible oxidation of the Re(I) centers. The comparison with the oxidation potential of the model species **[Ru(dmb)$_3$]$^{2+}$** and **Re(dmb)(CO)$_3$Cl**, show as the electronic communication, from an electrochemical viewpoint, among the metal centers is negligeable. It is also possible observing in the voltammograms three reduction processes. The first reduction process at -1.40 V is due to the simultaneous and independent reduction of the six dmb coordinated to the Re(I) and the first dmb coordinated to the Ru(II) metal center. By comparing the reduction potential of the model species **[Ru(dmb)$_3$]$^{2+}$** and **Re(dmb)(CO)$_3$Cl** (see **Table 5.15**), it should be noted as the reduction potential of the dmb of the two species takes place at the same potential.

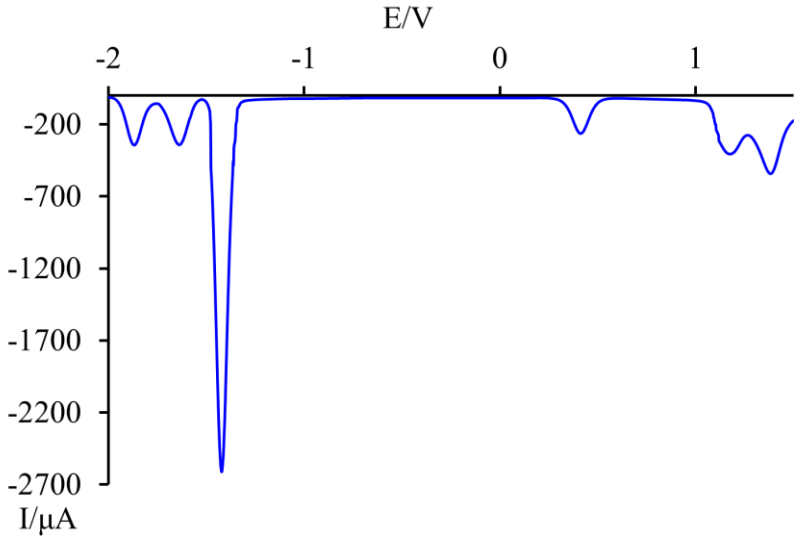

Figure 5.48. *DPV analysis of **RuRe6** (0.5 mM) in argon purged MeCN at room temperature using Bu_4NPF_6 (0.05 M) as supporting electrolyte. As internal reference was used the redox couple ferrocene/ferrocenium (395 mV vs. SCE in acetonitrile). Scan rate 20 mV/s.*

The comparison between the peak area of the first oxidation and reduction processes gives the possibility to confirm that the process involves seven electrons.

Unfortunately, the photocatalytic behaviour of the dendritic species **RuRe3** and **RuRe6**, due to the COVID pandemic, have been delayed, so this section is incomplete. However, we decided to report the synthesis as well as the absorption spectra, the photophysical properties and the redox behaviour of these new compounds and their components for completeness.

References

1. R. Dorta, R. Dorta, L. J. W. Shimon, D. Mistein, *Inorg. Chem.*, 2004, **43**, 7180-7186.
2. S. Campagna, F. Puntoriero, F. Nastasi, G. Bergamini, V. Balzani, *Top. Curr. Chem.*, 2007, **280**, 117-214.
3. Y. Yamazaki, H. Takeda, O. Ishitani, *Journal of Photochemistry and Photobiology C: Photochemistry Reviews*, 2015, **25**, 106-137.
4. J. Hawecker, J.-M. Lehn, R. Ziessel, *J. Chem. Soc., Chem. Commun.*, 1983, 536 - 538.
5. J. Hawecker, J.-M. Lehn, R. Ziessel, *Helv. Chim. Acta*, 1986, **69**, 1990 - 2012.
6. S. Serroni, S. Campagna, F. Puntoriero, C. Di Pietro, N. D. McClenaghan, F. Loiseau, *Chem. Soc. Rev.*, 2001, **30**, 367-375.
7. D. S. Tyson and F. N. Castellano, *J. Phys. Chem. A*, 1999, **103** (50), 10955-10960.
8. Y. Tamaki, K. Watanabe, K. Koike, H. Inoue, T. Morimoto and O. Ishitani, *Faraday Discuss.*, 2012, **155**, 115-127.
9. L. A. Worl, R. Duesing, P. Chen, L. Della Ciana, T. J. Meyer, *J. Chem. Soc., Dalton Trans.* 1991, **0**, 849-858.
10. M. Furue, M. Naiki, Y. Kanematsu, T. Kushida and M. Kamachi, *Coord. Chem. Rev.*, 1991, **111**, 221-226.
11. Y. Kawanishi, N. Kitamura, Y. Kim and S. Tazuke, *Riken Q.*, 1984, **78**, 212-219.
12. G. Sahara, O. Ishitani, *Inorg. Chem.*, 2015, **54**, 5096-5104.
13. Y. Kuramoki, M. Kamiya, H. Ishida, *Inorg. Chem.*, 2014, **53**, 3326−3332.
14. T. Morimoto, T. Nakajima, S. Sawa, R. Nakanishi, D. Imori, O. Ishitani, *J. Am. Chem. Soc.*, 2013, **135**, 16825-16828.
15. Y. Pellegrin and F. Odobel, *C. R. Chimie*, 2017, **20**, 283-295.
16. A. M. Cancelliere, F. Puntoriero, S. Serroni, S. Campagna, Y. Tamaki, D. Saito, O. Ishitani, *Chem. Sci.*, 2020, **11**, 1556 – 1563.

17. H. Takeda, K. Koike, T. Morimoto, H. Inumaru, O. Ishitani, *Advances in Inorganic Chemistry*, 2011, **63**, 137-186.
18. K. Koike, S. Naito, S. Sato, Y. Tamaki, O. Ishitani, *Journal of Photochemistry and Photobiology A: Chemistry*, 2009, **207**, 109–114.
19. Y. Kuramoki, O. Ishitani. H. Ishida, *Coordination Chemistry Reviews*, 2018, **373**, 333-356.
20. Y. Tamaki, O. Ishitani, *ACS Catal.*, 2017, **7**, 3394-3409.
21. E. Hasegawa, S. Takizawa, T. Seida, A. Yamaguchi, N. Yamaguchi, H. Chiba, T. Takahashi, H. Ikeda and K. Akiyama, *Tetrahedron*, 2006, **62**, 6581-6588.
22. S. Fukuzumi, S. Koumitsu, K. Hironaka and T. Tanaka, *J. Am. Chem. Soc.*, 1987, 109, 305-316.
23. P. A. Anderson, G. B. Deacon, K. H. Haarmann, F. R. Keene, T. J. Meyer, D. A. Reitsma, B. W. Skelton, G. F. Strouse, N. C. Thomas, J. A. Treadway, A. H. White, *Inorg. Chem.*, 1995, **34**, 6145−6157.
24. M. Kubeil, R. R. Vernooij, C. Kubeil, B. R. Wood, B. Graham, Holger Stephan, L. Spiccia, *Inorg. Chem.*, 2017, **56**, 5941−5952.
25. K. Sekizawa, K. Maeda, K. Domen, K. Koike, O. Ishitani, *J. Am. Chem. Soc.*, 2013, **135**, 12, 4596–4599.
26. E. Eskelinen, M. Maukka, T.-J.J. Kinnunen, T. A. Pakkanen, *Journal of Electroanalytical Chemistry*, 2003, **556**, 103-108.
27. F. Puntoriero, S. Serroni, G. La Ganga, A. Santoro, M. Galletta, F. Nastasi, E. La Mazza, A. M. Cancelliere, S. Campagna, *Eur. J. Inorg. Chem.*, 2018, 3887–3899 and references therein.

Chapter 6

Conclusions

A series of multinuclear metal complexes based on different bridging ligands with two, three and four chelating sites, have been synthesized. All the bridging ligands are constituted by a central phenyl ring connected in different positions with bipyridine subunits by ethylene chains. The metal complexes contain different numbers of $Ru(dmb)_3$-type chromophores which can act as photosensitizers for photoinduced CO_2 reduction, when $Re(dmb)(CO)_3Cl$-type or $Ru(dmb)(CO)_2Cl_2$-type based catalyst for the CO_2 reduction are integrated in the multinuclear arrays, thus yielding photosensitizer-catalyst (PS-CAT) supramolecular assemblies. The various supramolecular metal complexes prepared present different ratios of photosensitizer and catalysts. The molecular structure of the bridging ligands is unprecedented for bridging ligands connecting photosensitizers and catalysts for CO_2 reduction based on metal complexes, since it allows for larger separation among the active metal subunits.

The results clearly indicate that the metal subunits of the supramolecular systems keep their photophysical and redox properties and the electronic interactions among the metal centers are negligible. The PS-CAT metal complexes which present the Re(I) catalysts subunits show an efficient light-induced CO_2 reduction with formation of CO, with outstanding turnover number in most of the cases. For example, the trinuclear complexes **Ru2Re** and **RuRe2** photocatalyze CO_2 reduction to CO with high selectivity (up to 97%) and high durability (TON of 5232 and 6038, respectively), which are the largest TONs for CO_2 reduction using supramolecular photocatalysts in homogeneous solutions reported in literature. The metal complexes which present the Ru(II) based catalyst show a quite good photocatalytic ability for the HCOOH formation. The results exposed in the

present thesis clearly indicate that the bridging ligands with two and three bipyridine moieties can allow to obtain efficient long range electron transfer (suitable for the photocatalytic process) without affecting the behaviour of the catalytic subunit.

The metal complexes with only one photosensitizer unit and two catalysts units present the best photocatalytic activity for the CO_2 reduction. On the basis of this results, a second generation of multinuclear Ru/Re photocatalytic complexes were prepared, namely a tetranuclear and a heptanuclear dendrimer species which contain only one photosensitizer unit and respectively three and six catalysts units within their structure. For the synthesis of these complexes, divergent and convergent approaches have been employed. The more productive synthetic approach was the convergent one. Also these complexes keep their photophysical and redox properties. The study of the photocatalytic abilities of these latter, dendritic-shaped tetranuclear and heptanuclear metal complexes, however, have been delayed because of the COVID-19 pandemic, so while photophysical and redox properties are here reported, complete investigation of their properties is still running.

All together, these achievements represent a breakthrough in the design of novel supramolecular photocatalysts, allowing to overcome the size limit in bridging ligand represented by the ethylene bridges most commonly used in efficient PS-CAT supramolecular photocatalysts reported up to now. Actually, the present results indicate that new bridging ligands in which aromatic moieties are judiciously incorporated within the bridging ligand structure can allow to obtain fast long-range electron transfer, suitable for the photocatalytic process, without affecting the behaviour of the catalytic subunit(s). This can open new avenues for the design of new, more efficient and stable supramolecular photocatalysts for selective CO_2 photoreduction.

Chapter 7

PhotoElectrocatalysis for CO_2 Reduction – An Appendix

As discussed in Chapter 4 and 5 and widely reported in literature,[1,2] suitable combination of molecular photosensitizer and catalyst can perform photocatalytic CO_2 reduction with high stability, efficiency and selectively. Also photoelectrochemical CO_2 reduction could be one of the most promising way to obtain renewable energy source[3] and devices have been designed specifically for such conversion schemes, some of them integrating convincingly molecular components into hybrid electrode materials.[4] The conversion performances of such photoelectrochemical cell (PEC, see **Figure 6.1**) depends on the efficiency of prepared and integrated photoelectrodes, on the overall stability and on the fast surface redox reaction.[5]

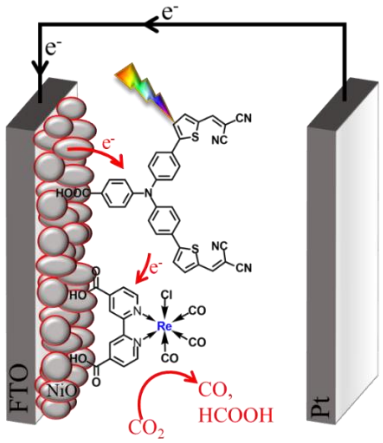

Figure 6.1. *Schematic representation of a PEC device composed of a photocathode and a Pt anode, operating in aqueous media (not represented here for clarity). The photocathode is here based on mesoporous NiO film sensitized with an organic dye (P1) and a catalyst for the CO_2 reduction.*

An ideal photoelectrochemical cell consists of a photocathode and a photoanode (*i.e.* "tandem cell" with electrodes being both photoactive). In this kind of cell the

electron and hole, generated under illumination, are separated and transferred to the respective catalysts loaded on the photoelectrodes surfaces to perform the catalytic reactions for the production of fuels. Electrons are directed to the reductive side (the photocathode), while holes are directed to the oxidative side (the (photo)anode).

An attractive photocathode material is p-type nickel oxide (NiO) semiconductor for which the band edges are suitably located for the CO_2 reduction.[6,7,8,9] However, the photosensitization of wide band gap NiO (*ca.* 3.6 eV) is required in order to improve its capacity in visible-light-harvesting. Hybrid photocatalytic systems composed by photosensitized NiO electrode and a suitable catalyst for CO_2 reduction have been successfully investigated.[10] Dye **P1** (4-[Bis(4-{5-[2,2-dicyanovinyl]-thiophene-2-yl}phenyl)amino]benzoic acid) (**Figure 6.2**) can be used as photosensitizer for p-type electrodes as it can be anchored on NiO through the carboxylic acid group:[11] its push-pull nature facilitates electron transfer from NiO to the reduction catalyst (acceptor CN groups being far from the oxide). Re(I) metal complexes based on CO and bipyridines ligands are tuneable and efficient catalysts in CO_2 reduction.[12] In particular, modification in the organic ligand backbone of the complex allows to tune its electronic/redox properties and to control its incorporation in the hybrid material *via* the introduction of anchoring groups.

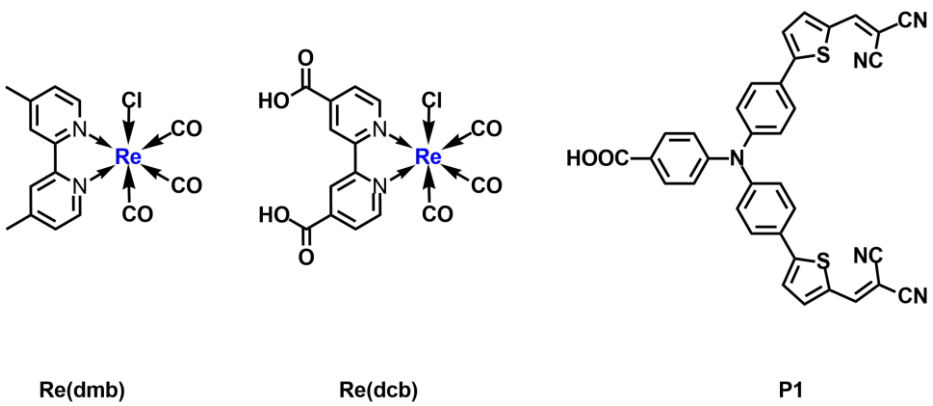

Re(dmb) Re(dcb) P1

Figure 6.2. *Molecular structures of the molecular catalysts for the CO_2 reduction Re(dmb) and Re(dcb) and P1 dye.*

The present work was projected and realized in collaboration with Dr. Marie-Pierre Santoni and with the help of Dr. Hasina Ramanitra, in Université de Paris (ITODYS laboratory). It focused on the elaboration of new types of modified NiO-P1 photocathodes for CO_2 reduction and Dye-Sensitized PhotoElectrosynthetic Cells prototypes (one photocathode, see **Figure 6.3**, coupled with a Pt anode). The novel aspects here were: (i) new combinations of proven molecular components to be heterogenized on NiO electrodes; and (ii) the engineering of the interfaces between units (dye, catalyst) and charge-transporting material (semi-conductor). Indeed, the controlled incorporation of those functional units into hybrid materials and devices is critical for the overall device performances, by directing charge transfer/transport and limiting charge recombination. Our objective was to make progress in the understanding of processes (charge transfers and transport, catalytic mechanisms), by establishing correlations between structure and properties toward a rationalized design. Our long-term objective is to implement such photoelectrodes, based on our designed molecular components, in various types of devices, including tandem cells (obtained by combining n- and p-type photoelectrodes).

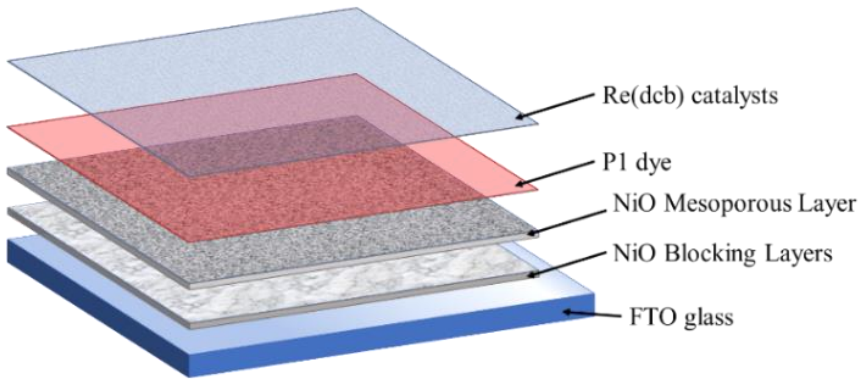

Figure 6.3. *Layer-by-layer composition of modified photoelectrodes targeted for PEC devices and CO_2 reduction.*

Two molecular catalysts were synthesized according to previous reports: **Re(dmb)(CO)$_3$Cl**, (hereafter called **Re(dmb)**) used here as a reference (no

anchoring group for specific integration into the material) and **Re(dcb)(CO)$_3$Cl** (**Re(dcb)** from now) (where dmb = 4,4'-dimethyl-2,2'-bipyridine and dcb = 4,4'-dicarboxyl-2,2'-bipyridine)). New photocathodes, based on **P1** dye and a Re(I) catalyst were prepared, characterized and studied for CO_2 reduction.

6.1 Preparation of modified photoelectrodes FTO/NiO-Dye/Catalyst

The NiO mesoporous electrodes on FTO (Fluorine Tin Oxide glass) substrate were prepared in two steps following the procedures reported in literature.[13] The first step consists in the preparation of two compact superimposed blocking layers,[14] the second one is the deposition of the mesoporous NiO layer.[15] The photosensitization of NiO was performed by soaking the **FTO/NiO** electrode in an ethanol solution 0.3 mM of **P1** for 16 hours. The obtained **FTO/NiO-P1** electrode was washed with acetonitrile and dried in air.

Two Re(I) catalysts were synthesized as reported in literature:[16] **Re(dcb)(CO)$_3$Cl** and **Re(dmb)(CO)$_3$Cl.** Identity and purity of each complex was verified using ^{1}H-NMR and IR spectroscopies. The deposition of the molecular catalyst, as the top layer of the photocathode, was performed using the dropcasting method: a solution of **Re(dcb)(CO)$_3$Cl** (0.3 mM in acetonitrile) was drop-casted on the surface of the **FTO/NiO-P1** electrodes to yield the modified photoelectrodes **FTO/NiO-P1/Re(dcb)**. The amount of deposited Re(I) catalyst was varied in order to optimize the preparation of the catalyst film (**Table 6.1**).

In order to study the behaviour of the Re(I) catalyst anchored on the NiO or not, **FTO/NiO/Re(dcb)** and **FTO/Re(dcb)** electrodes were also prepared for a comparative study. All the electrodes were characterized by UV-Vis and IR spectroscopy.

Table 6.1 *Conditions tested for the optimization of the catalyst film preparation, using an acetonitrile solution of* ***Re(dcb)(CO)$_3$Cl*** *(0.3 mM).*

DEPOSITION METHOD	Dropcasting 1 drop = 70 μL	Dropcasting 2 drops	Dropcasting 4 drops
QUANTITY of deposited catalyst	24 nmol	48 nmol	96 nmol
ASPECT of obtained films	Total coverage Homogeneous	Total coverage Homogeneous	Total coverage Homogeneous

Morphological characterization of the obtained (photo)electrodes using Scanning Electron Microspcopy (surface and cross-section imaging) are in progress in Paris. It will give important information about the homogeneity and thickness of the films prepared and constituting the modified photoelectrode.

6.2 Spectroscopic characterization of molecular components and of the FTO/NiO-P1/Re electrode

The photophysical properties in acetonitrile solution of molecular components **Re(dcb)** and **P1** are reported in **Table 6.2** and the absorption spectra are shown in **Figure 6.4**.

Table 6.2. *Photophysical properties measured in deaerated MeCN at 293K.*

	Absorption	Luminescence		
	λ/nm (ε/$M^{-1}cm^{-1}$)[b]	λ_{max}/ nm	τ / ns [a]	Φ_{em} [a]
P1[b]	468 (58000)	650	30 ps[c]	
Re(dcb)(CO)$_3$Cl[d]	240 (71100) 309 (40500) 400 (9800)	720	0.015 (0.012)	<1% (<1%)

(a) Data in parenthesis refer to air-equilibrated solution. (b) From reference 11. (c) From reference [17] (d) From reference ***Errore. Il segnalibro non è definito.***.

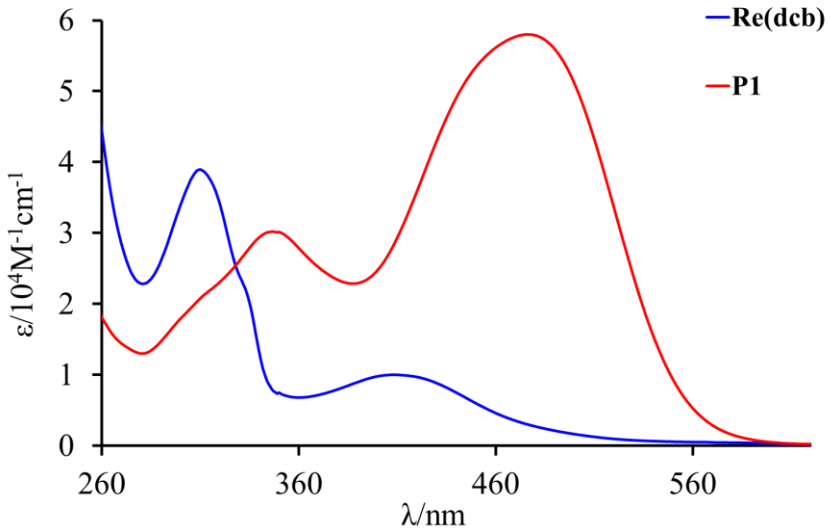

Figure 6.4. *Absorption spectra in acetonitrile at room temperature of Re(dcb) (**blue** solid line) and P1 (**red** solid line).*

The **Re(dcb)** absorption spectrum presents a ^{1}MLCT band at 400 nm and a LC π-π* transition at 310 nm. The **P1** absorption spectrum shows two π-π* absorption bands at around 350 and 470 nm with a quite high molar extinction coefficient.

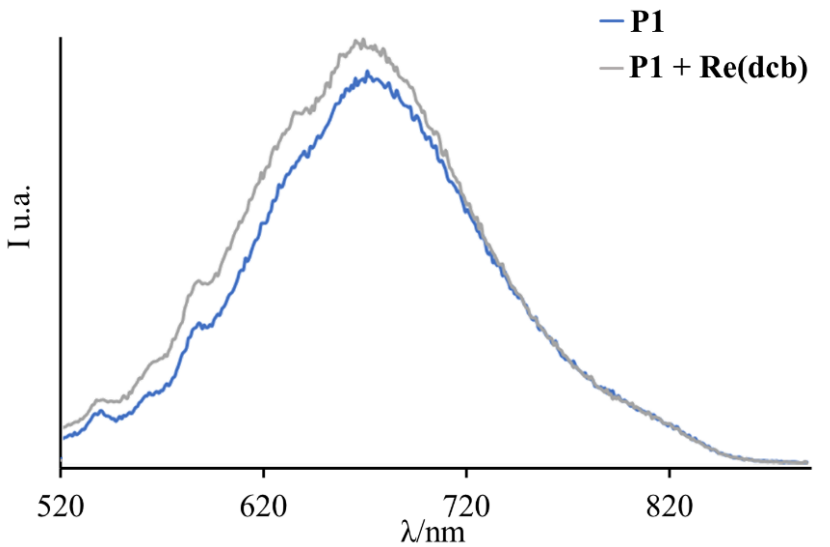

Figure 6.5. *Emission spectra of **P1** (2.5 μM) (**blue** solid line) and **P1** and **Re(dcb)** (30 mM) (**grey** solid line) in acetonitrile. The slight decrease in fluorescence intensity measured is due to the small dilution effect.*

In addition, a control quenching experiment was performed to verify that there is no competitive process (back electron transfer) possible between the dye and the catalyst (see **Figure 6.5**).

Even in large excess, the catalyst cannot quench the fluorescence of the P1 dye (by oxidative quenching, D* transfers an e^- to Re to give D^+ and Re^-). This may be due to slow kinetics for this electron transfer, which will be unable to compete with fast electron injection from NiO(VB). In conclusion, both components are well matched as they do not compete with each other, both regarding visible light absorption and electron transfers to the reduction catalyst.

As shown in **Figure 6.6**, after the sensibilization of the **FTO/NiO** electrodes there is a red shift of the absorption maximum of **P1** dye in **FTO/NiO-P1** electrode of around 30 nm.

This shift could be attributed to the coupling of the dye with the semiconductor.[11] The dye loading has previously been estimated to be *ca.* 15 nmol·cm^{-2}.[13] In the completed electrode **FTO/NiO-P1/Re(dcb),** an additional contribution is observed at 400 nm, confirming the presence of the Re(I) complex. The red shift of the **P1** band in this case is of about 15 nm.

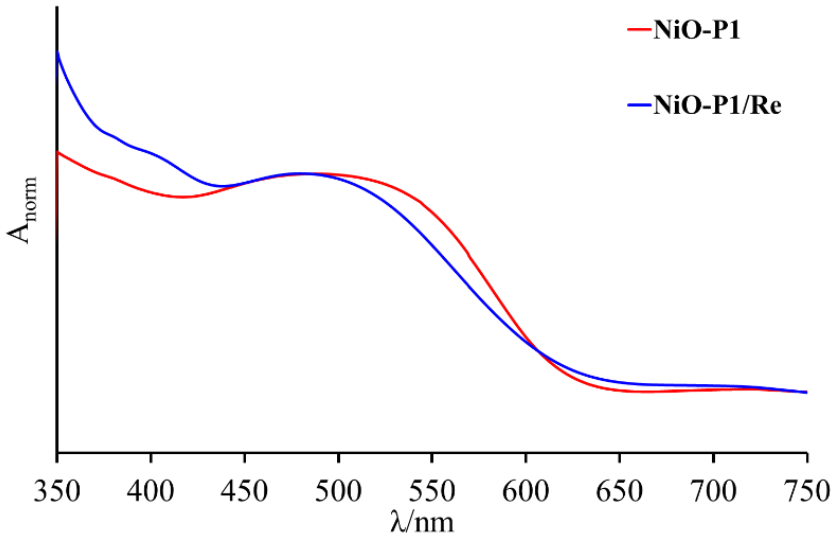

Figure 6.6. *Comparison of normalized absorption spectra in acetonitrile at room temperature of **FTO/NiO-P1/Re(dcb)** (**blue** solid line) and **FTO/NiO-P1** (**red** solid line).*

6.3 Electrochemical characterization of FTO/NiO/Re and FTO/NiO-P1/Re electrodes

The electrodes were studied by cyclic voltammetry in argon and then in CO_2 saturated atmosphere. In a standard experiment, the prepared electrodes were used as working electrode (active surface around 2 cm^2), SCE was used as reference and a Pt grid was used as counter electrode. A 0.1 M aqueous solution of Na_2SO_4 was chosen as supporting electrolyte. The mesoporous FTO/NiO electrode (before the deposition of the photosensitizer and the catalyst) presents an oxidation peak at around +70 mV *vs. SCE* for the oxidation of Ni(II) to Ni(III) and a second oxidation peak at around +660 mV *vs. SCE* for the Ni(III)/Ni(IV) oxidation (see **Figure 6.7**).[7,18] After bubbling CO_2 in the solution, the potentials are shifted at more positive potential because an acidification of the solution takes place (from pH ~ 6.4 to pH ~ 5.3).

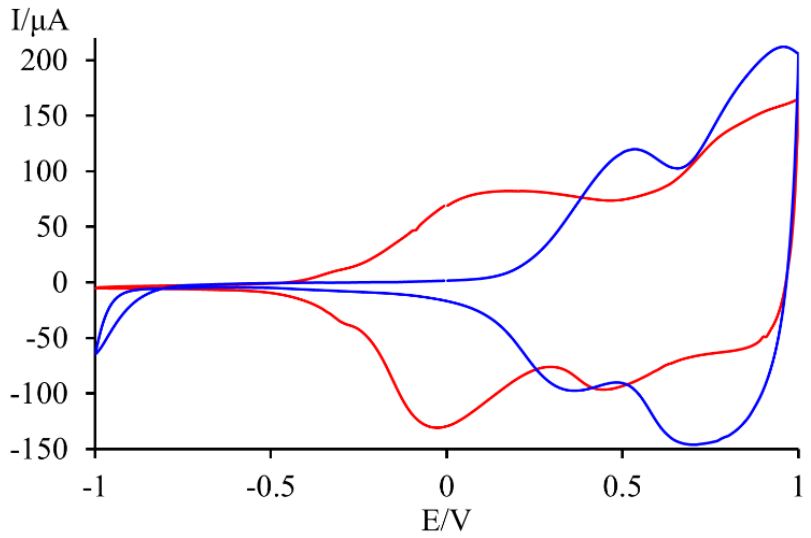

Figure 6.7. *Cyclic voltammetry of **FTO/NiO** electrode in Ar-saturated (**red** solid line) and CO_2-saturated solution (**blue** solid line).*

Figure 6.8 shows the difference in electrochemical response of **FTO/NiO-P1/Re(dcb) (2 drops)** electrodes under Ar *vs.* CO_2 atmosphere, with an increase in cathodic current below -0.7 V *vs. SCE* under CO_2-saturated atmosphere. A

further increase in cathodic current is measured for **FTO/NiO-P1/Re(dcb) (2 drops)** under illumination (see **Figure 6.9**). No photoresponse was observed in the **FTO/NiO** electrode (due to the absence of dye). This means that the photoelectrochemical reduction of CO_2 with the **P1** sensitized electrodes should be facilitated. These observations are consistent with previous works in the French group.

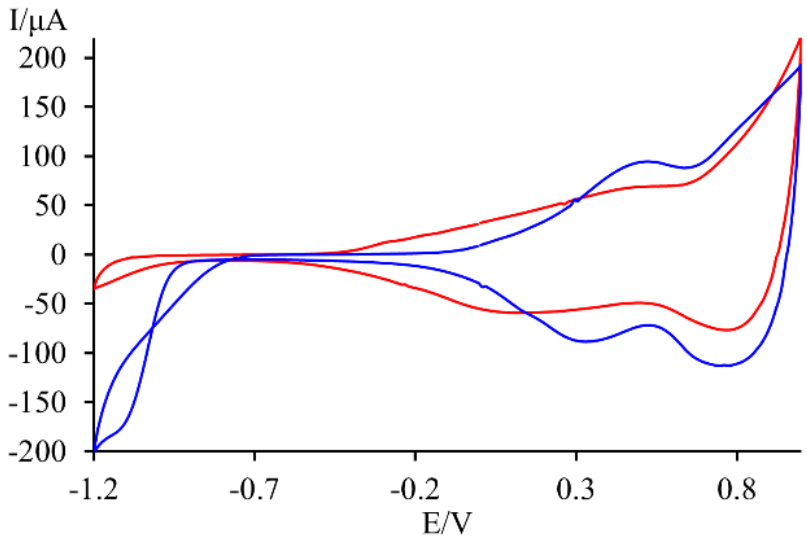

Figure 6.8. *Cyclic voltammetry of **FTO/NiO-P1Re(dcb) (2 drops)** electrode in Ar-saturated (**red** solid line) and CO_2-saturated solution (**blue** solid line).*

Comparison of electrode responses under CO_2 for **FTO/NiO**, **FTO/NiO-P1** and **FTO/NiO-P1/Re(dcb) (2 drops)** showed that the behaviour observed in the dark (**Figure 6.10**) differs from the behaviour observed under illumination (**Figure 6.11**).

In the dark, **FTO/NiO-P1/Re(dcb) (2 drops)** is the most active electrode below -1V (higher cathodic current recorded), while under illumination **FTO/NiO-P1** is the most active. So far, we cannot explain this observation: experiments are in progress to confirm and identify the processes at work (simultaneous potential-dependant GC-monitoring of catalytic products formed during a chronoamperometric experiment).

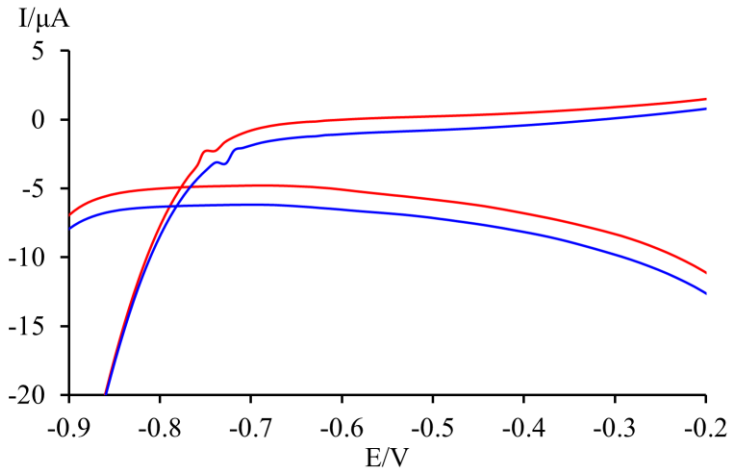

Figure 6.9. *Magnification of cyclic voltammetry of* ***FTO/NiO-P1Re(dcb) (2 drops)*** *electrode in CO_2-saturated solution in the dark (**red** solid line) and upon 0.1 Sun of light (**blue** solid line).*

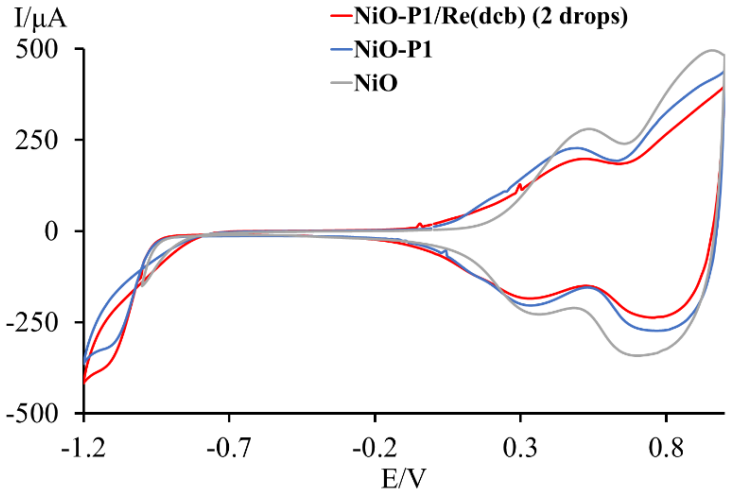

Figure 6.10. *Cyclic voltammetry of* ***FTO/NiO*** *(**grey** solid line),* ***FTO/NiO-P1*** *(**blue** solid line) and* ***FTO/NiO-P1/Re(dcb) (2 drops)*** *(**red** solid line) electrodes in CO_2-saturated solution in the dark.*

From **Figures 6.10** and **6.11**, we can see that the NiO surface is less and less accessible under the successive layers of **P1** dye and Re catalyst, as expected. However, 2 drops of catalyst are a low loading (48 nmol) and, despite the seemingly homogenous film obtained, it is insufficient to passivate the NiO surface. In consequence, **FTO/NiO-P1/Re(dcb)** electrodes with higher loading of Re complex were prepared and 4 drops (96 nmol) gave a complete passivation.

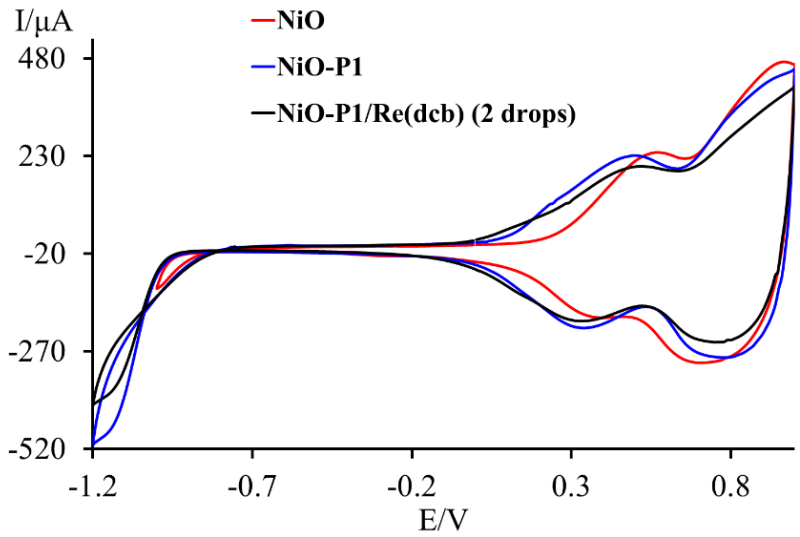

Figure 6.11. *Cyclic voltammetry of **FTO/NiO** (**red** solid line), **FTO/NiO-P1** (**blue** solid line) and **FTO/NiO-P1/Re(dcb) (2 drops)** (**black** solid line) electrodes in CO_2-saturated solution under illumination.*

As evidenced by **Figure 6.12**, the higher loading greatly affects the response of the electrode: no more oxidation processes of Ni centres are seen, while the cathodic photocurrent is significantly anticipated and starts around -0.7 V *vs SCE*. The promising **FTO/NiO-P1/Re(dcb) (4 drops)** electrodes will be further investigated and characterized (in particular, long-standing photocatalytic experiments coupled to GC-MS monitoring).

For comparative purpose and to get better understanding of the role of the Re catalyst in the performances of photoelectrodes assembled, the (photo)electrochemical behaviour of **FTO/Re(dcb)** and **FTO/Re(dmb)** were investigated. After control experiments confirmed the redox characteristics of the molecular complexes,[19] we turned to confirm the redox features of the heterogenized Re complexes. This turned out a difficult task as the deposited films of Re complexes were not stable on FTO (not even Re(dcb), despite its anchoring groups), under the experimental conditions used for cyclic voltammetry. On the other hand, films of Re catalysts deposited on **FTO/NiO** and **FTO/NiO-P1** are rather stable and very stable, respectively. This observation is in favour of such a

design for hybrid electrode materials based on multiple heterogenized molecular components.

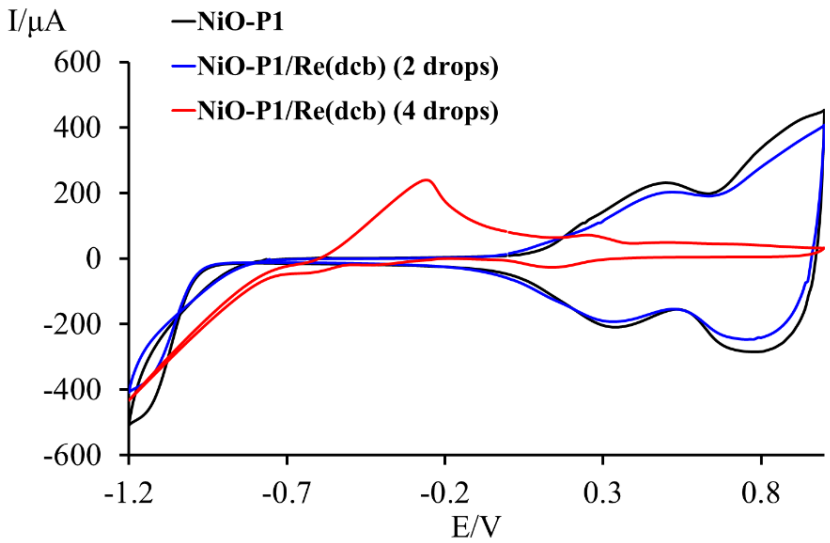

Figure 6.12. *Cyclic voltammetry of **FTO/NiO-P1** (**black** solid line), **FTO/NiO-P1/Re(dcb) (2drops)** (**blue** solid line) and **FTO/NiO-P1/Re(dcb) (4drops)** (**red** solid line) electrodes in CO_2-saturated solution under illumination.*

For comparative purpose and to get a better understanding of the role of the dye in the performances of photoelectrodes assembled, the (photo)electrochemical behaviour of **FTO/NiO-Re(dcb)** was investigated. For the deposition of the Re(I) catalyst on **FTO/NiO,** we first explored the soaking method that is commonly used for the dye loading. Overnight soaking (16 hours) of the **FTO/NiO** electrode in an acetonitrile solution 0.3 mM of **$Re(dcb)(CO)_3Cl$** resulted in a very low catalyst loading (no measurable difference to the response of **FTO/NiO**). For this reason, the deposition by drop cast of 42 nmol of catalyst (2 drops) was chosen instead. **Figure 6.13** shows the difference in electrochemical response for **FTO/NiO-P1, FTO/NiO/Re(dmb)** and **FTO/NiO/Re(dcb)** electrodes under CO_2 and in the dark. Under these conditions, the cathodic current recorded below -0.8V is larger for **FTO/NiO/Re(dmb)** (pink curve).

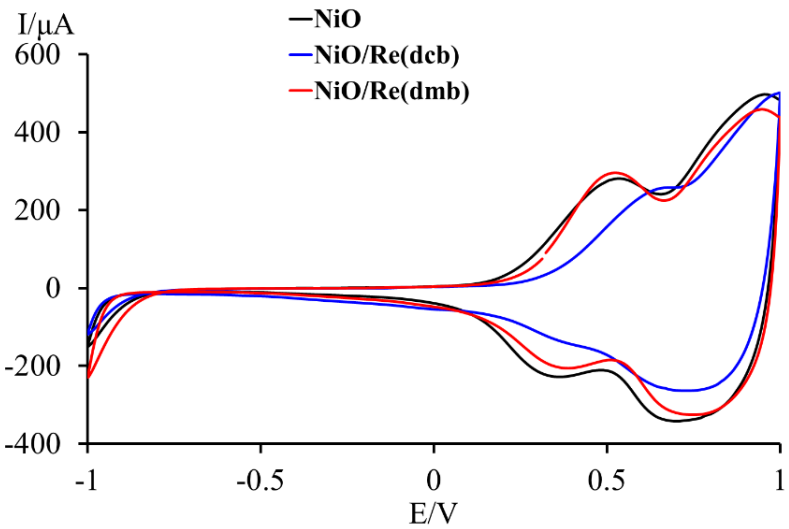

Figure 6.13. *Cyclic voltammetry of **FTO/NiO** (**black** solid line), **FTO/NiO/Re(dcb)** (**blue** solid line) and **FTO/NiO/Re(dmb)** (**red** solid line) electrodes in CO_2-saturated solution under dark.*

However, this range of potentials may correspond to overlapping and competing processes: Hydroden-Evolution Reaction and CO_2 reduction. However, on the potential range [-0.4; -0.8V], of particular interest for the reduction of CO_2, the cathodic current recorded is higher for **FTO/NiO/Re(dcb)** (**blue** curve) in **Figure 6.14**.

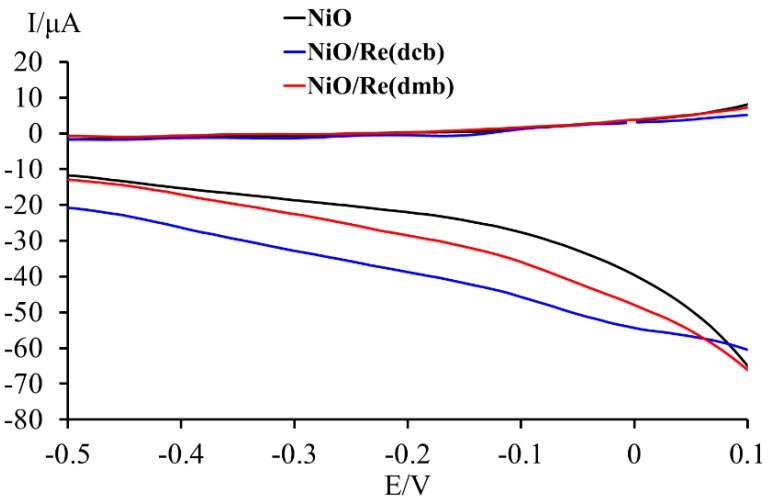

Figure 6.14. *Magnification of cyclic voltammetry of **FTO/NiO** (**black** solid line), **FTO/NiO/Re(dcb)** (**blue** solid line) and **FTO/NiO/Re(dmb)** (**red** solid line) electrodes in CO_2-saturated solution under dark.*

Overall, there are significant differences in the electrochemical responses and catalytic activities of photoelectrodes modified by the **Re(dcb)** or **Re(dmb)** complexes, as could be expected from their different redox properties and homogeneous catalysis. This will be further investigated using GC-MS monitoring.

In order to study the light response of the **FTO/NiO-P1Re(dcb) (2 drops)** photoelectrode on the time scale of the electrochemical setup, a chronoamperometry experiment with chopped illumination was performed (see **Figure 6.15**) and it showed that the transient photocurrent, generated during the on-off illumination cycles, is reproducible and stable.

Longer experiments (several hours) are necessary to confirm the overtime stability of the prepared materials under photocatalytic operating conditions. The relatively low photocurrents obtained need to be put in perspective of the "atom efficiency" approach of heterogenized molecular components and of the low loading of catalyst used here (48 nmol), at 0.1 Sun illumination.

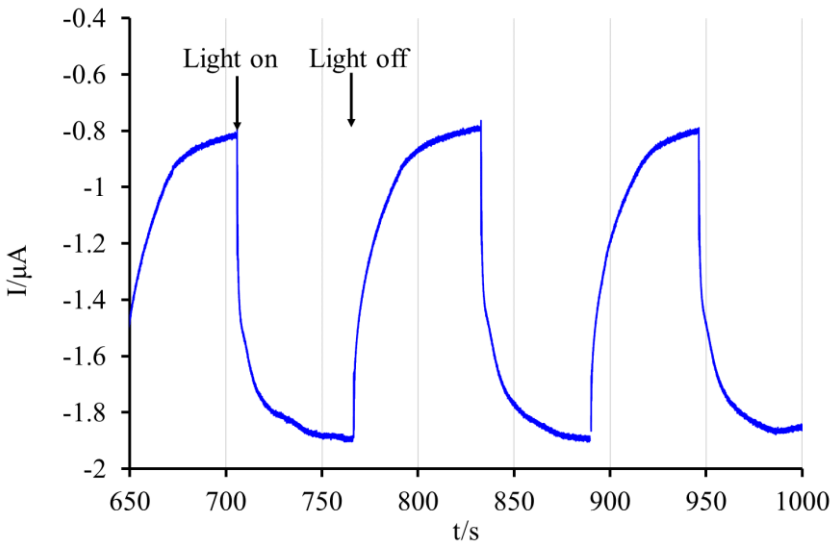

Figure 6.15. *Chronoamperometry of **FTO/NiO-P1Re(dcb)** (2 drops) electrode in CO_2-saturated solution at an applied bias of -0.6V vs. SCE and at 0.1 Sun illumination.*

6.4. Conclusions and Perspectives

Due to COVID outbreak in France, the work was interrupted on March 16th, 2020 and our current results, to be completed in time, are presented here.

The experiments performed so far led to several observations that will require further investigation. The dropcasting method turned out to be an efficient way to prepare the top layer of the catalyst. Light (white LED, 0.1 Sun) affects the electrochemical response of modified photoelectrodes under CO_2. Optimization of catalyst loading is necessary and it significantly changes the activity of the modified photoelectrodes, as observed in previous works.[13] The choice of molecular catalyst to be heterogenized, based on its redox properties in solution, is important and determines the activity of the resulting modified photoelectrode. We will further investigate both **Re(dcb)** and **Re(dmb)** electrodes and compare their catalytic activity, considering the redox and structural differences for these catalysts. Transient photocurrent, generated during the on-off illumination cycles, for modified photoelectrodes is reproducible, stable and its intensity is to be put in the perspective of the low loading of catalyst and of the dim light conditions used. Longer experiments are necessary to confirm the overtime stability of the prepared materials under photocatalytic operating conditions. Further experiments are in progress to confirm and identify the processes at work (simultaneous potential-dependant GC-monitoring of catalytic products formed during a chronoamperometric experiment), toward a rational design of such hybrid 3D electrode materials. As we have seen, integrated components within the 3D assembly are more stable than their simply deposited form onto FTO substrates.

Experiments that are in progress in Paris: (i) to identify and quantify the products of the CO_2 reduction experiment using a combination of (photo)electrochemical and analytical methods (GC-MS); (ii) to quantify the resistivity of the prepared hybrid materials using electrochemical impedance spectroscopy (EIS). Time-resolved spectroscopic characterizations of the most promising modified

photoelectrodes are planned in Messina, in order to get better insights into the key parameters and mechanistic aspects of the photocatalytic activity. The groups will continue this work in close collaboration despite the lasting pandemic situation.

References

1. Y. Yamazaki, H. Takeda, O. Ishitani, *J. Photochem. Photobiol., C*, 2015, **25**, 106−137.
2. A. J. Morris, G. J. Meyer, E. Fujita, *Acc. Chem. Res.*, 2009, **42**, 1983−1994.
3. J. L. White, M. F. Baruch, J. E. Pander, Y. Hu, I. C. Fortmeyer, J. E. Park, T. Zhang, K. Liao, J. Gu, Y. Yan, T. W. Shaw, E. Abelev, A. B. Bocarsly, *Chem. Rev.*, 2015, **115**, 12888–12935.
4. (a) M. K. Brennaman, L. Alibabaei, M. K. Gish, C. J. Dares, D. L. Ashford, R. L. House, G. J. Meyer, J. M. Papanikolas, T. J. Meyer, *J. Am. Chem. Soc.*, 2016, **138**, 13085-13102; (b) B. Zhang, L. Sun, *Chem. Soc. Rev.*, **2019**, 48, 2216-2264 and references therein.
5. J. Li, N. Wu, *Catal. Sci. Technol.*, 2015, **5**, 1360-1384.
6. J. S. DuChene, G. Tagliabue, A. J. Welch, X. Li, W.-H. Cheng, H. A. Atwater, *Nano Lett.*, 2020, **20**(4), 2348–2358.
7. A. Sapi, A. Varga, G. F. Samu, D. Dobo, K. L. Juhasz, B. Takacs, E. Varga, A. Kukovecz, Z. Konya, C. Janaky, *J. Phys. Chem. C*, 2017, **121**, 12148–12158.
8. M. P. Dare-Edwards, J. Goodenough, A. Hamnett, N. D. Nicholson, *J. Chem. Soc., Faraday Trans.*, 1981, **77**, 643–661.
9. C.-Y. Lin, Y.-H. Lai, D. Mersch, E. Reisner, *Chem. Sci.*, 2012, **3**, 3482–3487.
10. A. Bachmeier, S. Hall, S. W. Ragsdale, F. A. Armstrong, *J. Am. Chem. Soc.*, 2014, **136**, 13518−13521.
11. P. Qin, H. Zhu, T. Edvinsson, G. Boschloo, A. Hagfeldt, L. Sun, *J. Am. Chem. Soc.*, 2008, **130**, 8570–8571.
12. J.-M. Lehn, R. Ziessel, *Proc. Natl. Acad. Sci. U.S.A.*, 1982, **79**, 701 - 704.
13. E. Szaniawska, A. Wadas, H. H. Ramanitra, E. A. Fodeke, K. Brzozowska, A. Chevillot-Biraud, M.-P. Santoni, I. A. Rutkowska, M. Jouini, P. J. Kulesza, *RSC Adv.*, 2020, **10**, 31680–31690.

14. P. Ho, L. Q. Bao, R. Cheruku, J. H. Kim, *Electron. Mater. Lett.*, 2016, **12**, 638–644.
15. S. Sumikura, S. Mori, S. Shimizu, H. Usami, E. Suzuki, *J. Photochem. Photobiol., A*, 2008, 199(1), 1–7.
16. K. A. Jantan, J. M. McArdle, L. Mognon, V. Fiorini, L. A. Wilkinson, A. J. P. White, S. Stagni, N. J. Long, J. D. E. T. Wilton-Ely, *New J. Chem.*, 2019, **43**, 3199-3207.
17. P. Qin, J. Wiberg, E. A. Gibson, M. Linder, L. Li, T. Brinck, A. Hagfeldt, B. Albinsson, L. Sun, *J. Phys. Chem. C*, 2010, **114**, 4738–4748.
18. H. Bode, K. Dehmelt, J. J. Witte, *Electrochim. Acta*, 1966, **11**, 1079–1087.
19. J. M. Smieja, C. P. Kubiak, *Inorg. Chem.*, 2010, **49**, 9283–9289.

Chapter 8

Experimental Section

8.1. Materials and Methods

All solvents and reagents were used as received without further purification, unless otherwise stated.

UV-Vis absorption spectra were measured in acetonitrile on a JASCO V-560 UV/VIS spectrophotometer. The luminescence measurements were performed using a SpexJobin Yvon FluoroMax-2 spectrofluorimeter equipped with a photomultiplier Hamamatsu R3896. IR spectra were recorded with a JASCO FT/IR-6600 in MeCN. Emission lifetimes were obtained using a Horiba FluoroCube time-correlated single photon counting system. The excitation light source was a LED pulse lamp (NanoLED, 401 nm). The samples were dissolved in MeCN and purged with Ar for 20 min before lifetime measurements. The emission quantum yields were evaluated using as standard the emission from $[Ru(bpy)_3]Cl_2$ (bpy = 2-2'-bipyridine) in water (Φ_{em} = 0.040).[1]

Electrospray ionization time-of-flight mass spectroscopy (ESI-TOFMS) was undertaken with a Waters LCT Premier, with acetonitrile as mobile phase.

NMR spectra were recorded on a Varian 500 spectrometer operating at 500 MHz for ^{1}H and 125 MHz for ^{13}C. The chemical shifts were reported in parts per million (ppm, δ) using the residual solvent peak as internal standard. The coupling constants (J) were given in hertz.

Whereas for all the organic ligands the NMR spectra are reported, for the metal complexes only the ^{1}H-NMR spectrum of the metal complex **Re(bpy$_2$Ph)** is shown. This because the presence of a number of stereo isomers in the multinuclear metal complexes make the spectra unclear.

Redox potentials were measured in dry and Ar purged acetonitrile solution containing the complex (0.5 mM) and tetrabutylammonium hexafluorophosphate (Bu_4NPF_6, 0.05 M) as supporting electrolyte through CV, DPV and SW using an Autolab multipurpose equipment and a glassy carbon electrode (8 mm^2, Amel) as working electrode, a Pt wire as counter electrode and a silver wire as pseudo-reference electrode. The redox couple ferrocene/ferrocenium (395 mV vs. SCE in acetonitrile) was used as internal reference.

8.2. CO_2 Photoreduction

For the photocatalysis experiments DMA was dried over activated molecular sieves 4 Å, distilled under reduced pressure and stored under argon before use. TEOA was distilled under reduced pressure.

Emission quenching experiments were performed at 25 °C under an Ar atmosphere using a JASCO FP-8600 spectrofluorometer in DMA/TEOA (5:1 v/v) solutions containing the complex and four different concentrations of sacrificial agent. Quenching rate constants k_q were calculated from linear Stern–Volmer plots for the luminescence of the triplet metal-to-ligand-charge-transfer (^{3}MLCT) excited state of the photosensitizer units together with knowledge of their lifetimes. For the TONs determination, 3 mL of DMA/TEOA (5:1 v/v) solution of complex (0.05 mM) and sacrificial agent (0.1 M) in 11 mL (i.d. = 8 mm) Pyrex tubes were purged with CO_2 and irradiated with a Merry-go-round type irradiation apparatus using LED (530 nm, 4 mW) as a light source, Iris-MG (CELL System co.). For the quantum yield determination, 4 mL of DMA/TEOA (5:1 v/v) solution of complex (0.05 mM) and sacrificial agent (0.1 M) in 11 mL quartz cubic cell (optical path length: 1 cm) was purged with CO_2 for 20 min, and then irradiated with a SHIMADZU QYM-01 apparatus with light at 480 nm using a 500-W Xe lamp (Asahi Spectra Co.) with a bandpass filter. The temperature of the solutions was maintained at 25 ± 0.1 °C using an IWAKI

CTS-134A constant-temperature system. H_2 and CO (the gaseous photoreaction products) were quantified with a GC-TCD (GL science GC323) with an active carbon column and argon as gas carrier and the amount of formic acid was analysed by capillary electrophoresis system (Agilent7100L) with buffer solution and water dilution.

8.3. CO_2 PhotoElctroreduction

All commercially available chemicals were purchased and used as received. Dye **P1** was purchased from Dyenamo. FTO substrate (15 ohm/sq) was purchased from Solaronix.

Electrochemical measurements (cyclic voltammetry, chronoamperometry experiments) were performed with a potentiostat from Bio-Logic SAS (VSP and SP-150), in a 3-electrodes setup with aqueous solution of Na_2SO_4 0.1M as electrolyte: a Pt grid as the counter electrode, SCE (3.5 M KCl) as the reference electrode and the working electrode being the modified (photo)electrode FTO/NiO (the actual active area is measured for each sample, in order to determine the measured current density).

pH was measured using a combined glass electrode connected to a pH-meter CyberScan pH 510 (Eutech Instruments): for fresh Na_2SO_4 electrolyte, pH = 7.0 after bubbling with Ar and pH = 5.0 after bubbling with CO_2.

UV-visible absorption spectra of thin films were performed on a Cary 4000 spectrophotometer.

The emission spectra were recorded with a Jobin Yvon HORIBA Fluorolog-3 spectrofluorometer.

8.3.1 Modified (photo)electrode fabrication

FTO/NiO photoelectrodes were prepared on FTO step-by-step. FTO glass (3.8 x 3.8 cm) was sonicated in water milli-Q and soap for 15 minutes, in water milli-Q for 15 minutes and in ethanol for 15 minutes. After that, a thermic

treatment was performed with a microprocessor controller ramp controller GESTIGKEITE PROGRAMMER PR5. The blocking layer was prepared by following the reported procedure:[2] 200 µL of a solution of nickel acetate tetrahydrate (0.5 M) in ethanol 96% v/v was deposed by spin coating (3000 rpm for 30 sec) on the FTO glass. This glass was sintered using the following temperature program: the electrode was left at 240°C for 10 minutes (in order to dehydrate the complex), after that the temperature was increased until 330°C and left for 10 minute (to convert the nickel acetate in $NiCO_3$); third step: the electrode was left at 375°C for 10 minute and at 390°C for the decomposition of the carbonate in order to form a compact blocking layer. The electrode was left at 450°C for 30 minutes. This procedure was performed twice in order to obtain two compact blocking layers and to improve the compactness of the layer. Deposition of mesoporous NiO layer was performed using a Ni(II) precursor by "Doctor Blade" method followed by calcination at 450°C.

The electrode FTO/NiO-P1 and FTO/NiO/Re(dcb) were prepared by soaking. The NiO electrodes were warmed up until 200°C and left at this temperature for 10 minutes. When the temperature decreased until 70°C the electrodes were soaked in an ethanol solution 0.3 mM of P1 or an acetonitrile solution 0.3 mM of Re(dcb) for 16 hours. After this time, the electrodes were washed with acetonitrile and dried on air. The electrodes of FTO/NiO-P1/Re(dcb) were prepared by dropcast of an acetonitrile solution 0.3 mM of Re(dcb) on the previously prepared FTO/NiO-P1 electrodes. The FTO/NiO-P1 electrodes were warmed at 65°C and left at this temperature for 15 minutes. After this period 70 µL of an acetonitrile solution 0.3 mM of Re(dcb) was deposited on the electrode surface and dried at 65°C for 5 minutes. This passage was repeated twice for the 2 drops electrodes and four time for the 4 drops electrodes. The same procedure was employed for the FTO/NiO/Re(dmb) electrodes.

8.4. Syntheses

8.4.1 Syntheses of the Bridging Ligands

Synthesis of bpy$_2$Ph

4,4′-Dimethyl-2,2′-dipyridyl (1.88 g, 10 mmol) was dissolved in 140 mL of dry THF under argon atmosphere. The solution was cooled at -33°C and a solution 1M of lithium diisopropylamide (12 mmol, 12 mL) was added dropwise. After stirring for 90 min, 50 mL of a solution of 1,4-Bis(bromomethyl)benzene (1,09g, 4.1 mmol) was added dropwise. The solution was left stirring for 48h. After, the reaction was quenched adding 20 mL of water. The mixture was extracted with diethyl ether (3 x 250 mL) and dichloromethane (2 x 100 mL). The organic phase was dried over sodium sulphate anhydrous. The pale pink residue was recrystallized from ethanol giving the pure white solid. Yield: 1.00g, 52%.

^{1}H NMR (500 MHz, 25°C, CD_2Cl_2) δ = 8.51 (t br, 4H), 8.31-8.28 (d, 4H), 7.14 (m, 6H), 7.11 (d, 2H), 2.99 (s, 8H), 2.45 (s, 6H). ^{13}C NMR (126 MHz, 25°C, CD_2Cl_2) δ = 156.08, 155.88, 151.55, 148.88, 148.77, 148.05, 138.88, 128.41, 124.56, 123.87, 121.64, 120.95, 37.32, 36.19, 20.86.

Synthesis of bpy$_3$Ph

4,4′-Dimethyl-2,2′-dipyridyl (1.83 g, 10 mmol) was dissolved in 140 mL of dry THF under argon atmosphere. The solution was cooled at -33°C and a solution 1M of lithium diisopropylamide (12 mmol, 12 mL) was added dropwise. After stirring for 90 min, 38 mL of a solution of 1,3,5-Tris(bromomethyl)benzene (1g, 2.8 mmol) was added dropwise to the mixture. The solution was left stirring for 48h. After this period, the reaction was quenched adding 15 mL of water. The mixture was extracted with diethyl ether (3 x 250 mL) and dichloromethane (2 x 100 mL). The organic phase was dried over sodium sulphate anhydrous. The yellow residue was purified by chromatography on a silica column eluted with DCM/Methanol (9:1). Yield: 1.08g, 57%.

^{1}H NMR (500 MHz, 25°C, CD_2Cl_2) δ = 8.53 (d, J = 4.9 Hz, 6H), 8.28-8.25 (m, 6H), 7.14-7.11 (m, 3H), 7.06 (dd, J = 4.9, 1.7 Hz, 3H), 6.80 (s, 3H), 2.87 (s, 12H), 2.36 (s, 9H). ^{13}C NMR (126 MHz, 25°C, CD_2Cl_2) δ = 156.16, 156.01, 151.65, 148.99, 148.89, 148.14, 141.38, 126.63, 124.66, 124.63, 124.03, 121.80, 121.18, 37.45, 36.68, 21.01. ^{1}H{^{13}C} HQSC δ = {8.53, 149.00}, {8.53, 148.91}, {7.14-7.11, 124.65}, {7.06, 124.05}, {6.80, 126.65}, {8.28-8.25, 121.82}, { 8.28-8.25, 121.19}, {2.87, 37.46}, {2.87, 36.69}, {2.36, 21.02}.

Anal. Calcd for $C_{45}H_{42}N_6$: C, 81.05; H, 6.35; N, 12.60. Found: C, 81.09; H, 6.40; N, 12.58.

Synthesis of bpy$_4$Ph

4,4′-Dimethyl-2,2′-dipyridyl (1.81 g, 9.1 mmol) was dissolved in 140 mL of dry THF under argon atmosphere. The solution was cooled at -28°C and a solution 1M of lithium diisopropylamide (12 mmol, 12 mL) was added dropwise. After stirring for 90 min, 32 mL of a solution of 1,2,4,5-Tetra(bromomethyl)benzene (0.99g, 2.2 mmol) was added dropwise. The solution was left stirring overnight for 48h. After this period, the reaction was quenched adding 15 mL of water. The mixture was extracted with diethyl ether (3 x 250 mL) and dichloromethane (2 x 100 mL). The organic phase was dried over sodium sulphate anhydrous. The yellow residue was purified by chromatography on a silica column eluted with DCM/Methanol (9:1). Yield: 1.17g, 59%.

^{1}H NMR (500 MHz, 25°C, CD_2Cl_2) δ = 8.47-8.50 (m, 8H), 8.28 (d, 4H), 8.26 (dd, 4H), 7.11-7.13 (m, 4H), 7.07-7.06 (dd, 4H), 6.94 (s, 2H), 2.91 (m, 16H), 2.41 (s, 12H). ^{13}C NMR (126 MHz, 25°C, CD_2Cl_2) δ = 156.10, 155.85, 151.51, 148.94, 148.78, 148.01, 136.70, 130.54, 124.56, 123.90, 121.70, 121.06, 36.96, 33.04, 20.90.

8.4.2 Syntheses of the Photosensitizer Moieties

Synthesis of Cis-[Ru(dmb)$_2$Cl$_2$] ·2H$_2$O^3

4,4′-Dimethyl-2,2′-dipyridyl (2.81 g, 15 mmol), $RuCl_3 \cdot 3H_2O$ (2.06 g, 8 mmol) e LiCl (1 g, 24 mmol) were dissolved in 14 mL of DMF. This mixture was refluxed for 15 h. After this time the solution was cooled to room temperature and 65 mL of acetone was added. The mixture was left at 0°C overnight. The formed purple solid was collected by filtration. Yield: 2.02 g, 45%.

Synthesis of Ru(bpy$_2$Ph)

The ligand **bpy$_2$Ph** (200 mg, 0.42 mmol) was dissolved in 25 mL of a mixture 1,2-dichloroethane/ethanol (1:1 v/v) under argon atmosphere. Cis-$[Ru(dmb)_2Cl_2] \cdot 2H_2O$ (65 mg, 0.12 mmol) was dissolved in 10 mL of the same solvent mixture and added dropwise slowly to the reaction mixture at reflux temperature. The solution was left at reflux temperature for 2 h. The crude was dissolved in distilled water and the unreacted ligand was filtered out. The product was obtained as orange solid by adding NH_4PF_6 and washed with water. Yield: 128 mg, 86.7%.

Synthesis of Ru(bpy$_3$Ph)

The ligand **bpy$_3$Ph** (101 mg, 0.15 mmol) was dissolved in 5 mL methanol under argon atmosphere. Cis-$[Ru(dmb)_2Cl_2] \cdot 2H_2O$ (78 mg, 0.13 mmol) was dissolved in 5 mL of ethanol and added dropwise to the mixture during 60 min at reflux temperature. The solution was left at reflux temperature under stirring for 24 h. The residue was purified by ion exchange chromatography on CM Sephadex C-25 eluted with a 0.05 M solution of NaCl in water/acetone (5:3, v/v). Yield: 70 mg, 46%. ESI-TOFMS (in MeCN) m/z: Calculated for $C_{69}N_{10}H_{64}Ru$ (M – 2 PF6) 568.2267, found 568.2239.

Synthesis of $Ru_2(bpy_3Ph)$

The ligand **bpy_3Ph** (101 mg, 0.15 mmol) was dissolved in 5 mL methanol under argon atmosphere. Cis-$[Ru(dmb)_2Cl_2] \cdot 2H_2O$ (180 mg, 0.31 mmol) was dissolved in 5 mL of ethanol and added dropwise to the reaction mixture over 80 min at reflux temperature. The solution was left under stirring at reflux temperature for 24 h. The residue was purified by ion exchange chromatography on CM Sephadex C-25 eluted with a solution of NaCl in water/acetone (5:3, v/v). The 0.05 M solution of NaCl led to the elution of the mononuclear bi-charged complex. Increasing the concentration of NaCl up to 0.1 M resulted in the selective elution of the required binuclear tetra-charged complex. The product was precipitated from the concentrate by addition of NH_4PF_6 and filtered out. Yield: 220.9 mg, 67%. ESI-TOFMS (in MeCN) m/z: Calculated for $C_{93}N_{14}H_{86}Ru_2$ (M – 4 PF_6) 401.6400, found 401.6376.

Synthesis of $Ru_3(bpy_3Ph)$

The ligand **bpy_3Ph** (101 mg, 0.15 mmol) was dissolved in 5 mL methanol under argon atmosphere. Cis-$[Ru(dmb)_2Cl_2] \cdot 2H_2O$ (260 mg, 0.45 mmol) was dissolved in 5 mL of ethanol and added dropwise to the mixture during 60 min at reflux temperature. The solution was left at reflux temperature for 24 h. The residue was purified by ion exchange chromatography on CM Sephadex C-25 eluted with a solution of NaCl 0.5 M in water/acetone (5:3, v/v). The concentration of NaCl was gradually increased until 0.15 M. The product was precipitated from the concentrate by addition of NH_4PF_6 and filtered out. Yield: 334.4 mg, 75%. ESI-TOFMS (in MeCN) m/z: Calculated for $C_{117}N_{18}H_{108}Ru_3$ (M – 6 PF_6) 345.9444, found 345.9446.

Synthesis of $Ru_3(bpy_4Ph)$

The ligand **bpy_4Ph** (106 mg, 0.12 mmol) was dissolved in 10 mL ethanol, under argon atmosphere. Cis-$[Ru(dmb)_2Cl_2] \cdot 2H_2O$ (210 mg, 0.36 mmol) was dissolved in 10 mL of methanol and added dropwise slowly to the reaction

mixture at reflux. The solution was left under stirring at reflux temperature for 24 h. The residue was purified by ion exchange chromatography on CM Sephadex C-25 eluted with a solution of NaCl (0.05 M) in water/acetone (5:3, v/v). The starting concentration of NaCl in the eluent permitted the elution of the bi-charged species (**RuL4**). Increasing gradually NaCl concentration (0.1 M, 0.15 M and 0.2 M) gave the possibility to isolate the tree other Ruthenium complexes (respectively with four, six and eight positive charge). The required complex was eluted with a 0.15 M NaCl solution. The product was precipitated from the concentrate by addition of NH_4PF_6 and filtered out. Yield: 219.4 mg, 58%. ESI-TOFMS (in MeCN) m/z: Calculated for $C_{130}N_{20}H_{120}Ru_3$ (M – 6 PF_6) 378.7945, found 378.7920.

8.4.3 Syntheses of the Final Integrated Photosensitizer(s)-Catalyst(s) Complexes

Synthesis of RuRe

RuL2 (38 mg, 0.037 mmol) was dissolved in 18 mL of a mixture of 1,2-dichloroethane and toluene (1:1 v/v) and refluxed under argon atmosphere. **$Re(CO)_5Cl$** (24 mg, 0.066 mmol) was dissolved in 5 mL of the same solvent and the solution was stirred for 4 h at reflux under argon atmosphere. After this period, the product was evaporated under vacuum. The crude was dissolved in ethanol and precipitated by addition of NH_4PF_6, filtered out and washed with diethyl ether. Yield: 46 mg, 80.8%.

Synthesis of RuRe2

RuL3 (20 mg, 0.017 mmol) and **$Re(CO)_5Cl$** (12.7 mg, 0.035 mmol) were dissolved in 32 mL of 1,2-dichloroethane for 4 h at reflux under argon atmosphere. After this period, the product was precipitated by addition of NH_4PF_6 and filtered out. Yield: 33.1 mg, 94%. ESI-TOFMS (in MeCN) m/z: Calculated for $C_{75}N_{10}H_{64}Cl_2O_6RuRe_2$ (M – 2 PF_6) 874.1349, found 874.1372. FT-IR (in CH_3CN) ν_{CO}/cm^{-1}: 2021, 1915, 1896.

Synthesis of Ru2Re

Ru2L3 (50.6 mg, 0.023 mmol) and **$Re(CO)_5Cl$** (8.9 mg, 0.025 mmol) were dissolved in 30 mL of 1,2-dichloroethane for 6 h at reflux under argon atmosphere. The product was dissolved in ethanol, precipitated by addition of NH_4PF_6 and filtered out. Yield: 34.5 mg, 61%. ESI-TOFMS (in MeCN) m/z: Calculated for $C_{96}N_{14}H_{86}ClO_3Ru_2Re$ (M – 4 PF_6) 478.1170, found 478.1149. FT-IR (in CH_3CN) ν_{CO}/cm^{-1}: 2021, 1915, 1895.

Synthesis of Ru3Re

Ru3L4 (35.2 mg, 0.014 mmol) and **$Re(CO)_5Cl$** (7.00 mg, 0.019 mmol) were dissolved in 30 mL of 1,2-dichloroethane for 24 h at reflux under argon atmosphere. The product was dissolved in ethanol, precipitated by addition of NH_4PF_6 and filtered out. Yield: 15.4 mg, 32%.

Synthesis of $[Ru(CO)_2Cl_2]_n$ [4]

Paraformaldehyde (250 mg) and $RuCl_3 \cdot 3H_2O$ (520 mg, 2 mmol) were dissolved in 15 mL of 90% formic acid under Ar atmosphere at reflux temperature for 4 days. The solution changed colour from red to green during the first hour of reflux. Further heating resulted in a change of colour from green to orange to pale yellow. The solution was cooled to room temperature and after stored at 4°C for 24 h. The crude was evaporated to dryness and the residue triturated with hexane. Yield: 320 mg, 71%.

Synthesis of Ru2Ru

Ru2L3 (49.9 mg, 0.023 mmol) and **$[Ru(CO)_2Cl_2]_n$** (7.6 mg, 0.033 mmol) were dissolved in 5 mL of MeOH/acetone (1:1, v/v) and was left at reflux under vigorous stirring for 7 h. The product was reprecipitated in diethyl ether and filtered out. The required product was obtained as an orange precipitate. Yield:

48.6 mg, 87%. $C_{95}N_{14}H_{86}Cl_2O_2Ru_3$ (M – 4 PF_6) 458.5979, found 459.5941. FT-IR (in CH_3CN) ν_{CO}/cm^{-1}: 2070, 2110, 2145, 2172.

Synthesis of Ru3Ru

Ru3L4 (51.0 mg, 0.016 mmol) and **$[Ru(CO)_2Cl_2]_n$** (7 mg, 0.031 mmol) were dissolved in 5 mL of MeOH/acetone (1:1, v/v) and was left at reflux temperature under vigorous stirring for 24 h. The product was reprecipitated in diethyl ether and filtered out. The required product was obtained as an orange precipitate. Yield: 42.7 mg, 78%. $C_{132}N_{20}H_{120}Cl_2O_2Ru_4$ (M – 6 PF_6) 416.7664, found 416.7645. FT-IR (in CH_3CN) ν_{CO}/cm^{-1}: 2063, 1997.

8.4.4 Syntheses of the Final Integrated dendrimer Photosensitizer(s)-Catalyst(s) Complexes

Synthesis of $[Ru(bpy2Ph)_3]^{2+}(PF_6^-)_2$

Bpy_2Ph (197 mg, 0.42 mmol) was dissolved in 20 mL of a deoxygenate 1,2-DCE/EtOH (3:1, v/v) mixture. **Ru(DMSO)4Cl2** (67 mg, 0.14 mmol) was solubilized in 15 mL of the same solvent mixture and added dropwise to the bpy_2Ph solution in 2 hours. The solution was refluxed under argon atmosphere for 26 h. The crude was purified by size exclusion chromatography using Sephadex LH-20 as stationary phase and ethanol as eluent. The final product was precipitate with NH_4PF_6 yielding the final orange solid. Yield: 50.4 mg, 20%.

Synthesis of RuRe3

$Ru(bpy_2Ph)_3$ (20 mg, 0.013 mmol) and **$Re(CO)_5Cl$** (25.8 mg, 0.071 mmol) were dissolved in 15 mL of a deoxygenate 1,2-DCE/toluene (1:1, v/v) mixture. The solution was refluxed under argon atmosphere for 24 h. The final product was precipitate with NH_4PF_6, filtered out and washed with ethanol and diethyl ether yielding the final orange solid. Yield: 25.2 mg, 71%.

Synthesis of [Ru(bpy3Ph)$_3$]$^{2+}$(PF$_6^-$)$_2$

Bpy$_3$Ph (210 mg, 0.29 mmol) was dissolved in 15 mL of a deoxygenate EtOH/H_2O (50:1 v/v) mixture. **Ru(DMSO)$_4$Cl$_2$** (39.4 mg, 0.081 mmol) was solubilized in 15 mL of the same solvent mixture and added dropwise to the **bpy$_3$Ph** solution in 2 hours. The solution was refluxed under argon atmosphere for 6 h. The crude was purified by chromatographic column using Sephadex LH-20 as stationary phase and ethanol as eluent. The first eluted band was purified by chromatography column using alumina as stationary phase and a DCM/EtOH (9:1 v/v) solution as eluent. The final product was precipitated with NH_4PF_6 yielding the final orange solid. Yield: 28.7 mg, 15%.

Synthesis of RuRe6

Ru(bpy3Ph)$_3$ (28 mg, 0.012 mmol) and **Re(CO)$_5$Cl** (40.1 mg, 0.11 mmol) were dissolved in 15 mL of a deoxygenate 1,2-DCE/toluene (1:1, v/v) mixture. The solution was refluxed under argon atmosphere for 24 h. The final product was precipitate with NH_4PF_6 and washed with ethanol and diethyl ether yielding the final orange solid. Yield: 30.9 mg, 61%.

Synthesis of Re(bpy2Ph)

Bpy$_2$Ph (154 mg, 0.33 mmol) was dissolved in 120 mL of deoxygenate toluene. **Re(CO)$_5$Cl** (44.8 mg, 0.12 mmol) was solubilized in 30 mL of methanol and added dropwise to the **bpy$_2$Ph** solution in 4 hours. The solution was refluxed under argon atmosphere for 7 h. The crude was dried under reduced pressure and the product was extracted with acetonitrile (3 x 50 mL). The product was solubilized in chloroform, precipitated in hexane, filtered and washed with diethyl ether yielding the final yellow solid. Yield: 60.5 mg, 65%. δ = 8.80 (d, 2H), 8.49 (t, 2H), 8.23 (t, 4H), 7.40 (dd, 2H), 7.17 (m, 6H), 3.09 (m, 2H), 2.97 (m, 6H), 2,53 (s, 3H), 2.42 (s, 3H).

Synthesis of RuRe3

Re(bpy$_2$Ph) (40 mg, 0.051 mmol) and **Ru(DMSO)$_4$Cl$_2$** (8.3 mg, 0.017 mmol) were dissolved in 15 mL of a deoxygenate 1,2-DCE/toluene (1:1, v/v) mixture. The solution was refluxed under argon atmosphere for 24 h. The final product was precipitated with NH_4PF_6, filtered and washed with ethanol and diethyl ether yielding the final orange solid. Yield: 41.6 mg, 90%.

Synthesis of Re$_2$(bpy$_3$Ph)

Bpy$_3$Ph (250 mg, 0.37 mmol) was dissolved in 120 mL of deoxygenate toluene. **Re(CO)$_5$Cl** (202.5 mg, 0.57 mmol) was solubilized in 50 mL of methanol and added dropwise to the **bpy$_3$Ph** solution in 4 hours. The solution was refluxed under argon atmosphere for 7 h. The crude was purified by chromatographic column using Sephadex LH-20 as stationary phase and EtOH/DCM (9:1 v/v) as eluent. The product was precipitated in diethyl ether and filtered, yielding a yellow solid. Yield: 214.8 mg, 60%.

Synthesis of RuRe6

Re$_2$(bpy$_3$Ph) (60 mg, 0.047 mmol) and **Ru(DMSO)$_4$Cl$_2$** (7.3 mg, 0.016 mmol) were dissolved in 20 mL of a deoxygenate 1,2-DCE/EtOH (1:1, v/v) mixture. The solution was refluxed under argon atmosphere for 24 h. The final product was precipitated with NH_4PF_6, filtered and washed with ethanol and diethyl ether, yielding the final orange solid. Yield: 57.5 mg, 85%.

8.4.5 Syntheses Catalysts Complexes

Synthesis of Re(4,4'-Dimethyl-2,2'-dipyridyl)(CO)$_3$Cl

Re(CO)$_5$Cl (167.4 mg, 0.46 mmol) was dissolved in 25 mL of hot toluene. 4,4′-Dimethyl-2,2′-dipyridyl (90 mg, 0.49 mmol) was added and the reaction was stirred at reflux for 90 minutes. During this period, the solution became yellow in 15 minutes and the product precipitated after 30 minutes of reflux. After

reaching room temperature, the solution was left in the freezer overnight. The product was filtered out and washed with toluene. The product was obtained as a yellow solid. Yield: 201 mg, 89%. ^{1}H NMR (400 MHz, 25°C, d_6-DMSO) δ = 8.82 (d, 2H), 8.62 (s, 2H), 7.58 (d, 2H), 2.55 (s, 6H). FT-IR (in KBr) ν_{CO}/cm^{-1}: 2020, 1940, 1870.

Synthesis of Re(4,4'-dicarboxyl-2,2'-dipyridyl)(CO)$_3$Cl

Re(CO)$_5$Cl (161.1 mg, 0.45 mmol) was dissolved in 56 mL of a hot solution of methanol/toluene (1:2.5, v/v). 4,4′- dicarboxyl-2,2′-dipyridyl (109.5 mg, 0.45 mmol) was added and the reaction was stirred at reflux for 1 hour. During this period, the solution became yellow in 15 minutes and, later, turned orange. The solution was left in the freezer for 1 hour. The reaction mixture was filtered out and the resulting solution was evaporated under vacuum. The product was obtained as an orange solid. Yield: 170 mg, 69%. ^{1}H NMR (400 MHz, 25°C, DMSO) δ = 14.48 (s(br), 2H), 9.22 (d, 2H), 9.01 (s, 2H), 8.14 (d, 2H). FT-IR (in KBr) ν_{CO}/cm^{-1}: 2030, 1930, 1900, 1735.

8.4.6 Syntheses of the Sacrificial Agents

Synthesis of 1-Benzyl-1,4-dihydronicotinamide (BNAH)

The chloride salt of 1-benzylnicotinamide ($BNA^{+}Cl$)[5] (20.1g, 0.08 mol) and Na_2CO_3 (28g, 0.27 mol) were solubilized in 250 mL of water and left stirring and bubbling with N_2. After 30 minutes, $Na_2S_2O_4$ (50g, 0.29 mol) was added and the solution immediately turned orange-yellow. The solution was left stirring and bubbling N_2 in the dark for 24h. The residue yellow precipitate was filtrated and recrystallized tree times from hot ethanol. Yield: 4 g, 23%.

^{1}H NMR (400 MHz, 25°C, CD_3Cl) δ = 7.36-7.30 (m, 5H), 7.20 (s, 1H), 5.75 (dd, 1H), 5.32 (s, 2H), 4.75 (m, 1H), 4.29 (s, 2H), 3.17 (s, 2H).

Synthesis of 1,3-Dimethyl-2-Phenyl-2,3-dihydro1H-benzo[d]imidazole (BIH)

Pyridine (120 mL), p-toluenesulfonil chloride (40.4 g, 0.21 mol) and o-phenylenediamine (11 g, 0.11 mol) were stirred at room temperature for 6 h. The solution became immediately dark red and after 6 h pink. An aqueous solution of HCl (15%, 130 mL) was added to give white precipitate. These solid was collected, suspended in ethanol and refluxed for 3.5 h. The solution was left at 0°C overnight. The white precipitate (N,N'-di(*p*-toluenesulfonyl)-*o*-phenylenediamine) was collected by filtration and dried under vacuum. Yield: 40.3 g, 97%.

N,N'-di(*p*-toluenesulfonyl)-*o*-phenylenediamine (40 g, 0.1 mol) and K_2CO_3 (50.2 g, 0.38 mol) were dissolved in 450 mL of acetonitrile. The solution was left stirring at room temperature for 1 h. Methyl iodide (15 mL, 0.24 mol) was added under stirring and in an ice bath. After that, the solution was left at reflux overnight. The solution was evaporated and extracted with water and dichloromethane (3 x 250 mL) and dried with Na_2SO_4. The solid was recrystalized from hot ethanol in order to give white crystals (N-N'-dimethyl-N,N'-di(*p*-toluenesulfonyl)-*o*-phenylenediamine) and dried under vacuum. Yield: 38 g, 90%.

N-N'-dimethyl-N,N'-di(*p*-toluenesulfonyl)-*o*-phenylenediamine (19 g, 0.04 mol) and H_2SO_4 (96%, 20 mL) were heated at 85°C for 4 h. Then the solution was cooled at room temperature and diluted with 200 mL of water. NaOH 10 M was added to make the solution basic. The mixture was extracted with diethyl ether (3 x 200 mL). The organic phase was evaporated and N-N'-dimethyl-*o*-phenylenediamine was obtained as brown oil. Minimum amount of MeOH was added to dissolve the oil and benzaldehyde (5 mL, 0.05 mol) was added and stirred at room temperature. One drop of acetic acid was added to give a white precipitate. The crude was recrystallized twice from hot ethanol to give pure BIH. Yield: 7.8 g, 87%.

^{1}H NMR (400 MHz, 25°C, CD_3Cl) δ = 7.59-7.76 (m, 2H, Ph-*o*), 7.42-7.40 (m, 3H, Ph-*m*,*p*), 6.72 (dd, J = 4.8, 3.2, 2H, 4-H), 6.44 (dd, J = 4.8, 3.2, 2H, 5-H), 4.88 (m, 1H, 2-H), 2.57 (s, 6H, -CH_3).

8.5 NMR Characterization

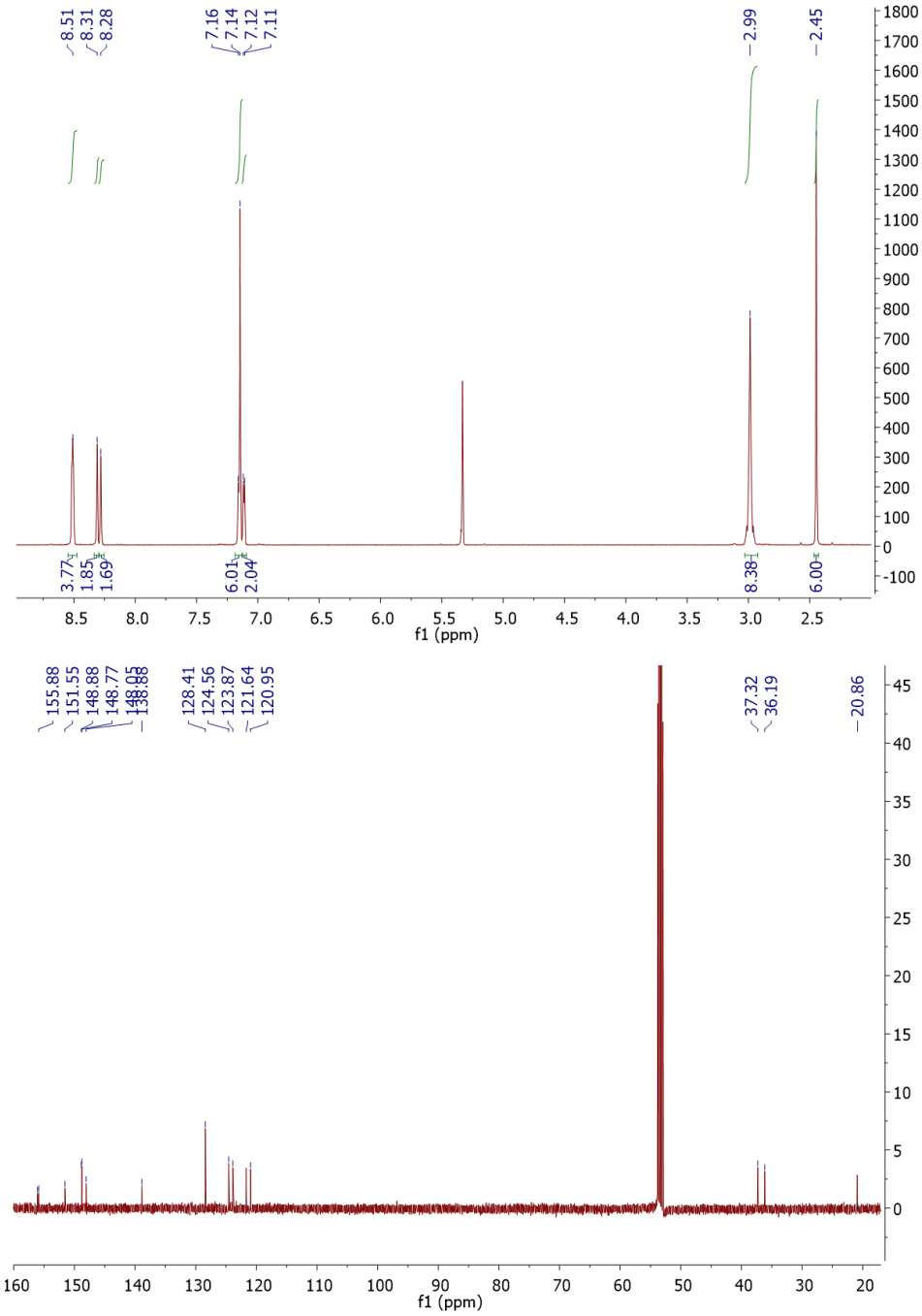

Figure 8.1. *^{1}H-NMR spectrum (top panel) and ^{13}C-NMR spectrum (bottom panel) of* ***bpy$_2$Ph*** *in CD_2Cl_2.*

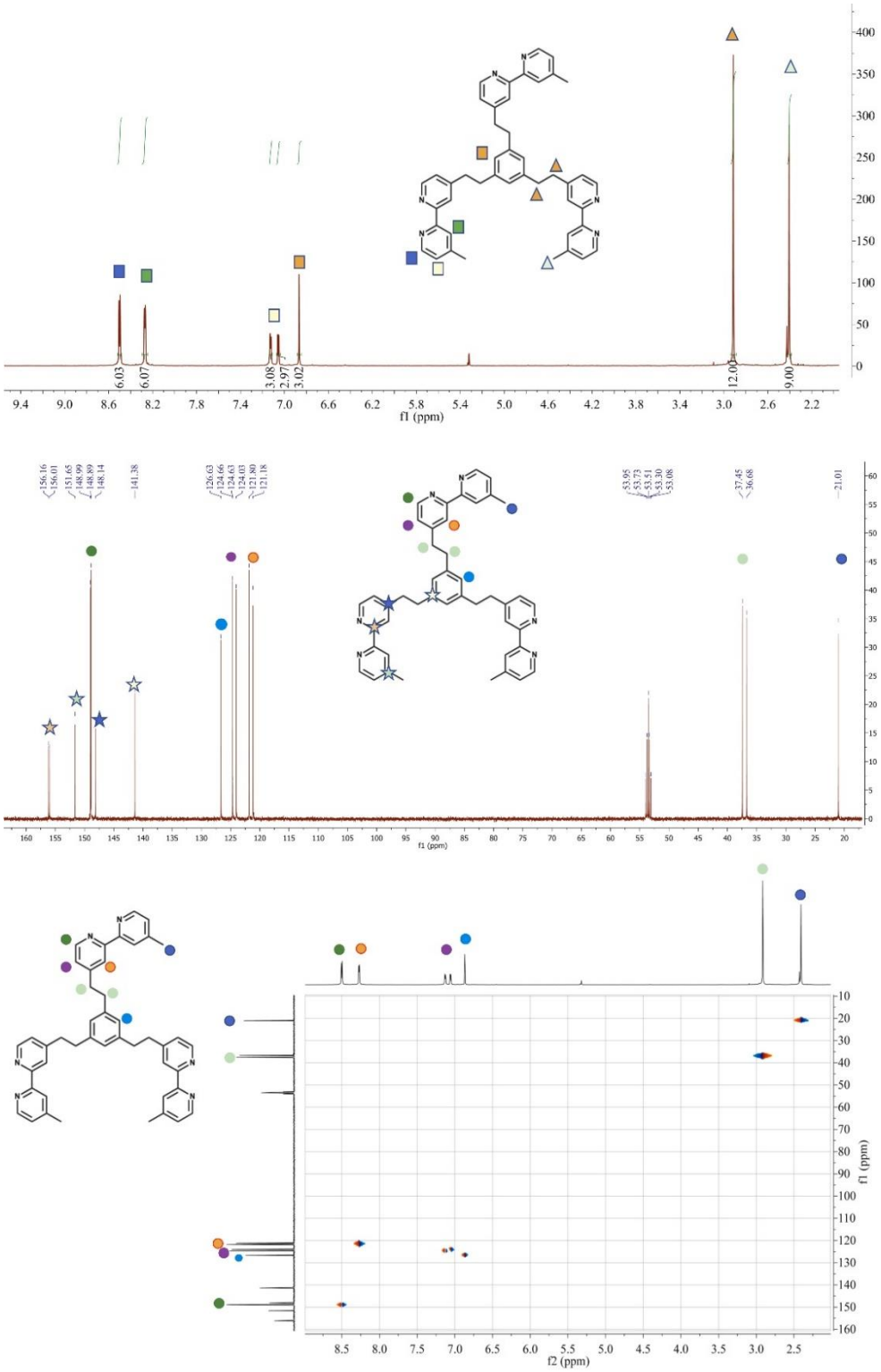

Figure 8.2. *^{1}H-NMR spectrum (top panel); ^{13}C-NMR spectrum (middle panel) and ^{1}H–^{13}C HQSC (bottom panel) of* ***bpy$_3$Ph*** *in CD_2Cl_2.*

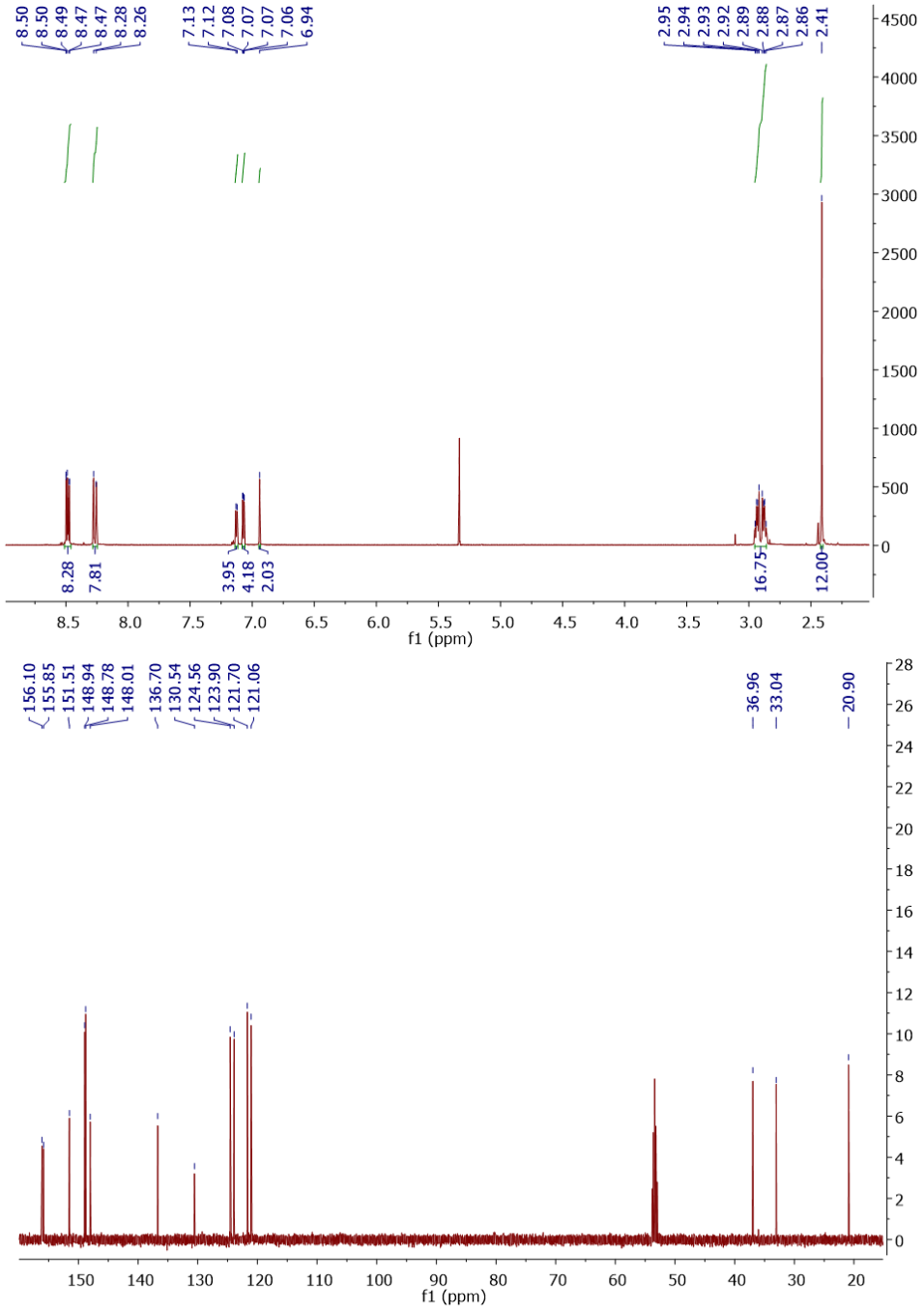

Figure 8.3. *^{1}H-NMR spectrum (top panel) and ^{13}C-NMR spectrum (bottom panel) of* ***bpy$_4$Ph*** *in CD_2Cl_2.*

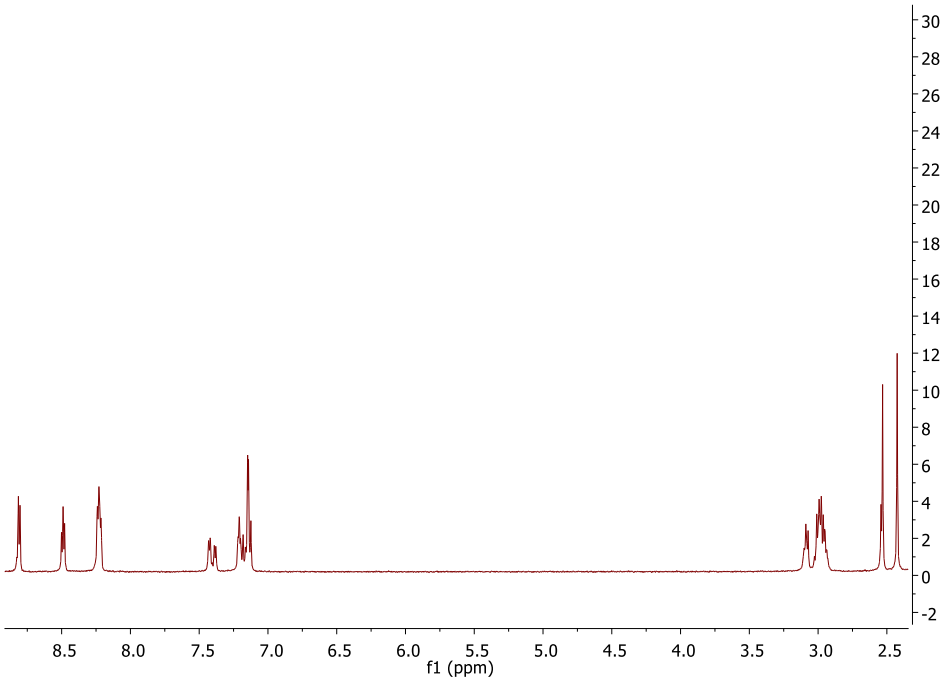

Figure 8.4. *^{1}H-NMR spectrum of* ***Re(bpy$_2$Ph)*** *in CD_3CN.*

References

1. K. Suzuki, A. Kobayashi, S. Kaneko, K. Takehira, T. Yoshihara, H. Ishida, Y. Shiina, S. Oishi and S. Tobita, *Phys. Chem. Chem. Phys.*, 2009, **11**, 9850-9860.
2. P. Ho, L.Q. Bao, R. Cheruku, J. H. Kim, *Electron. Mater. Lett.*, 2016, **12**, 638-644.
3. B. P. Sullivan, D. J. Salmon, T. J. Meyer, *Inorg. Chem.*, 1978, **17**(12), 3334-3341.
4. P. A. Anderson, G. B. Deacon, K. H. Haarmann, F. R. Keene, T. J. Meyer, D. A. Reitsma, B. W. Skelton, G. F. Strouse, N. C. Thomas, J. A. Treadway, A. H. White, *Inorg. Chem.*, 1995, **34**, 6145-6157.
5. K. S. Schanze, L. Y. C. Lee, C. Giannotti, D. G. Whitten, *J. Am. Chem. Soc.*, 1986, **108**, 2646-2655.

Acknowledgements

I thank the University of Messina and the Regione Sicilia for the PhD grant. The Ministero degli Affari Esteri e della Cooperazione Internazionale, Direzione Generale per la Promozione del Sistema Paese, is gratefully acknowledged for a Italy-Japan Collaborative Grant (Project title: "A supramolecular approach to artificial photosynthesis") given to my thesis supervisor, which supported my stage in Tokyo to perform photocatalysis experiments.